NTNU – Trondheim
Norwegian University of
Science and Technology

Grid Integration of the Wave Energy Converter Bolt2

Control of the Grid Side Converter with
Energy Storage

Johannes Christopher Ulvin

Problem Description

The goal of this thesis is to develop a model of a converter interfacing the DC-link with the grid side and to investigate the integration of an Energy Storage System (ESS) at the DC-link. The DC-link serves as the coupling point for several point absorbers that inject power onto the DC-link. Measurements from Fred Olsen's Wave Energy Converter (WEC) Bolt2 have been made available and are applied to the model. The tool for carrying out the work will be Matlab/Simulink. The main tasks to be accomplished can be divided in two parts:

- Develop and implement a model of the grid side converter and a functioning control system in order to enable stable operating conditions for the system.

- Explore the possibilities of integrating an Energy Storage System to mitigate power fluctuations and enable a more constant power supply.

Abstract

This thesis is written in cooperation with Fred Olsen's Wave Energy Project Bolt2 which is a Wave Energy Converter (WEC) recently deployed outside of Falmouth Bay in the UK. After the initial phases of testing, the device is to be grid connected to the local distribution network. The purpose of this thesis is to develop a model that can serve as a useful starting point for investigating grid connection issues for Wave Energy Converters or as a part of a complete wave-to-wire modelling of a WEC. The Bolt2 project will be used as a framework for the thesis. Measurements from the testing of Bolt2 have been provided and strengthen the project by applying real life conditions to the model.

The work emphasizes on the challenges of grid connecting wave energy devices as motivation for the work. As a first step, the design of the grid side converter and its control system is carried out with the main criterion being a constant DC-link voltage. In addition, the control circuit ensures no reactive power exchange at the converter output and that the currents are injected at the grid frequency. The control strategy applied is based on vector control due to its well documented performance in a variety of applications.

One of the main barriers for wave energy developers are the large power variations that are inherent to most WECs since the produced wave power goes through zero twice in each wave period. An effective way of reducing the power fluctuations is by disposing several point absorbers in an array configuration which is one of the advantages of Fred Olsen's Bolt2.

To further smooth out the power, an Energy Storage System (ESS) is considered. After a short discussion, the energy storage device was chosen to be a supercapacitor (SC) bank. Initially, the possibility to provide a constant power to the grid was investigated but was rejected as being unrealistic for a practical case. Instead, an alternative power management strategy of the ESS was developed. It was decided to chop off only the largest power peaks and to discharge whenever any amount of energy remained in the SCs for the storage system to be completely discharged and prepared for any incoming power peak. A bi-directional DC-DC converter was used to interface the SCs with the DC-link and the described power management strategy was realized through current control of the switching devices. Two similar but separate control schemes were necessary in order to perform both buck charging and boost discharging.

Finally, simulations of power data from a design sea state were performed in order to prove the validity of the developed model. The peak-to-average power ratio was demonstrated to be reduced with the integration of the energy storage system. However, the expenses of including a storage would have to be justified by reduced costs for the developer in order for the scenario to be economically viable.

Sammendrag

Denne oppgaven er skrevet i samarbeid med Fred Olsens bølgekraftprosjekt Bolt2. Bolt2 er en bølgekraftomformer som nylig er blitt utplassert utenfor Falmouth Bay i Storbritannia. Etter å ha gjennomgått den initielle testfasen, vil enheten bli tikoblet til det lokal distribusjonsnettet. Meningen med denne oppgaven er å utvikle en modell som kan bli brukt som et nyttig utgangspunkt for å undersøke nettilkoblingsproblemstillinger for bølgekraftomformere eller som en del av en fullstending "bølge-til-ledning"-modell. Bolt2-prosjektet vil bli brukt som rammeverk til oppgaven. Målinger fra testingen av Bolt2 har blitt gjort tilgjengelig og styrker prosjektet ved at virkelige forhold blir påtrykt modellen.

Arbeidet legger vekt på utfordringene ved nettilkobling av bølgekraftomformere som motivasjon for oppgaven. I et første steg blir kontrollsystemet til omformeren på nettsiden utviklet med en konstant DC-link spenning. Dessuten sikrer kontrollen at det ikke blir utvekslet noen reaktiv effekt ved tilkoblingspunktet og at strømmene blir injisert med nettfrekvensen. Kontrollstrategien som blir andvent er basert på vektorkontroll.

En av de største barrierene for bølgeenergiutviklere er de merkbare kraftvariasjonene som er iboende i de fleste bølgekraftomformere siden bølgekraften går innom null to ganger hver bølgeperiode. En effektiv måte å redusere kraftsvingningene er ved å plassere flere punktabsorbenter i en matriseformasjon. Dette er en av fordelene med Fred Olsens Bolt2. For å videre jevne ut kraften vil et energilager bli utforsket. Etter en kort diskusjon, ble energilageret valgt til å bestå av superkondensatorer. I utgangspunktet ble muligheten for å produsere konstant kraft til nettet undersøkt, men ble avvist for å være urealistisk i et praktisk tilfelle. Isteden ble en alternativ strategi utviklet. Det ble bestemt å kutte ut de største krafttoppene og hvis det fantes kraft i energilageret, skulle dette utlades umidelbart. En toveis DC-DC omformer ble benyttet til å koble til DC-linken og kontrollstrategien ble implementert via strømkontroll. To separate men liknende kontrollsystem var nødvendig for å både kunne utføre "buck"-lading og "boost"-utlading.

Til slutt ble simuleringer av kraft fra en design bølgetilstand utført for å bevise gyldigheten av modellen. Det ble vist at snittet mellom krafttoppene og gjenomsnittskraften kunne bli redusert ved integreringen av energilageret.

Preface

This thesis concludes my master's programme Energy and Environmental Engineering at the Norwegian University of Science and Technology. I would like to thank NTNU for offering a versatile study programme which has challenged me in a wide range of scientific fields, in addition to my specialization in Electric Power Engineering. I am also grateful for allowing me to go on exchange for one academic year at Nanyang Technological University in Singapore, and for providing the facilities during the work with my thesis.

My supervisor, professor Marta Molinas, deserves credit for giving me the opportunity to work in the complex and interesting field of wave energy, and I would especially like to express my gratitude for letting me attend and participate in relevant workshops and conferences.

A special thanks to my co-supervisor, Jonas Sjolte, for always taking the time to answer my questions and for sharing his views and insight.

Lastly, I would like to thank the co-students in my office space, Åshild Vatne, Christian Sandvik and Elisabeth Abildgaard for contributing to a healthy and good working environment.

Contents

List of Figures

List of Tables

Chapter 1

Introduction

1.1 Background

To this date, wave energy is a fairly unexploited resource with a high global potential which has recently been quantified above $2\ TWh$ [1]. Although the first patent was filed in 1799, wave energy is still an immature technology. However, the new millennium has been marked by raised oil prices and the threat of climate change. Thus, in the quest for renewable energy, an increasing number of interested parties are attracted by the high promise of wave energy characterized by its high energy density, predictability and the consistency of the waves. Especially the European countries bordering the Atlantic Ocean have initiated promising R&D projects to contribute to the EU's climate and energy target "20-20-20" [2]. It is worth mentioning MaRINET [3] in Ireland, Wavetrain 2 [4] in Portugal, Marina Platform [5], TROPOS [6] and the bimep [7] in Spain.

Previously, wave energy developers have been focusing on hydrodynamical aspects, mechanical optimization and survivability issues. In recent years, Wave Energy Converters are getting closer to the market and increased attention is being paid to the challenges of grid connecting wave energy devices [8] [9]. In that respect, it is vital to ensure stable operating conditions and conditioning of the power supplied to the grid to fulfil local grid requirements. Furthermore, wave energy is troubled by very high peak-to-average power ratios and has previously been studied by the author from a hydrodynamical aspect (paper attached in appendix F), and can be limited through control of the motor drive at the expense of the average power extraction [10] [11]. However, the variations still prevail when entering the electrical domain and further measures should be taken to ensure a more stable power supply. This is mainly due to two reasons, a high peak-to-average ratio represents high investment costs for the developer and may cause voltage and frequency instabilities in the grid network depending on the strength of the grid.

The purpose of this thesis is to design and implement a model of the grid side converter in Matlab/Simulink in order to supply wave power to the local grid. The control of the grid side converter is a vital task to ensure stable operating conditions. Further, the effect of introducing an energy storage system is investigated.

An initiative that will be paid special interest in this thesis is the Fred Olsen Wave Energy Project and their deployment of their recent prototype Bolt2 [12] at the Wave Hub [13] in the UK. The Wave Hub is a grid connected offshore facility for large scale testing of wave energy technologies. The project will serve as a framework for the thesis and measurements from testing of Bolt2 at the Wave Hub will be used as input to the developed model.

1.2   System Description

Fred Olsen has been involved in wave energy since 2000 and has focused on point absorbers to extract energy from the waves. They launched their first prototype Buldra in 2004, consisting of several point absorbers. After developing a number of prototypes, they decided to concentrate on a single point absorber concept, Bolt, which was deployed in the sea outside Risør in Norway in 2009 as a stand-alone system, and has been operated since then.

The Bolt system is depicted in figure 1.1 and will be consulted to explain the point absorber technology. The point absorber is semi-submerged and shaped as a cylinder. It is tightly moored to the sea bottom through a mooring rope which also serves as production rope. The rope is tied around a winch, which transforms the linear motion from the motion of the point absorber in the sea into a rotational motion. The angular velocity is increased through a gear system consisting of belts. The mechanical power is then turned into electrical power through an electrical machine.

The success and lessons learnt from Bolt laid the foundation for the next generation Bolt, the project Bolt2Wavehub. Bolt2 is shaped like a toroid, seen in figure 1.2, and is composed of 5 point absorbers coupled the DC-link. The advantage of the toroid shape is increased power production through the 5 point absorbers and also the ability to produce from pitch and roll motion as well as heave motion, which was the only production mode for Bolt. In addition, several point absorbers in an array configuration has a smoothing effect on power. The topology envisaged for grid connecting the device is shown in figure 1.3.
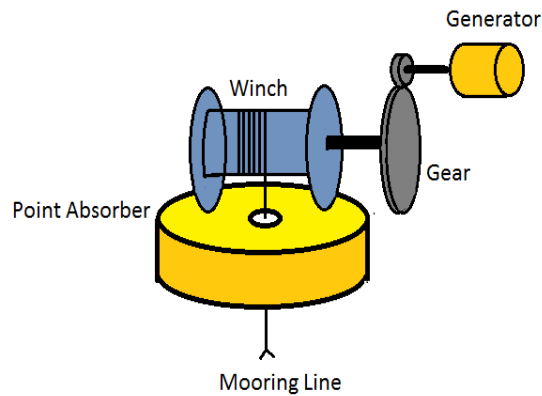
Figure 1.1: Sketch of Bolt
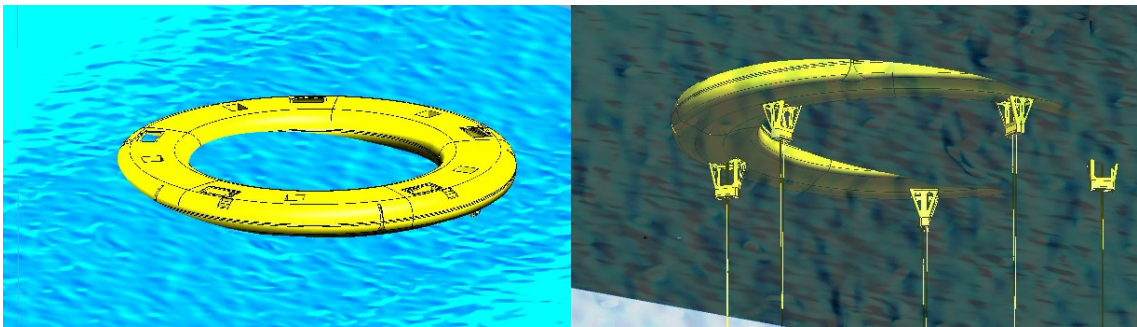
Figure 1.2: Artistic impression of Bolt2 [12]

The complete grid connected system is composed by:

- **Permanent Magnet Synchronous Machine (PMSM)**

- **AC-DC converter**

- **DC-link / DC-capacitor bank**

- **DC-AC converter**

- **Energy Storage System (ESS)**

- **Grid interfacing transformer**

  The scope of the thesis is restricted to the DC-link, its interfacing to the grid side and the energy storage system.

3
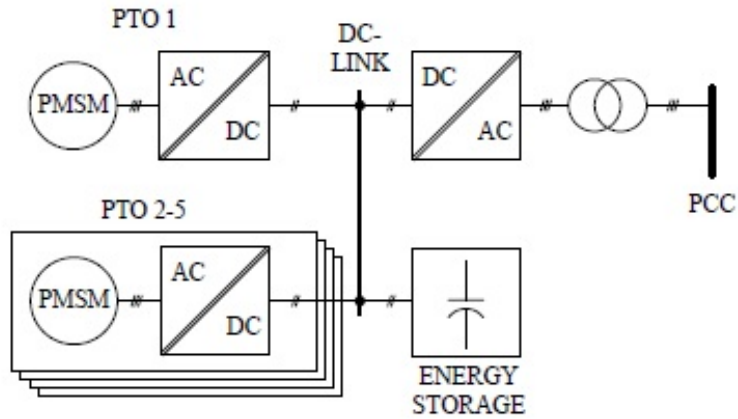
Figure 1.3: Grid connected system [12]

1.3   Structure of the Thesis

The thesis is divided into 7 chapters. **Chapter 2** provides a description of the Wave Hub together with grid connection specifications, which are used to outline the motivating factors for the thesis. In **chapter 3**, a control strategy for the grid side converter is derived and a tuning of the controllers is performed. A general discussion of the energy storage system is initiated in **chapter 4**. The energy requirements of the WEC serve as basis for a power management strategy for the storage system. **Chapter 5** documents the controllers' performance and includes the simulation results for power series from a design wave state. A discussion of the simulation results is provided in **chapter 6**. Finally, the conclusion rounds off the thesis in **chapter 7** with suggestions of further work. To avoid disturbing the composition of the thesis, some general theory is provided in the appendix together with supplementary simulation results and conference proceedings.

Chapter 2

Grid Connection at the Wave Hub

2.1 Grid Connection Requirements

The development of the electrical infrastructure of the Wave Hub has been undertaken by the South West of England Regional Development Agency (SWRDA) and the generated electricity is exported to the local grid via the Western Power Distribution (WPD) substation at Hayle on the north coast of Cornwall, UK.

Several requirements are imposed on electricity producers to be able to connect to the grid, and this is also the case for wave energy producers. The document that states the electrical connection parameters for the connection of wave energy converter devices to the Wave Hub project is the WEC connection specifications available at the Wave Hub website [14]. The power quality at the offshore connection point should be of a quality that would be acceptable for direct connection to WPD's local distribution system. The most relevant requirements for the power quality and a description of those are cited below:

- **Harmonic distortion:** Harmonics are highly unwanted, SWRDA has set limits for the maximum harmonic current from a producer at each frequency up to the 50th harmonic and are given in appendix C of [14]. Harmonics are sinusoidal disturbances whose frequency is a multiple of the grid frequency (the fundamental). These disturbances are superimposed to voltage and/or current, provoking a deviation from ideal sinusoidal conditions. Converters are highly non-linear devices and can produce a high amount of harmonic currents depending on the topology. Grid side filters are often included to reduce the amount of harmonic currents injected into the grid.

- **Voltage levels:** The array must be able to handle voltage changes of $\pm 10\%$ of the $11kV$ voltage as measured at the Offshore Connection Point. An increase of

5

voltage is referred to as a voltage swell and can be caused by an abrupt reduction in load. A reduction of voltage, a voltage dip, is inversely often caused by an abrupt increase in load due to short circuits and faults.

- **Frequency:** The WEC developer must ensure that its array supplies its registered capacity within the range of $\pm 1\%$ of $50Hz$. In addition it is stated that the developer shall use its best endeavours to stay connected to the distribution system until the frequency drops to $47Hz$ at which disconnection occurs. A deviation from the system frequency can arise when the demand and generation differ. In those cases, the electrical machines will either increase or decrease their speed which directly affects the frequency of the generated power.

- **Power factor:** The export power factor should be unity at the low voltage side of the Offshore Connection Point transformer, unless otherwise instructed. However, on request by SWRDA, the WEC should also be able to provide a power factor at any set point between 0.97 leading (inductive) and 0.97 lagging (capacitive). In general, reactive power is unwanted since this causes circulation of non-useful currents. However, some ability to produce or consume reactive power can be appropriate to mitigate voltage swells or dips in the system.

- **Flicker:** Although flicker is not mentioned in [14], it is a typical problem at the point of common coupling for wave farms. If there is no power smoothing, the power delivered from a point absorber varies with a frequency twice the wave frequency and can cause voltage instabilities at the point of connection with the grid. These voltage instabilities are denoted flicker and can be disturbing for other costumers connected to the coupling point. The magnitude of the variations depend on the strength of the grid.

2.2 Modelling of the Grid Connection

2.2.1 Converter

The converter is a Voltage Source Converter (VSC) and its operation is described in appendix C.1. The VSC is a self-commutated converter and requires semiconductors which can be turned on and off in response to a gating signal. The switching device chosen is the Insulated Gate Bipolar Transistor (IGBT) mainly due to its ability to sustain a very high switching frequency. The IGBTs are connected in anti-parallel with diodes in order to allow a bi-directional power flow. The IGBTs are connected in a full bridge topology which requires six sets of IGBTs/Diodes. The switching pattern is determined through Sinusoidal Pulse Width Modulation (SPWM). The technique is explained in detail in appendix C.1.3.

2.2.2 DC-Link and DC-Capacitor

The DC-link is the connection between the machine side converter and the grid side converter, where the DC-capacitor is the connecting element. A constant DC voltage indicates the balancing of active power between the two sides. Therefore, by controlling the voltage on the DC-link, the amount of power transferred to the grid can be controlled. A design criterion for the grid side converter will therefore be to maintain a stable DC-link voltage.

The DC-capacitor should be chosen according to two criteria: minimizing both the voltage ripple and the converter response time. The switching of the converter creates current harmonics which again results in a voltage ripple at the DC-side. The voltage ripple can be reduced by increasing the capacitor size. However, a large capacitor increases the converter response time. In addition, an over-sized capacitor is not a cost effective solution. An estimation of the required size of the DC-capacitor is given in [15]:

$$C_{dc} = \frac{2\tau_{dc}S_n}{V_{dc,n}^2} \tag{2.1}$$

Where $V_{dc,n}$ is the nominal DC voltage and S_n denotes the nominal apparent converter power. τ_{dc} is the time constant equal to the time needed to fully charge the capacitor at rated conditions. In [15] a τ_{dc} of $5ms$ is selected to satisfy small ripple and small transient over-voltage. Reactive or resistive effects due to the DC-cables are neglected in this thesis.

2.2.3 Filter

In order to reduce the harmonics created by the PWM-switching, a filter is required. The grid filter is assumed to be a single inductive filter (L-filter), L_f with an internal resistance, R_f. An estimation of a reasonable inductance filter size is proposed in [16]:

$$L_f = \frac{V_{dc}}{8I_{rp,max}f_s} \tag{2.2}$$

Where $I_{rp,max}$ is the maximum tolerated ripple current, f_s is the switching frequency of the converter and V_{dc} is the DC-link voltage.

For better filtering performance, more complex filters like LC-filters or LCL-filters can be considered but will not be discussed in this thesis.

2.3 Power Transfer to the Grid

Both reactive and active power fluctuations affect the grid. The impact of the power flow on the voltage in a transmission line is described by the equations below, where the change in voltage magnitude is $\triangle E$, and the change in the voltage angle is δE:

$$\triangle E = \frac{RP + XQ}{E} \tag{2.3}$$

$$\delta E = \frac{XP - RQ}{E} \tag{2.4}$$

Generally, for transmission lines, we have $R << X$, and hence $\triangle E \propto Q$ while $\delta E \propto P$ and more specifically, we get:

$$\triangle E = \frac{XQ}{E} \tag{2.5}$$

$$\delta E = \frac{XP}{E} \tag{2.6}$$

From equation (2.5), it can be seen that the voltage drop in the transmission line is directly proportional to the reactive power produced/consumed by the grid side converter. Hence, it is desirable to operate with a reactive power production equal to zero. However in section 2.1, the producers are required to be able to operate with a reactive power production of ± 0.97 pu. This is because it could contribute to recover stable operating conditions for voltage swells or dips at the point of common coupling. For instance, injecting reactive power can be a remedy for a low voltage ride through.

Similarly, by inspecting equation (2.6), the change in voltage angle is directly proportional to the active power injected into the transmission line. Thus, fluctuating active power results in a fluctuating voltage angle. For the case of a weak grid with fluctuating power contributors, the superposition of fluctuating voltage angle contributions ultimately results in frequency instabilities at the point of common coupling. Therefore, it is desirable that power producers operate with a constant power production so that the resulting voltage angle at the point of common coupling remains stable which results in a stable system frequency.

To summarize, it can be stated that active power control contributes to frequency control whereas reactive power control contributes to voltage control.

Chapter 3

Control of the Grid Side Converter

3.1   Introduction

The control of the grid side converter is developed in this chapter. Voltage oriented vector control is applied which enables independent control of both active and reactive power. The control technique is useful for several applications and widely available in literature [17][18][19]. The method requires a transformation from the normal *abc*-frame to the *dq*-frame through Clark and Park transformations. The transformation turns sinusoidal signals into constant signals so that PI-controllers can be used. From [20] it is known that for PI-controllers to eliminate the error signal, the input must be constant. The transformations are developed in appendix D. Balanced three phase conditions are assumed together with a lossless converter.
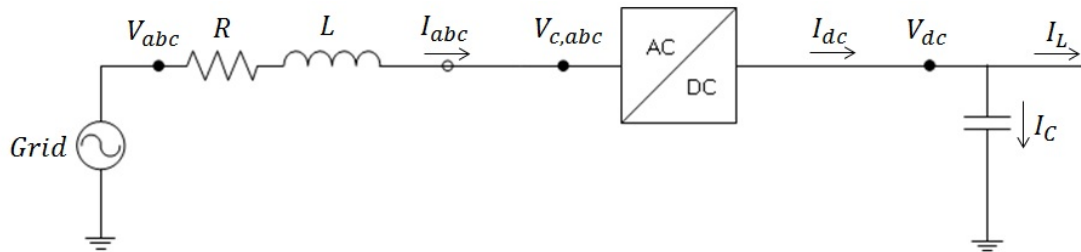
Figure 3.1: Grid side model

3.2   System Equations

The equations describing the system makes the basis of the control structure in order to determine the closed loop transfer functions of the system and to determine the tuning of the controllers. Firstly, the dynamics of the grid side will be considered and the power balance between the DC and the AC side is examined. Finally, the DC-link will be

analysed. The system equations will be developed on the basis of figure 3.1. The AC side of figure 3.1 shows only the per phase equivalent of the grid side, but consists of three phases.

3.2.1 Grid Side Equations

The voltage change between the stiff voltage, V_{abc} and the converter output, $V_{c,abc}$, is given as:

$$V_{abc} - V_{c,abc} = RI_{abc} + L\frac{dI_{abc}}{dt} \tag{3.1}$$

As previously discussed, reference values in the dq-frame are needed as input to the control system to be able to use PI-controllers. Hence, equation (3.1) is transformed to the dq-frame according to the voltage invariant dq-transform described in appendix D:

$$V_d - V_{c,d} = L\frac{dI_d}{dt} + RI_d - \omega LI_q \tag{3.2}$$

$$V_q - V_{c,q} = L\frac{dI_q}{dt} + RI_q + \omega LI_d \tag{3.3}$$

Equations (3.2) and (3.3) are dependent on both the d-axis and q-axis currents. In order to decouple the two axes, a fictive voltage is defined:

$$V_d' = V_{c,d} + V_{ff,d} = V_{c,d} - \omega LI_q - V_{g,d} \tag{3.4}$$

and:

$$V_q' = V_{c,q} + V_{ff,q} = V_{c,q} + \omega LI_d + V_{g,q} \tag{3.5}$$

Where $V_{ff,d}$ and $V_{ff,q}$ are the feed forward terms. Since this is a voltage invariant transformation, $V_q = 0$. By rearranging (3.4) and inserting into (3.2) and similarly with (3.5) and (3.3), we get:

$$V_d' = L\frac{dI_d}{dt} + RI_d \tag{3.6}$$

and

$$V_q' = L\frac{dI_q}{dt} + RI_q \tag{3.7}$$

Hence, due to the feed forward terms, the control system experiences the direct and quadrature axes as decoupled and independent.

3.2.2 Power Balance

In the dq-frame, the three phase apparent power at the AC-side can be expressed as [19]:

$$S = \frac{3}{2}V_{dq}I_{dq}^*$$

(3.8)

$$S = \frac{3}{2}(V_d + jV_q)(I_d - jI_q)$$

(3.9)

$$S = \frac{3}{2}\{(V_dI_d + V_qI_q) + j(-V_dI_q + V_qI_d)\}$$

(3.10)

Since we assume no losses in the conversion, we can write:

$$P_{AC} = \text{Re}\,(S) = \frac{3}{2}(V_dI_d + V_qI_q) = P_{dc} = V_{dc}I_{dc}$$

(3.11)

And as we apply voltage invariant transformation ($V_q = 0$), we get:

$$\frac{3}{2}V_dI_d = V_{dc}I_{dc}$$

(3.12)

$$I_{dc} = \frac{3}{2}\frac{V_d}{V_{dc}}I_d$$

(3.13)

Further, the reactive power produced by the converter can be written as:

$$Q = \text{Im}\,(S) = \frac{3}{2}(-V_dI_q + V_qI_d)$$

(3.14)

Again, we can simplify:

$$Q = \frac{3}{2}(-V_dI_q)$$

(3.15)

From this, it can be concluded that the active and reactive power produced by the converter can be controlled independently when considering the equations in the dq-frame. The active power output is determined by V_d and I_d while the reactive power output is controlled by V_d and I_q. Since V_d is assumed stiff, it suffices to control the direct and quadrature axes currents. The specifications in chapter 2 [14] insists that for normal operating conditions there should be no reactive power transfer at the point of common coupling. By inspecting (3.15) we see that this is achieved by setting $I_q = 0$.

3.2.3 DC-Link Equations

The current balance of the DC-link can be expressed:

$$C\frac{dV_{dc}}{dt} = I_c = I_{dc} - I_L$$

(3.16)

By inserting equation (3.13) for I_{dc}:

$$C\frac{dV_{dc}}{dt} = \frac{3}{2}\frac{V_d}{V_{dc}}I_d - I_L \tag{3.17}$$

3.3   Voltage Oriented Vector Control

The control strategy is a cascaded control structure with an inner current controller and an outer voltage controller. The idea is to use the relation between the DC voltage and the d-axis current to control the DC-link voltage, and the relation between the reactive power and the q-axis current to control the reactive power. Hence, the output signal from the outer voltage controller serves as the reference input for the d-axis of the inner current controller. Similarly, the output signal from the reference value for the q-axis current controls the amount of reactive power in the system.

An overview of the proposed control system is shown in figure 3.2.
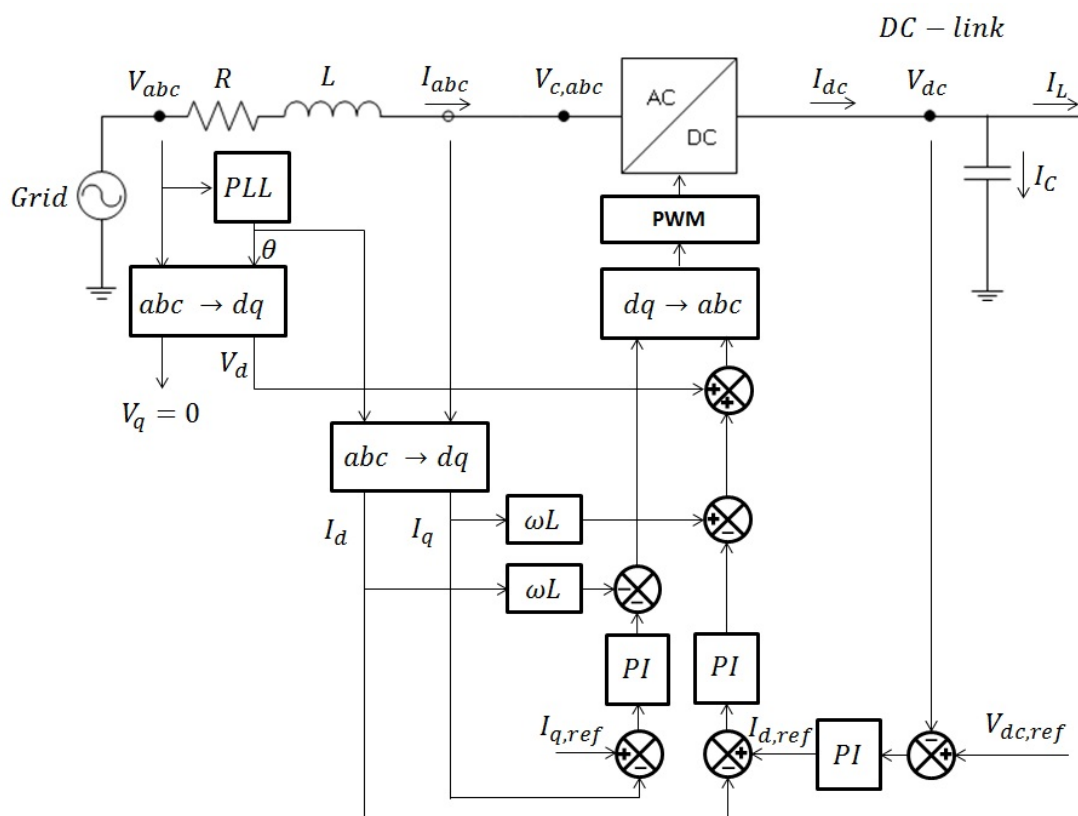
Figure 3.2: Detailed control system

3.3.1 Phase Lock Loop

The Phase Lock Loop is denoted PLL in figure 3.2. It is a control system that senses the phase of the input signal. Information about the phase angle is necessary to perform the dq-transformations.

3.3.2 Inner Current Controller

Grid Side Equations

As explained in the previous chapter, the decoupling of the current axes enables the control to see an RL circuit. Equations (3.6) and (3.7) are on the same form. Therefore, a general system transfer function will be derived for both axes. By taking the Laplace transform we get:

$$V'(s) = LI(s)s + RI(s) = I(s)(Ls + R) \tag{3.18}$$

This gives:

$$\frac{I(s)}{V'(s)} = \frac{1}{Ls + R} \tag{3.19}$$

The system transfer function is defined as:

$$\frac{I(s)}{V'(s)} = \frac{1}{R}\frac{1}{1 + \tau s} \tag{3.20}$$

Where $\tau = \frac{L}{R}$ and is the time constant of the system.

Time Delay

The converter is essentially a voltage transformer, where the voltage follows the desired reference. This is achieved through the sinusoidal pulse width modulator which controls the switching which in return creates a time delay. In the Laplace-domain, a time delay is described as $e^{-T_s s}$, where T_s represents the switching time delay in seconds [20]. The term $e^{-T_s s}$ is not a rational function and makes it impossible to determine an algebraic solution for the control parameters. The function needs to be approximated to a rational expression:

$$e^{-T_s s} = \frac{e^{\frac{-T_s}{2}s}}{e^{\frac{+T_s}{2}s}} \approx \frac{1 - \frac{T_s}{2}s}{1 + \frac{T_s}{2}s} \tag{3.21}$$

To obtain this expression both the numerator and the denominator have been expand by their first order component of their Taylor series, which is called a first order Pade-approximation. However, to eliminate numerator dynamics, an even simpler approximation can be derived by taking the expansion of the numerator to be of order 0.

Hence, we get:

$$e^{-T_s s} \approx \frac{1}{1 + \frac{T_s}{2} s} \qquad (3.22)$$

We define $T = \frac{T_s}{2}$ and the transfer function of the time delay as:

$$J(s) = \frac{1}{1 + Ts} \qquad (3.23)$$

PI-Controller

PI-controllers are applied as regulating device to follow the desired reference. A PI-controller is composed by to terms: the proportional gain and the integral term connected in parallel. The proportional gain amplifies the input error signal by a factor Kp. The proportional gain is a regulator by itself called the P-controller, however it has the disadvantage that it is unable to eliminate the stationary error signal. This can be solved by including an integral term, $\frac{K_i}{s}$, at the expense of a reduced stability margin [20]. The regulator is described by the following transfer function:

$$PI = K_p + \frac{K_i}{s} = \frac{K_p s + K_i}{s} = K_p(\frac{1 + \frac{K_p}{K_i}}{\frac{K_p}{K_i} s}) = K_p(\frac{1 + T_i s}{T_i s}) \qquad (3.24)$$

Where T_i is defined as $\frac{K_p}{K_i}$.

Transfer Functions

The complete control system for the current controller is described by the three blocks mentioned and the block diagram for both d and q axes is given in figure 3.3.
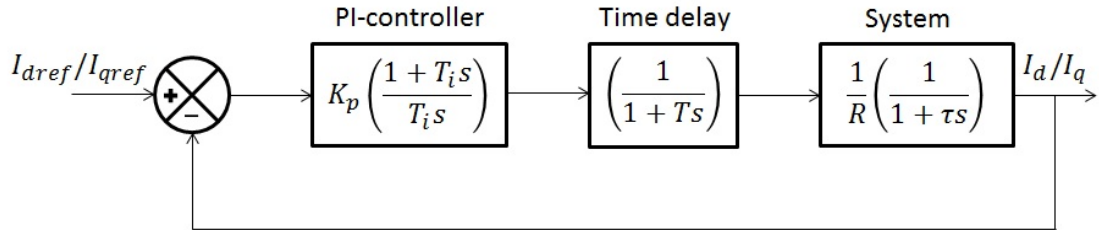
Figure 3.3: Block diagram of the current controller

Hence, the open loop transfer function is given as:

$$h_{0,cc}(s) = K_p \frac{1 + T_i s}{T_i s} \frac{1}{1 + Ts} \frac{1}{R} \frac{1}{1 + \tau s} \qquad (3.25)$$

14

After simplification, the closed loop transfer function can be expressed:

$$M_{0,cc}(s) = \frac{h_{0,cc}(s)}{h_{0,cc}(s) + 1} = \frac{K_p}{T\tau R s^2 + \tau R s + K_p} \tag{3.26}$$

When including the feed forward terms cancelling out the cross-couplings, the complete block diagram with both axes is given in figure 3.4
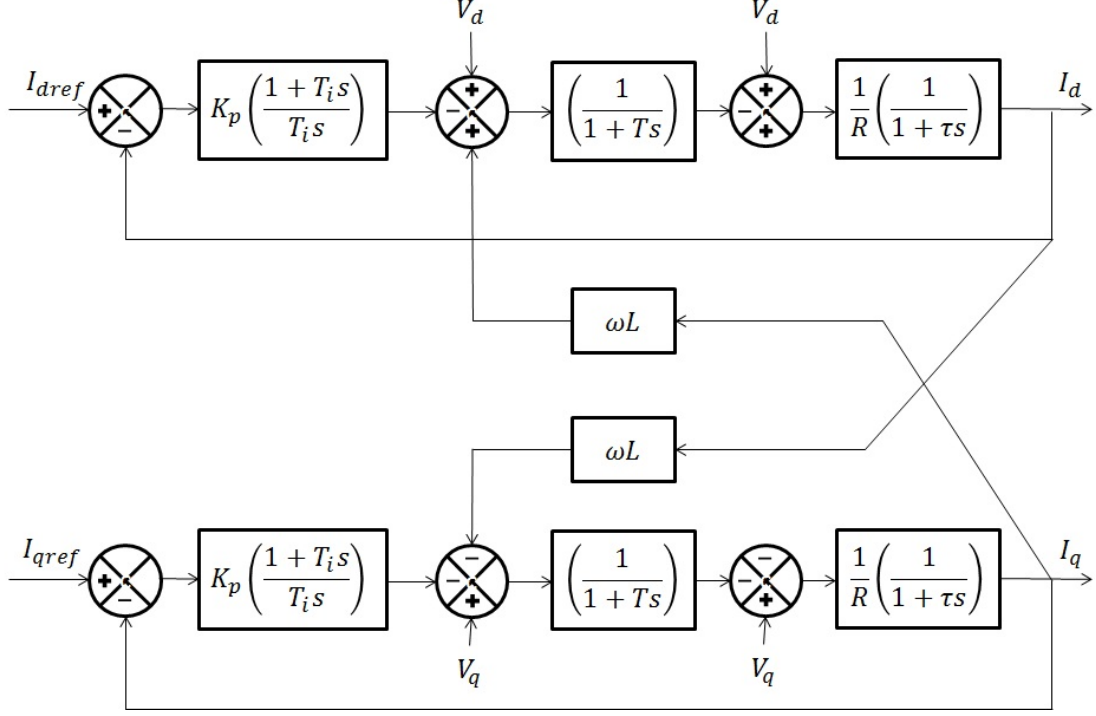
Figure 3.4: Complete block diagram of the current controller for both the d and q axes

3.3.3 Outer Voltage Controller

The aim of the outer voltage controller is to regulate the DC-link voltage to the desired value by creating the reference value for the direct-axis current. The current balance of the DC-link is given by equation (3.17). This equation is non-linear and has to be linearised in order to investigate the stability conditions of the DC-link. However, the steady state conditions of the DC-link imply a nearly constant DC-voltage. Hence, we can linearise the equation near the operation point of the reference voltage, $V_{dc,ref}$. After performing a Taylor series expansion [18]:

$$C\frac{dV_{dc}(s)}{dt} = \frac{3}{2}\frac{V_{d,o}}{V_{dc,ref}}I_d(s) \tag{3.27}$$

By Laplace transforming:

$$V_{dc}(s) = \frac{3}{2}\frac{V_{d,o}}{V_{dc,ref}}\frac{1}{sC}I_d(s) \tag{3.28}$$

15

Where $\frac{V_{d,o}}{V_{dc,ref}}$ is a constant and gives a linear relation between I_d and V_{dc}. Thus, by controlling I_d, the DC-link voltage can be controlled. The outer voltage controller will therefore compute the reference value for I_d, which serves as input for the current controller. Since this is a cascaded control system, it is vital that the inner control system, i.e. the current controller, operates faster than the outer control system, i.e. the voltage controller. The transfer function of the inner current controller is of second order. Therefore, in order to analyse the operation of the voltage controller, the transfer function of the second controller should be simplified to a first order transfer function to facilitate the analysis.

Approximation of the Inner Current Controller to a 1st Order Function

A method to determine a simplified 1st order model of the current controller's closed loop transfer function can be found in the literature [17]. The idea is that the time integral of the controller's error signal should be equal for both the actual model and the 1st order model.

For a unit step input, $\frac{1}{s}$, the integral of the error signal for the current controller is given as:

$$\int_0^\infty (i_{ref}(t) - i(t))\,\mathrm{d}x = \lim_{s\to\infty} s\frac{1}{s}\{\frac{1}{s} - \frac{1}{1 + \frac{\tau R}{K_p}s + \frac{\tau RT}{K_p}s^2}\frac{1}{s}\} = \frac{\tau R}{K_p} = 2T \qquad (3.29)$$

Similarly, for the first order approximated model of the current controller:

$$\int_0^\infty (i_{ref}(t) - i(t))\,\mathrm{d}x = \lim_{s\to\infty} s\frac{1}{s}\{\frac{1}{s} - \frac{1}{1 + T_{eq}}\frac{1}{s}\} = T_{eq} \qquad (3.30)$$

Hence, we get:

$$T_{eq} = 2T \qquad (3.31)$$

Feed Forward Term

A cascaded control system has the disadvantage of a slow response to disturbances. From a control point of view, the disturbance to the system is represented by the current coming onto the DC-link, I_L. In order to reduce the disturbing effect on the system, a feed forward term can be included. Ideally, the feed forward term should compensate so that the overall disturbance sensed by the control system is zero. Under stable conditions, the DC-voltage is constant and the capacitor current I_c equal to 0. Thus by rearranging

3.17, the feed forward term can be determined:

$$I_d = \frac{2}{3}\frac{V_{dc}}{V_d}I_L \qquad (3.32)$$

Transfer Functions

When including a PI-controller, the open loop transfer function of the outer voltage controller becomes:

$$h_{0,vc} = K_{pv}(\frac{1+T_{iv}s}{T_{iv}s})(\frac{1}{1+T_{eq}s})\frac{3V_d}{2V_{dc}}\frac{1}{Cs} \qquad (3.33)$$

The subsequent block diagram is depicted in figure 3.5.
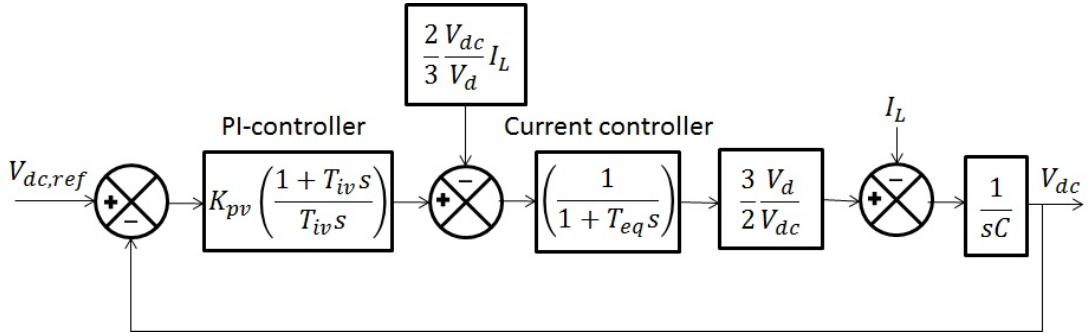
Figure 3.5: Block diagram for the voltage controller

3.4 Tuning of the Controllers

The objective of controllers, is that the output should exactly follow the reference input. Therefore the performance of a controller can be evaluated by the following criteria[21]:

- A zero steady state error signal

- Fast transient response

- Small overshoot, or small oscillations

In order to achieve this, an effective tuning of the controller parameters, the gain and the integral time constant, is necessary. Two different tuning techniques will be applied to the control loops, depending on their transfer function characteristics.

3.4.1 Tuning of the Current Controller: Modulus Optimum

Modulus optimum is used for low order transfer functions (< 3) and makes the crossover frequency as high as possible. By inspecting equation (3.25), it can be deduced that

$\tau >> T$ for realistic values. When there is a dominant in the transfer function, the integral time constant of the PI controller is selected to cancel out the dominant pole. Thus, by setting $T_i = \tau$ equation (3.25) can be simplified:

$$h_{0,cc}(s) = \frac{K_{pi}}{\tau R} \frac{1}{s(1+Ts)} \tag{3.34}$$

The closed loop transfer function is given as [20]:

$$M_{cc}(s) = \frac{h_{0,cc}(s)}{h_{0,cc}(s)+1} = \frac{n_{0,cc}}{n_{0,cc}+d_{0,cc}} \tag{3.35}$$

Where $n_{0,cc}$ and $d_{0,cc}$ respectively are the open loop transfer function's nominator and denominator.

$$M_{cc}(s) = \frac{1}{1 + \frac{\tau R}{K_{pi}}s + \frac{\tau RT}{K_{pi}}s^2} \tag{3.36}$$

A standard 2. order system can be written as [20]:

$$h(s) = \frac{\frac{1}{k}}{1 + 2\zeta\frac{s}{\omega_0} + (\frac{s}{\omega_0})^2} \tag{3.37}$$

Where ω_0 is the undamped resonance frequency, and ζ is the relative damping coefficient. By equating (3.36) and (3.37):

$$\omega_0 = \sqrt{\frac{K_{pi}}{\tau RT}} \tag{3.38}$$

and

$$\zeta = \frac{1}{2}\sqrt{\frac{\tau R}{K_{pi}T}} \tag{3.39}$$

The modulus optimum criterion ensures that the closed loop transfer function is equal to 1 high up in the frequency spectrum. If $M_{cc}(s) \approx 1$, the output follows the reference signal and is the desired operation of the controller circuit. Thus:

$$|M_{cc}(s)| = 1 \tag{3.40}$$

We get:

$$\frac{1}{(K_{pi} - T\tau R\omega^2)^2 + (\tau R\omega)^2} = 1 \tag{3.41}$$

By rearranging:

$$K_{pi} = \frac{\tau R(T\omega^2 + 1)}{2T} \tag{3.42}$$

For $\omega << \frac{1}{\sqrt{T}}$:

18

$$K_{pi} = \frac{\tau R}{2T} \tag{3.43}$$

Hence, we get:

$$\zeta = \frac{1}{\sqrt{2}} \approx 0.7 \tag{3.44}$$

$$\omega_0 = \frac{1}{\sqrt{2}T} \tag{3.45}$$

Thus, the tuning of the current PI-controllers is given as:

$$K_{pi} = \frac{\tau R}{2T} \tag{3.46}$$

$$T_i = \tau \tag{3.47}$$

3.4.2 Tuning of the Voltage Controller: Symmetrical Optimum

Since the DC-voltage control loop has two poles at the origin, pole cancellation is not possible and modulus optimum cannot be applied. Therefore, an alternative method is used: Symmetrical Optimum. The method has the benefit that it maximizes the phase margin, and the system can therefore tolerate more delays which is an important feature in the cascaded control system.

The phase margin of equation (3.33) can be derived:

$$\langle h_{0,vc}(j\omega) = \arctan\left(T_{iv}\omega\right) - 90° - \arctan\left(T_{eq}\omega\right) - 90° = \Psi_m - 180° \tag{3.48}$$

Where Ψ_m is the phase margin. According to the Nyquist-criterion for an open loop transfer function without poles in the right half plane, the following conditions apply for a system to be stable:

$$\langle h_{0,vc}(j\omega_c) > -180° \tag{3.49}$$

$$|h_{0,vc}(j\omega_{180})| < 1 = 0[dB] \tag{3.50}$$

Hence, the phase margin expresses the additional negative phase tolerated by the system before it becomes unstable when $|h_{0,vc}(j\omega)| = 1 = 0[dB]$, i.e. at the crossover frequency, ω_c. It is generally accepted that for a satisfactory dynamic response, the phase margin should be greater than 45°. [20][21]

Further, the phase margin is maximized:

$$\frac{d\Psi_m}{d\omega_c} = \frac{T_{iv}}{1 + (T_{iv}\omega_c)^2} - \frac{T_{eq}}{1 + (T_{eq}\omega_c)^2} = 0 \tag{3.51}$$

Solving for ω_c:

$$\omega_c = \frac{1}{\sqrt{T_{iv}T_{eq}}} \tag{3.52}$$

Thus, the phase margin becomes:

$$\Psi_m = \arctan{(T_{iv}\frac{1}{\sqrt{T_{iv}T_{eq}}})} - \arctan{(T_{eq}\frac{1}{\sqrt{T_{iv}T_{eq}}})} \tag{3.53}$$

$$\Psi_m = \arctan{(\sqrt{\frac{T_{iv}}{T_{eq}}})} - \arctan{(\sqrt{\frac{T_{eq}}{T_{iv}}})} \tag{3.54}$$

We define:

$$\theta = \arctan{(\sqrt{\frac{T_{iv}}{T_{eq}}})} \tag{3.55}$$

Then:

$$\arctan{(\sqrt{\frac{T_{eq}}{T_{iv}}})} = 90° - \theta \tag{3.56}$$

By inserting into (3.54):

$$\Psi_m = \theta - (90° - \theta) = 2\theta - 90° \tag{3.57}$$

$$sin(\Psi_m) = sin(2\theta - 90°) = -\cos(2\theta) \tag{3.58}$$

From (3.55) and (3.58):

$$\sqrt{\frac{T_{iv}}{T_{eq}}} = \tan(\theta) = \sqrt{\frac{1 - \cos(2\theta)}{1 + cos(2\theta)}} = \sqrt{\frac{1 + \sin(\Psi_m)}{1 - sin(\Psi_m)}} \tag{3.59}$$

Finally, the integral time constant can be expressed:

$$T_{iv} = T_{eq}\frac{1 + \sin(\Psi_m)}{1 - sin(\Psi_m)} = a^2 T_{eq} \tag{3.60}$$

Where a is a constant number, defined by a given phase margin.

At the stability margin:

$$\Psi m = 0° \longrightarrow a = 1 \tag{3.61}$$

Hence, $a \geqq 1$ for a stable system. However, it is desirable with a greater stability margin. From the earlier criteria:

$$\Psi m > 45° \longrightarrow a \gtrsim 2.41 \tag{3.62}$$

As mentioned, at the crossover frequency, $|h_{0,vc}(j\omega_c)| = 1$. By evaluating, we get:

$$|h_{0,vc}(j\omega_c)| = \frac{3K_{pv}V_d}{2V_{dc}} \frac{|1 + T_{iv}\omega_c j|}{|T_{iv}\omega_c j - T_{iv}T_{eq}\omega_c^2|}|\frac{1}{j\omega_c C}| = 1 \tag{3.63}$$

$$|h_{0,vc}(j\omega_c)| = \frac{3K_{pv}V_d}{2V_{dc}C} \frac{\sqrt{1^2 + (T_{iv}\omega_c)^2}}{\sqrt{(T_{iv}\omega_c)^2 + (-T_{iv}T_{eq}\omega_c^2)^2}} \frac{1}{\omega_c C} = 1 \tag{3.64}$$

$$(\frac{3K_{pv}V_d}{2V_{dc}\omega_c C})^2 = \frac{(T_{iv}\omega_c)^2 + (-T_{iv}T_{eq}\omega_c^2)^2}{(1^2 + (T_{iv}\omega_c)^2)} \tag{3.65}$$

Inserting for ω_c:

$$(\frac{3K_{pv}V_d}{2V_{dc}\omega_c C})^2 = \frac{\frac{T_{iv}}{T_{eq}} + 1}{1 + \frac{T_{iv}}{T_{eq}}} = 1 \tag{3.66}$$

We get:

$$K_{pv} = \frac{2V_{dc}}{3V_d}\omega_c C = \frac{2V_{dc}}{3V_d}\frac{1}{\sqrt{T_{iv}T_{eq}}}C \tag{3.67}$$

21

Chapter 4

Energy Storage System

4.1 Introduction

The power produced from a wave energy converter is intermittent and variable. Hence, large variations in the output power on the generator side are a common problem. Of course, ideally electricity producers should deliver constant power to the grid. There are several reasons for this. Firstly, from a producer's perspective, a high peak power compared to the average power, would give a poor utilization of the installed conversion and transmission capacity. As an example, for the power fluctuations generated by Bolt2, the ratings of the installed capacity would have to be 20 times higher than the average exported power [22]. Secondly, with the increasing contribution of distributed generation, the grid is more likely to be disturbed and might lead to an unstable frequency and voltage variations. Although there are no restrictions on the active power production for grid connection at the Wave Hub [14], a large scale integration of wave energy or other renewable based resources to the grid would require smoothing of the power output for a minimum disturbance of the grid.

4.1.1 Array Configuration

An effective way of reducing the peak-to-average power ratio is by relying on several WECs in an array configuration. By distributing the point absorbers along the incoming wave direction, the wave hits the point absorbers at different times and by adding the powers together, a mitigating effect is obtained. When deciding the disposition of the point absorbers in the array, the point absorbers should not disturb the energy capture of the nearby point absorbers: the shadowing effect should be minimized. With these and other considerations taken into account, the resulting proposed configuration for Fred Olsen's array of Bolt2 WECs is given in figure 4.1(a). Figure 4.1(b) shows the decrease in peak-to-average power ratio when increasing the number of point absorbers in the array.
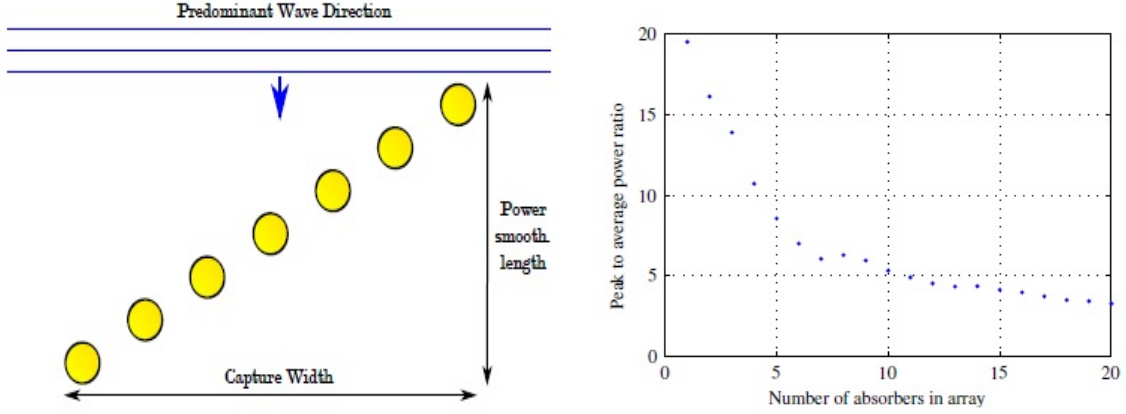
(a) Peak-to-average ratio as a function of number of point absorbers

(b) Proposed array configuration for Bolt2

Figure 4.1: Array considerations [22] (a),(b)

4.1.2 Energy Storage System (ESS)

To further improve the power quality, the integration of an energy storage system (ESS) is considered. Ideally, the ESS should supply or absorb active power according to the power difference between the generated power from the array, P_{prod} and the desired output power supplied to the grid, P_{grid}. The sizing of the energy requirements of the ESS will be the difference between the maximum and the minimum value of the time integral of the difference between the produced power and the desired output power [23]. We can write:

$$P_{sc}(t) = P_{prod}(t) - P_{grid}(t) \qquad (4.1)$$

$$E_{ESS}(t) - E_{ESS}(t=0) = \int_0^t P_{sc}(t) \qquad (4.2)$$

In order to gain a control of the desired power dispatch from the energy storage system, $P_{sc}(t)$, the energy storage must be interfaced to the DC-link through a DC-DC converter. Since the energy storage should both be in charging and discharging mode, bi-directional DC-DC converters have to be applied and the energy storage is placed on the low voltage side of the converter.

4.2 Energy Storage Devices

The performance of energy storage devices are usually measured by two main criteria, their energy density and their power density and can be placed in the Ragone chart as shown in figure 4.2. Conventional capacitors excel in power density whereas batteries and fuel cells perform well in terms of energy density. Nevertheless, for many applications, wave energy included, a considerable amount of energy is required in addition to a high

power density to mitigate short term power fluctuations. Hence, the research direction for energy storage devices tends towards the right top corner of the Ragone chart. As seen from figure 4.2, the supercapacitors bridge the gap between conventional capacitors and batteries and will therefore be considered as the storage device in this thesis. Supercapacitors have already been investigated for similar applications [24]. Other storage devices that show promise for renewable energy applications are flywheels and SMES (Superconducting Magnetic Energy Storage) [25].
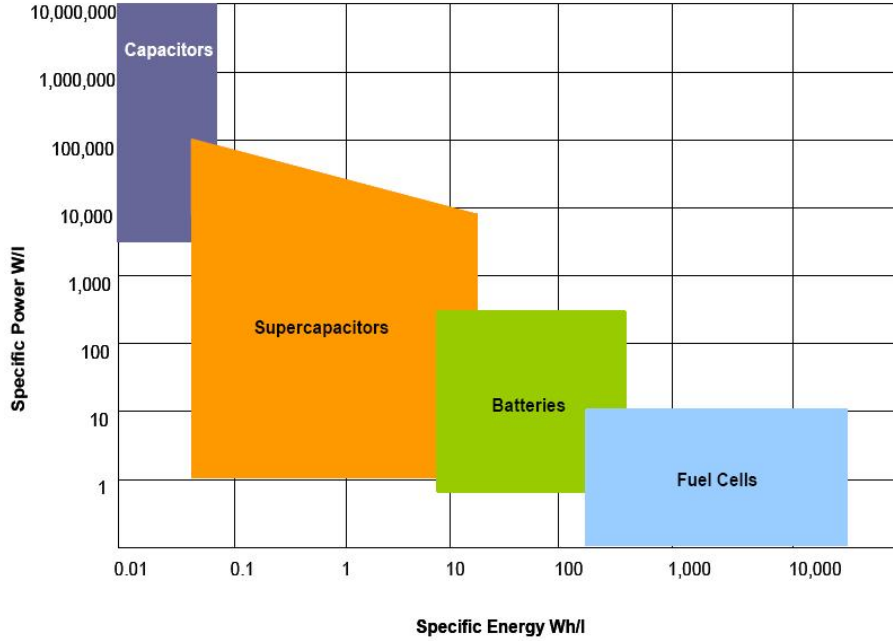
Figure 4.2: Simplified Ragone chart [26]

Supercapacitors

Supercapacitors, also known as ultracapacitors or electrochemical double layer capacitors (EDLC), disposes of high surface area nano-structured electrodes immersed in electrolyte. When a voltage is applied to the electrodes, dissolved ions in the electrolyte are attracted to the electrode surface by an equal opposite charge in the electrode. These two parallel regions of charge forms the origin for the term "double layer".

They can be analysed in the same way as regular capacitors. Hence:

$$C \propto \frac{A}{d} \tag{4.3}$$

and

$$E = \frac{1}{2}CV^2 \tag{4.4}$$

From the two above equations and since supercapacitors disposes of a high surface

24

double layer of charge, they have a much higher energy density compared to conventional capacitors. Another advantage is that the storage process does not require any chemical or structural changes to the materials. Therefore, the device can withstand a lot more charging-discharging cycles than batteries (10^6 cycles compared to 10^3 for batteries) [27]. In addition, nano-structured carbon materials are relatively cheap and have well-developed fabrication techniques so that a wide range of capacitances can be achieved [27]. Supercapacitor cells are delivered with low voltages and serial connections are needed to obtain high voltage levels

An important feature of the operation of supercapacitors is their charge/discharge curve which describes the voltage potential of an energy storage device with respect to time when charging and discharging. As opposed to batteries, which dispose of a nearly flat charge/discharge curve, the supercapacitor potential increases during charging and decreases during discharging since the current outputted by a capacitor is given by:

$$I = C\frac{dV}{dt} \tag{4.5}$$

4.3 Power Management of the ESS

The design wave to be analysed in the thesis has been provided by Fred Olsen. The power time series are recorded data for the wave power coming into the DC-link from an array of 7 point absorbers and is given in figure 4.3. Hence, the power series have already been smoothed due to the coincidence factor described in the introduction of this chapter. Since the deployment of Bolt2 is still at a testing phase, the power series are normalized to the average output power in order to avoid giving any indications of Bolt2's power output.

4.3.1 Constant Grid Power

As discussed in section 4.1.2, the power rating and the energy rating of the supercapacitor bank can be determined from the power profile in figure 4.3. If the WEC is to supply constant power to the grid, the power rating of the energy storage system is found as the difference between the peak wave power and the mean power, which will be the highest power demand the storage system would have to provide during the time series. Secondly, to consider the energy requirements, the power demand of the supercapacitor bank, $P_{sc}(t)$, would have to be integrated. The resulting plot is shown in figure 4.4.

By examining the energy profile expected of the energy storage system in figure 4.4, it can be deducted that the voltage profile of the supercapacitor would experience a similar
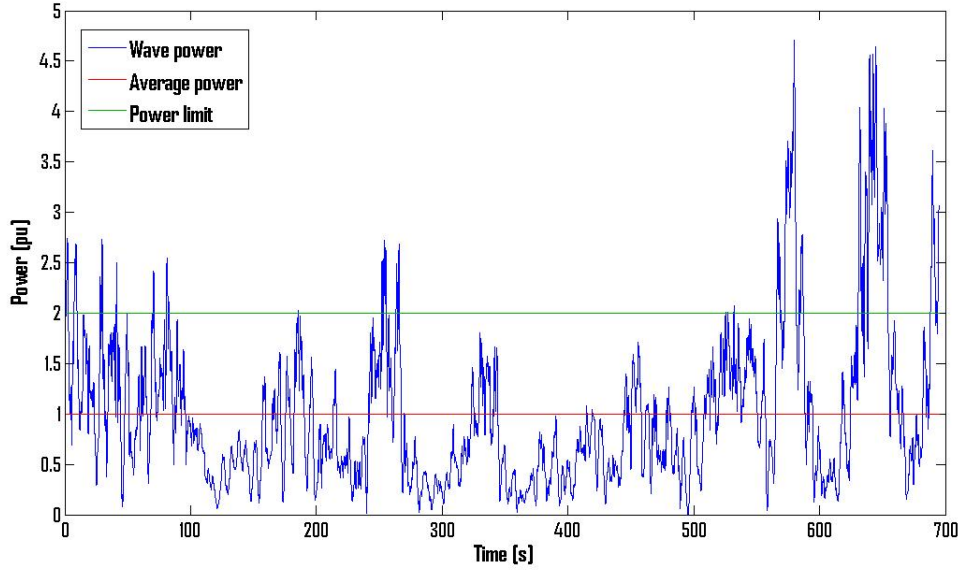
Figure 4.3: Incoming wave power
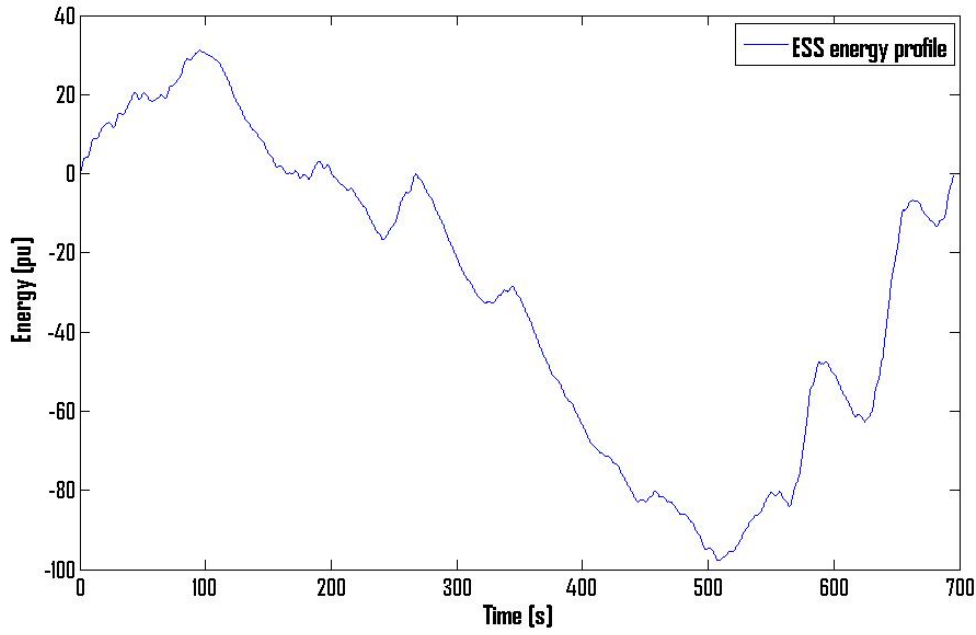
Figure 4.4: Integral of supercapacitor power profile $P_{sc}(t)$

profile. This is because the energy in a supercapacitor is proportional to the square of the voltage. The rated energy capacity of the energy storage device would be:

$$E_{sc,rat} = \Delta E_{max} = E_{sc,max} - E_{sc,min} = 31.2pu - (-97.7)pu = 128.9pu \qquad (4.6)$$

For an operating voltage of the supercapacitor between $V_{sc,max}$ and $V_{sc,min}$, the required capacitance would be:

26

$$C_{sc} = \frac{2E_{sc,rat}}{V_{sc,max}^2 - V_{sc,min}^2} \tag{4.7}$$

Further, the energy profile is negative for a large part of the simulation. This means a negative supercapacitor voltage and is not possible. Therefore, the supercapacitor must have an initial voltage so that it never reaches its lower operation voltage limit, or in other words when the supercapacitor is discharged. Hence, the initial voltage of the supercapacitor should be:

$$V_{sc,init} = \sqrt{\frac{2E_{sc,min}}{C_{sc}} + V_{sc,min}^2} \tag{4.8}$$

Several remarks need to be made about this case. Firstly, the capacitance value can become unreasonably large for low voltage levels for a practical case since the power variations are significant. Although feasible; it is only a matter of the number of series and parallel connections, supercapacitors are expensive components and the expenses of including an energy storage system have to be compensated by the savings from a smoother power output. Further, the supercapacitor is set so that it never becomes fully charged or discharged since the incoming wave power is known. In the real sea, this is not the case and a more complex approach would have to be developed for the power management of the energy storage system.

4.3.2 Peak-to-Average Ratio $= 2$

If the idea of a constant power output to the grid has to be abandoned, the next step would be to investigate the possibility to smooth out the highest power peaks. Hence, the following supercapacitor power management rule could be outlined:

Firstly, an acceptable peak-to-average ratio would have to be determined with a maximum power limit set accordingly, P_{set}. For all incoming power values above this limit, the supercapacitors should store the power difference:

$$P_{sc}(t) = P_{prod}(t) - P_{set} \tag{4.9}$$

A possible criterion for the discharge mode could be as follows. As soon as P_{prod} drops below P_{set}, the energy storage should discharge by keeping $P_{grid} = P_{set}$ as for the charging mode until the energy storage is fully discharged. In this way, the supercapacitor will experience a relatively quick discharge time before reaching the lower discharge limit ready to use its full charging capability for the next high incoming peak power.

To summarize, the energy storage charges for high sporadic power peaks and discharges

as long as there is energy available in the storage system. A measure of the energy content in a supercapacitor is the voltage and it will dictate the state of charge of the storage device. Hence, the power management of the ESS is summarized in table 4.1. The same strategy is also found in the literature [28].

Table 4.1: Proposed ESS power management strategy

Power criterion	Voltage criterion	Current reference	ESS Operation
$P_{prod} > P_{set}$	-	$\frac{P_{prod}-P_{set}}{V_{sc}}$	Charging Mode
$P_{prod} < P_{set}$	$V_{sc} > V_{sc,min}$	$-(\frac{P_{prod}-P_{set}}{V_{sc}})$	Discharging Mode
$P_{prod} < P_{set}$	$V_{sc} = V_{sc,min}$	0	Redundant ESS

To size the supercapacitor for this strategy, the power peaks higher than the set point value, P_{set}, are integrated to determine their energy content. Thus, for a peak-to-average ratio $k = 2$, the energy profile in figure 4.5 can be obtained.
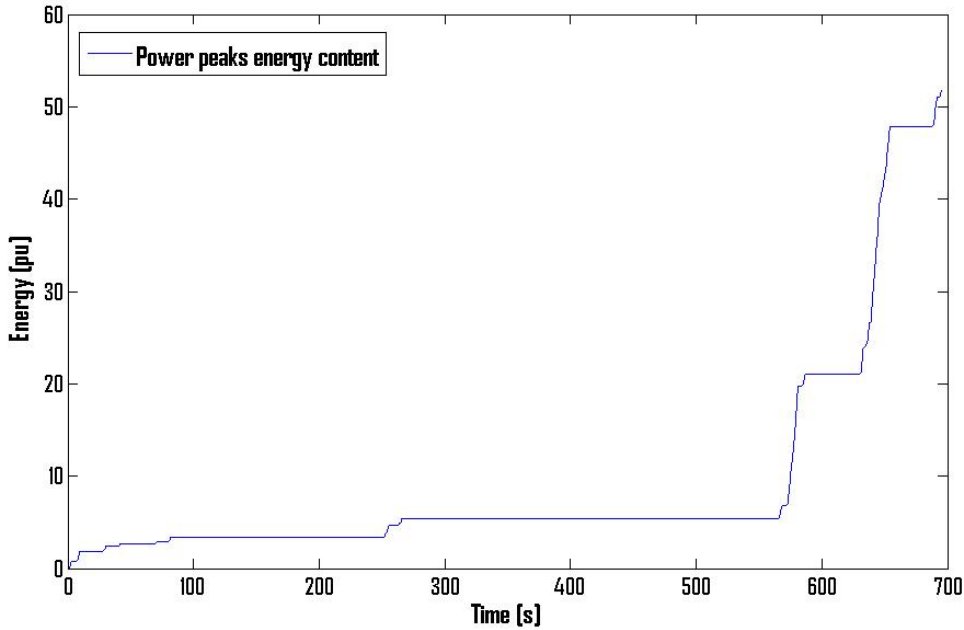
Figure 4.5: Integral of the power peaks larger than P_{set}

By inspecting figure 4.5, it can be observed that for $k = 2$ the energy storage is redundant for a large part of the simulation time. However, towards the end of the simulation, two very large power peaks occur. Since they occur with quite a significant time difference, it can be assumed that the supercapacitors be able to discharge before the largest power peak arrives after around $630s$. Hence, the energy increase during the

28

highest power peak, ΔE_{max} will be used for sizing the supercapacitor for this sea state. Thus, we get:

$$\Delta E_{max} = E_{655s} - E_{630s} = 47,9pu - 21pu = 26,9pu \qquad (4.10)$$

By comparing ΔE_{max} for $k = 1$ and $k = 2$ the maximum energy rating is reduced from $129pu$ to $26,9pu$. Since the capacitances are proportional to the energy rating, we get:

$$\frac{C_{sc,k=1}}{C_{sc,k=2}} = \frac{\Delta E_{max,k=1}}{\Delta E_{max,k=2}} = \frac{128,9}{26,9} = 4,8 \qquad (4.11)$$

Thus, by doubling the accepted peak-to-average ratio, the required supercapacitor size is reduced by a factor of $4,8$.

4.4 Bi-Directional DC-DC converter

A DC-DC converter is required to control the power dispatch from the energy storage device. Since the converter must be able to conduct the current in both directions, bidirectional power switches are needed. IGBTs can be used as power switches and should be connected in anti-parallel with a diode. Both the classic buck and boost converter circuits can be made bidirectional by replacing the switch and the diode by power switch and diode configuration. The bi-directional DC-DC converter is depicted in figure 4.6. It can be analysed in two modes defined by the polarity of the inductor current: charging or discharging. A satisfying value for the inductance in the DC-DC converter can be calculated as [16]

$$L_{sc} = \frac{V_{sc}}{8\Delta I_{sc}f_{dc}} \qquad (4.12)$$

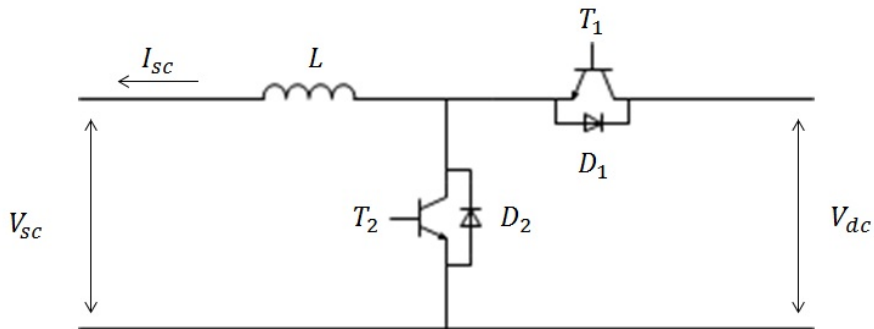Where f_{dc} is the switching frequency of the DC-DC converter.

Figure 4.6: Circuit diagram of the bi-directional DC-DC converter

Boost Discharging Mode

In the boost discharging mode the DC-DC converter should operate as a conventional boost converter. Hence, T_1 should be turned off and the classic boost converter circuit is obtained.

Buck Charging Mode

Inversely, when operating in buck charging mode T_2 should be turned off and the conventional buck converter circuit is obtained.

An introduction to the buck and boost converter can be found in appendix C.2.

4.4.1 Control of the DC-DC Converter

The control scheme of the bidirectional DC-DC converter is based on inductor current control and is found in literature [15] [29] [30]. The converter is assumed lossless. Thus, the reference current the supercapacitor should provide is defined as in table 4.1, depending on the mode of operation.

The voltage across the inductive element of the converter is given as:

$$V_L = L\frac{dI_{sc}}{dt} \tag{4.13}$$

By transforming into the Laplace-domain, the system transfer function can be obtained:

$$\frac{V_L(s)}{I_{sc}(s)} = \frac{1}{Ls} \tag{4.14}$$

In order to control the switching of the DC-DC converter to follow the reference value, $I_{sc,ref}$, PI-controllers will be used:

$$V_L(s) = (I_{sc,ref}(s) - I_{sc}(s))(K_{psc}\frac{1 + T_{isc}s}{T_{isc}s}) \tag{4.15}$$

Hence, the block diagram of the closed control loop of the DC-DC current controller is depicted in figure 4.7.

The open loop transfer function is:

$$h_{0,sc}(s) = \frac{K_{psc}(1 + T_{isc}s)}{T_{isc}Ls^2} \tag{4.16}$$

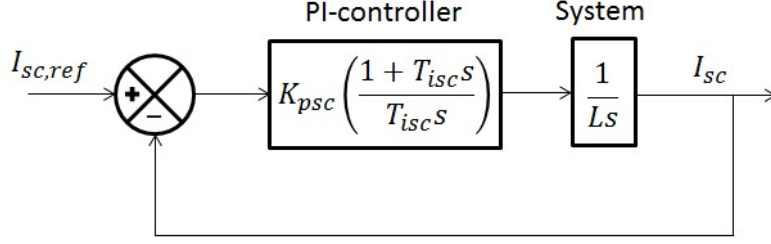The closed loop transfer function can be derived:

Figure 4.7: Block diagram of the ESS current control

$$M_{sc}(s) = \frac{I_{sc,ref}(s)}{I_{sc}(s)} = \frac{h_{0,sc}(s)}{1 + h_{0,sc}(s)} = \frac{K_{psc}(1 + T_{isc}s)}{T_{isc}Ls^2 + K_{psc}(1 + T_{isc}s)} \tag{4.17}$$

To ensure better control dynamics, a filter with time constant τ_{sc} is applied to the current reference. The closed loop transfer function becomes:

$$M_{sc}(s) = \frac{I_{sc,ref}(s)}{I_{sc}(s)} = \frac{1}{1 + \tau_{sc}s} \frac{1 + T_{isc}s}{1 + T_{isc}s + \frac{T_{isc}}{K_{psc}}Ls^2} \tag{4.18}$$

Similarly to the approach in chapter 4, the transfer function can be simplified by setting $\tau_{sc} = T_{isc}$. Thus, we get:

$$M_{sc}(s) = \frac{I_{sc,ref}(s)}{I_{sc}(s)} = \frac{1}{1 + T_{isc}s + \frac{T_{isc}}{K_{psc}}Ls^2} \tag{4.19}$$

It can be observed that equation (4.19) is at the same form as the standardized 2. order system in equation (3.37). Hence:

$$T_{isc} = \frac{2\zeta}{\omega_0} \tag{4.20}$$

$$K_{psc} = 2\zeta L\omega_0 \tag{4.21}$$

In [29], the damping ζ is proposed to be equal to 0.707 as in chapter 4. The system bandwidth is also limited to 10% of the control frequency, f_{dc}:

$$\omega_0 \leq \frac{2\pi f}{10} \tag{4.22}$$

The gating signals to the IGBTs are created through the PWM-technique. The duty cycle must be calculated and compared to a sawtooth carrier wave of amplitude 1 and switching frequency f_{dc}.

31

4.4.2 Buck Mode

The estimation of V_L is obtained through the current control. In addition the voltage across the inductor can also be written as:

$$V_L = D_{buck} V_{dc} - V_{sc} \tag{4.23}$$

From this the control law for the switching can be obtained:

$$D_{buck} = \frac{V_L + V_{sc}}{V_{dc}} \tag{4.24}$$

The signal is then compared to the sawtooth signal to generate the switching pulses for the switching device T_1 while T_2 is off during the entire buck mode operation. The resulting control block diagram is depicted in figure 4.8.
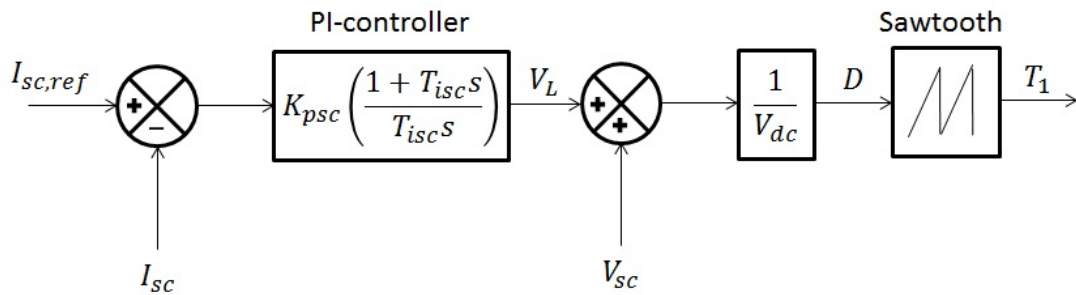
Figure 4.8: Block diagram of the DC-DC control in buck mode

4.4.3 Boost Mode

The estimation of V_L is obtained as for the buck mode. However, the control law has changed since:

$$D_{boost} = 1 - \frac{V_{sc} + V_L}{V_{dc}} \tag{4.25}$$

Thus, the gating signal for T_2 can be obtained, while T_1 is maintained off during the entire boosting mode. The control block diagram for the boost mode is shown in figure 4.9:

Figure 4.9: Block diagram of the DC-DC control in boost mode

Chapter 5

Simulations

5.1 Model Description

The validity and performance of the model will be evaluated through simulations implemented in Matlab/Simulink and follows the theory presented in chapter 3 and 4. The overall 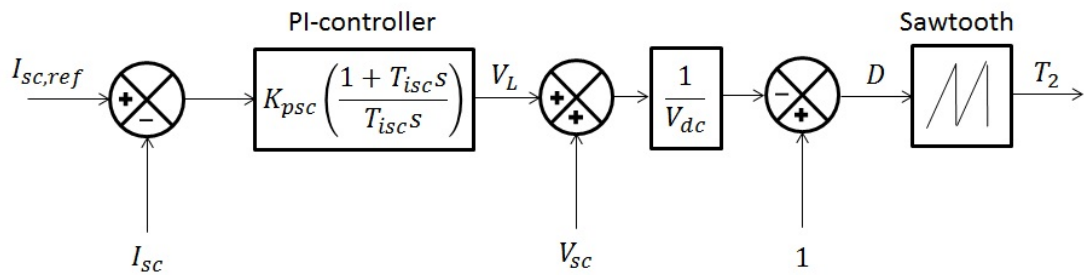simulink model window is depicted in figure 5.1. While the electrical entities are obtained from the Simulink library extension SimPowerSystems, the control subsystems defining the DC-link control and the DC-DC control are given in appendix A.1 and A.2.

Inputs to the DC-link control system are the DC-link voltage reference and the reactive power reference and can be found in the DC-link control subsystem in appendix A.2. Further, The incoming wave power disturbing the DC-link is provided as power time series by Fred Olsen. Hence, the incoming DC-current from the machine side converter is denoted in the model as:

$$I_g(t) = \frac{wavepower(t)}{V_{dc}(t)} \tag{5.1}$$

The supercapacitor power reference is calculated from equation (4.1):

$$P_{sc,ref}(t) = wavepower(t) - waveaverage(t) \tag{5.2}$$

Thus, the reference current the supercapacitor should provide is determined:

$$I_{sc,ref}(t) = \frac{P_{sc,ref}(t)}{V_{sc}(t)} \tag{5.3}$$

However, when accepted peak-to-average ratio k is set larger than 1, the current reference will have to be discontinuous and should be 0 when the ESS is redundant according to table 4.1. In order to manipulate the current reference, a switching scheme is employed. If the control system senses that the supercapacitor minimum operating voltage
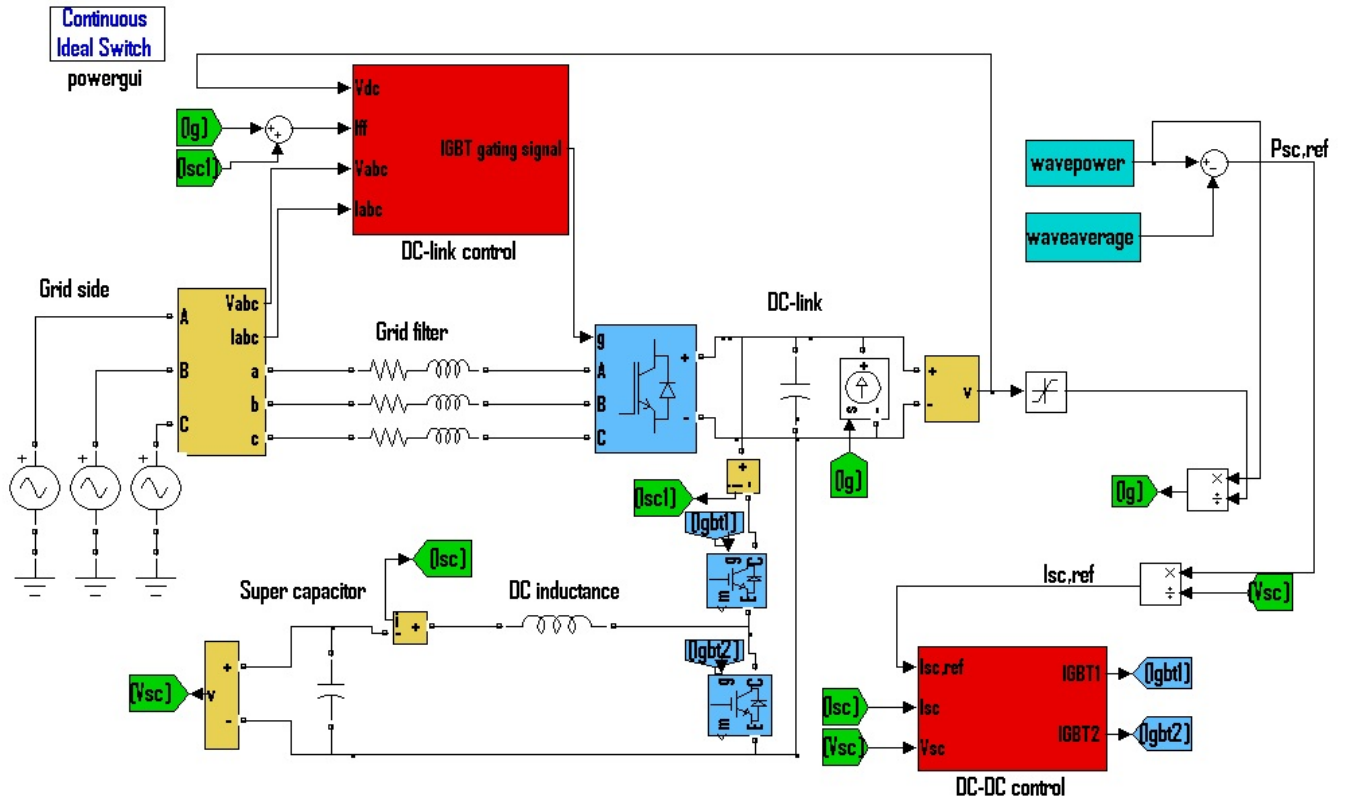
Figure 5.1: Overall simulink model of the system

has been attained, the current should switch from following the reference from equation (5.3) and go to 0. To prevent the supercapacitor from start charging in this mode, a minimal voltage decrease is ensured since the DC-DC converter is unable to provide a constant zero current, due to current ripple. The DC-DC control system is attached in appendix A.1. for further interest.

The system parameters are specified in table 5.1. The parameters are normalized to the per unit system as defined in appendix E, with the base quantities being the peak phase value of the stiff AC voltage, and the average power of the power series. It is important to point out that the results in this chapter will be presented with currents defined in opposite direction of chapter 3 in order to display positive values for power.

5.2 Controller Performance

In order to evaluate the performance of the controllers the bode plots of the open loop transfer functions are presented in this section. In addition, the transient time responses of the system are documented when exciting the system at start-up.

Table 5.1: System parameters

Description	Parameter	Value	Unit
Average power	P_{avg}	1	pu
Peak power	P_{pk}	4.7	pu
DC-link voltage	V_{dc}	1.5	pu
Rated frequency	f	50	Hz
VSC switching frequency	fs	2000	Hz
Stiff AC voltage	V_{abc}	1	pu
DC-capacitor	C_{dc}	13.4%	pu
AC filter resistance	R_f	0.42%	pu
AC filter inductance	L_f	8.4%	pu
DC-DC inductance	L_{sc}	1.85%	pu
Supercapacitor	C_{sc}	0.0021%	pu
DC-DC converter switching frequency	f_{dc}	10000	Hz

5.2.1 Inner Current Controller

The inner current controller was tuned according to modulus optimum. We get:

$$h_{0,cc}(s) = \frac{1}{2T} \frac{1}{s(1 + Ts)} \tag{5.4}$$

$$T = \frac{1}{2 \cdot fs} = \frac{1}{2 \cdot 2000 Hz} = 2.5 \cdot 10^{-4} s \tag{5.5}$$

$$h_{0,cc}(s) = \frac{2000}{s + 2.5 \cdot 10^{-4} s^2} \tag{5.6}$$

The bode plot of the open loop transfer function can be obtained from Matlab and is shown in figure 5.2.

From 5.2, the phase margin is given as 65.5° and the gain margin is given as infinite. The gain margin is infinite because the phase $h_{0,cc}(j\omega)$ never reaches $-180°$ irrespective of ω. Thus, the inner current controller system could be qualified as robust and the tuning of the inner current controller could be deemed successful.

The error signals of the d-axis current and the q-axis current are shown in figure 5.3 and figure 5.4 to demonstrate the performance of the current controllers at start-up. The error signals are shown since the current reference for the d-axis may be variable. From figure 5.3 it can be seen that d-axis current error signal has a significant overshoot and a small negative oscillation before eliminating the error at around 0.06s. For the error signal of the q-axis current in figure 5.4, the overshoot is smaller than for the d-axis.
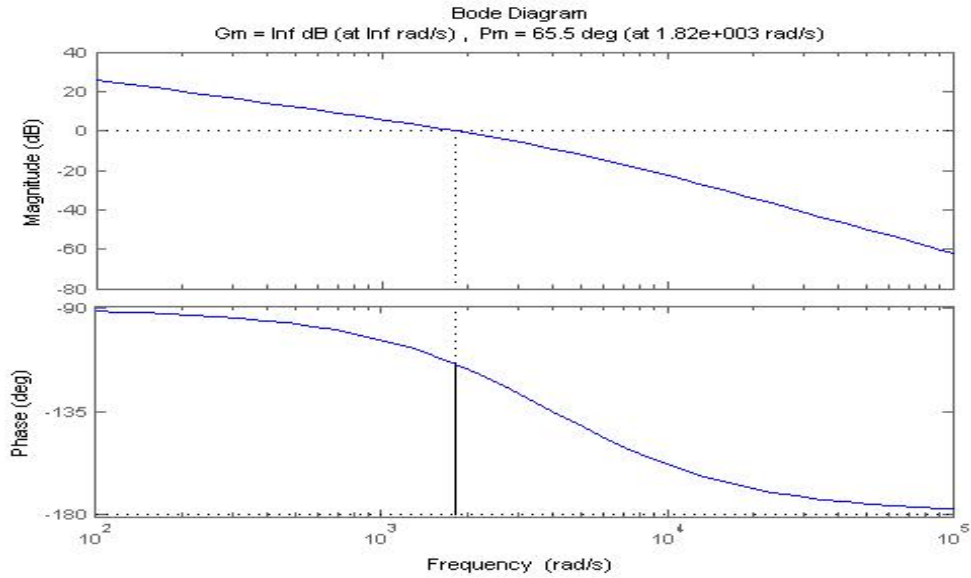
Figure 5.2: Bode plot of the open loop transfer function of the inner current controller

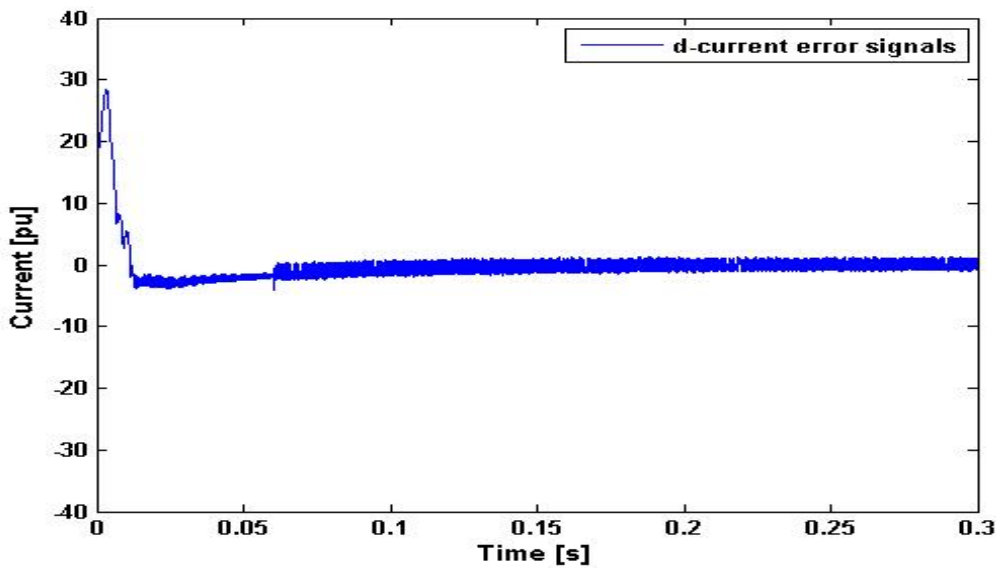Otherwise, the profile is quite similar and also stabilizes at around $0.06s$.

Figure 5.3: Error signal of the direct current axis at simulation start-up

5.2.2 Outer Voltage Controller

As argued in section 3.3.2, the phase margin of the outer voltage controller can be defined by a constant value a. For a robust control system it is desirable with a phase margin
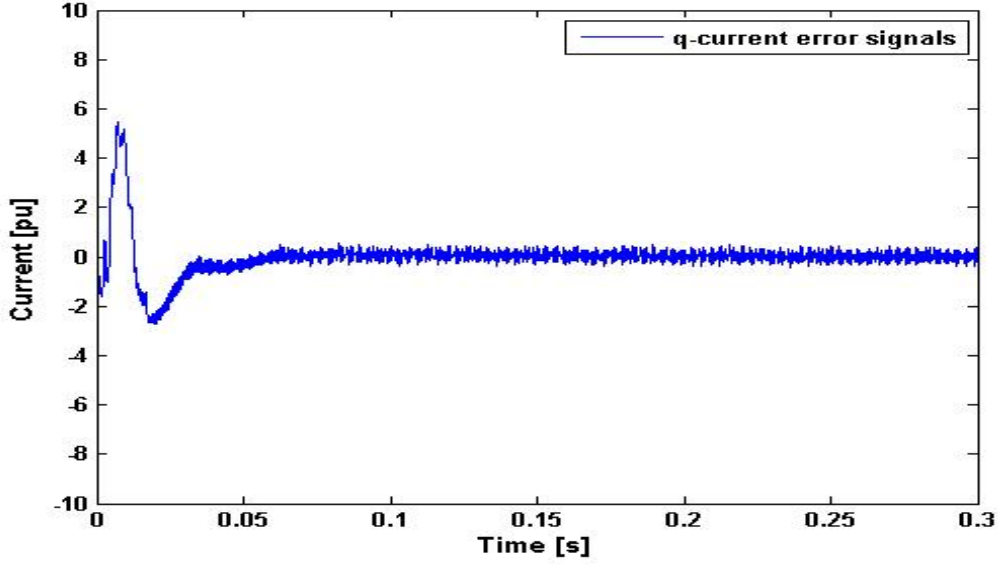
Figure 5.4: Error signal of the quadrature current axis at simulation start-up

larger than $45°$. Hence, a is chosen equal to 3. We can calculate:

$$T_{iv} = a^2 T_{eq} = a^2 2T = a^2 \frac{2}{2fs} = 3^2 \frac{1}{2000Hz} = 0.0045s \qquad (5.7)$$

By inserting the tuning of K_{pv} the open loop transfer function can be simplified to:

$$h_{0,vc}(s) = \frac{1}{\sqrt{T_{iv}T_{eq}}}(\frac{1+T_{iv}s}{T_{iv}s})(\frac{1}{1+T_{eq}s})\frac{1}{s} \qquad (5.8)$$

Thus, by simplifying:

$$h_{0,vc}(s) = \frac{1+0.0045s}{3.375 \cdot 10^{-9}s^3 + 6.75 \cdot 10^{-6}s^2} \qquad (5.9)$$

Hence, the bode plot of the open loop transfer function of the outer voltage controller is drawn in figure 5.5.

The phase margin is found to be $53.1°$ and the gain margin is again infinite. The phase margin can also be calculated analytically from equation (3.54):

$$\psi_m = \arctan{(a)} - \arctan{(\frac{1}{a})} = \arctan{(3)} - \arctan{(\frac{1}{3})} = 53.1° \qquad (5.10)$$

The transient start-up excitation of the DC-link voltage is depicted in figure 5.6. Similarly to previous plots, it experiences a small overshoot followed by an oscillation below the control value before stabilizing just before $0.05s$.

38
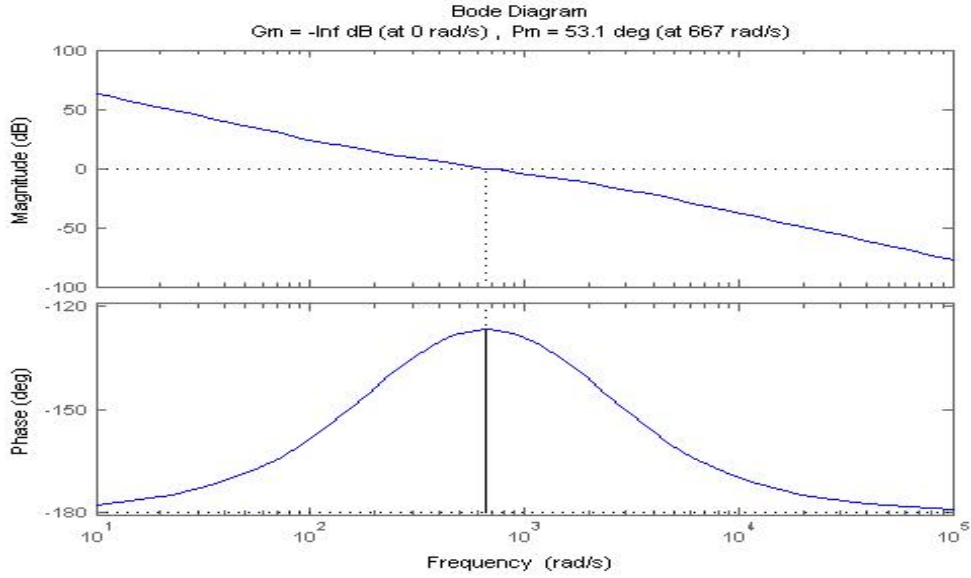
Figure 5.5: Bode plot of the open loop transfer function of the outer voltage controller
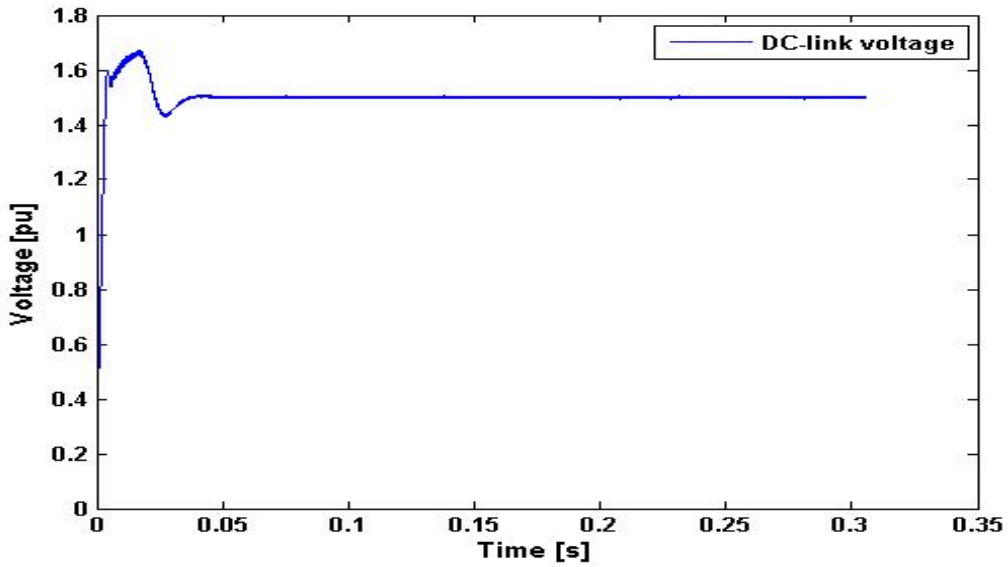
Figure 5.6: Transient response of the DC-link voltage at simulation start-up

5.2.3 DC-DC Current Controller

When inserting the tuning criteria of the DC-DC converter current control, its open loop transfer function can be simplified to:

$$h_{0,sc}(s) = \omega_0^2 \frac{(1 + T_{isc}s)}{s^2} \tag{5.11}$$

With $\omega_0 = \frac{2\pi f_{dc}}{10} = 6283 \frac{rad}{s}$, $T_{isc} = \frac{2\zeta}{\omega_0} = 2.25 \cdot 10^{-4}s$, we get:

39

$$h_{0,sc}(s) = \frac{1 + 2.25 \cdot 10^{-4}s}{0.25 \cdot 10^{-7}s^2} \tag{5.12}$$

Figure 5.7: Bode plot of the open loop transfer function of the DC-DC current controller

The error signal of the dc-dc converter current is given in figure 5.8. The signal starts off with a large error before eliminating the error at around $0.06s$.

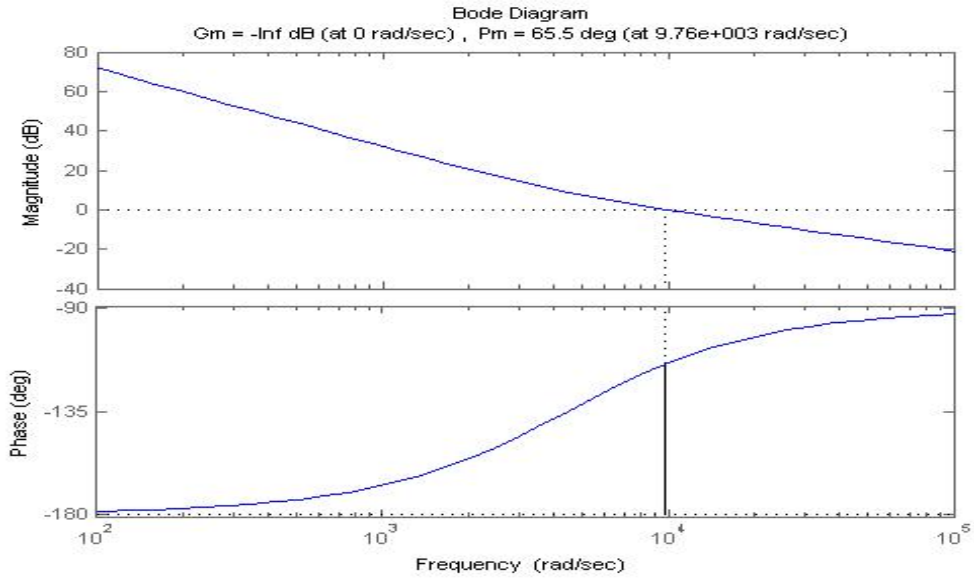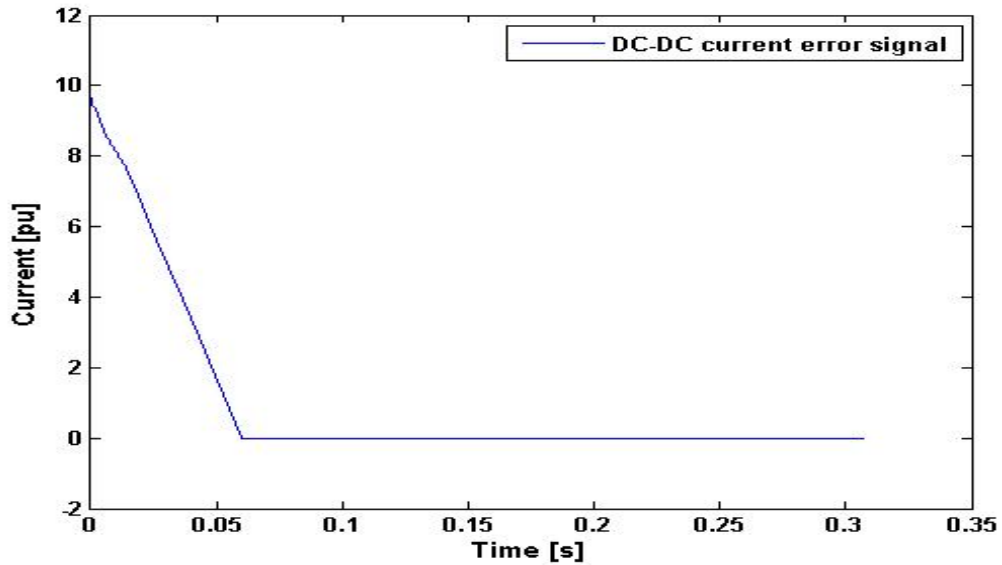Figure 5.8: Bode plot of the open loop transfer function of the DC-DC current controller

Table 5.2: Design wave characteristics

Description	Parameter	Value
Significant wave height	H_s	$2.5m$
Wave period	T_w	$6.5s$
Incoming wave angle	θ	$45 \circ$

5.3 Simulation Results for Peak-to-Average Ratio $k = 2$

The simulation results in are performed for a power series under a design wave state. The power series are depicted in figure 4.3 and the design wave state is defined in table 5.2. For comparison, selected simulation results for a constant grid power ($k = 1$) and without energy storage are provided in appendix B.2. and B.3.
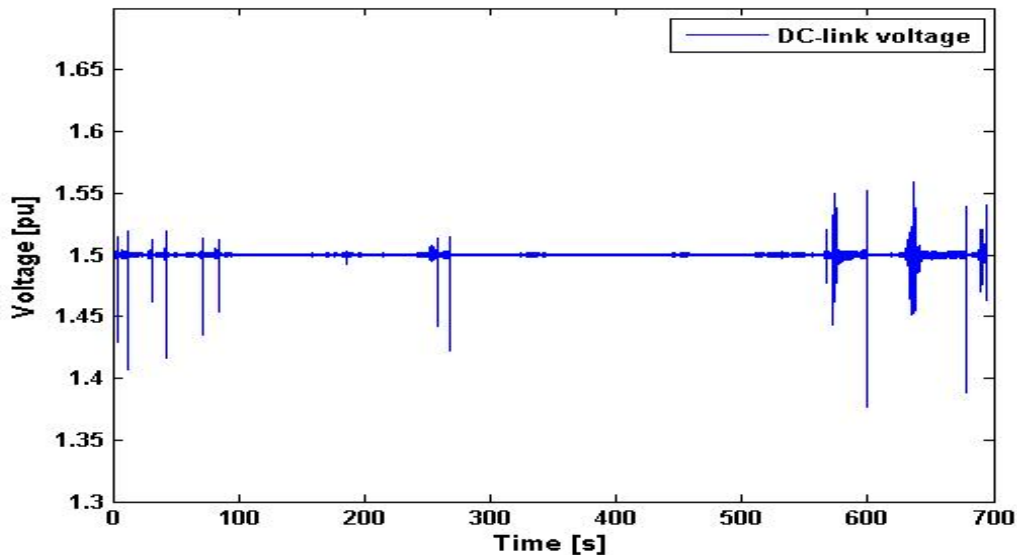
Figure 5.9: DC-link voltage

Figure 5.9 shows the DC-link voltage. It remains stable around $1.5pu$ throughout the simulation time. The extent of voltage ripple varies but never exceeds $0.05pu$. Sporadic voltage spikes can be observed where the largest deviation from the control value is around $0.15pu$.

The power output to the grid is found by multiplying the DC-current fed to the grid side converter with the DC-link voltage and is documented in figure 5.10. Since, the current follows a switching pattern the current is averaged over the switching frequency before the grid power is calculated. As for the DC-link voltage, ripple content exists throughout the simulation where the largest ripple amplitude is around $1pu$. Power
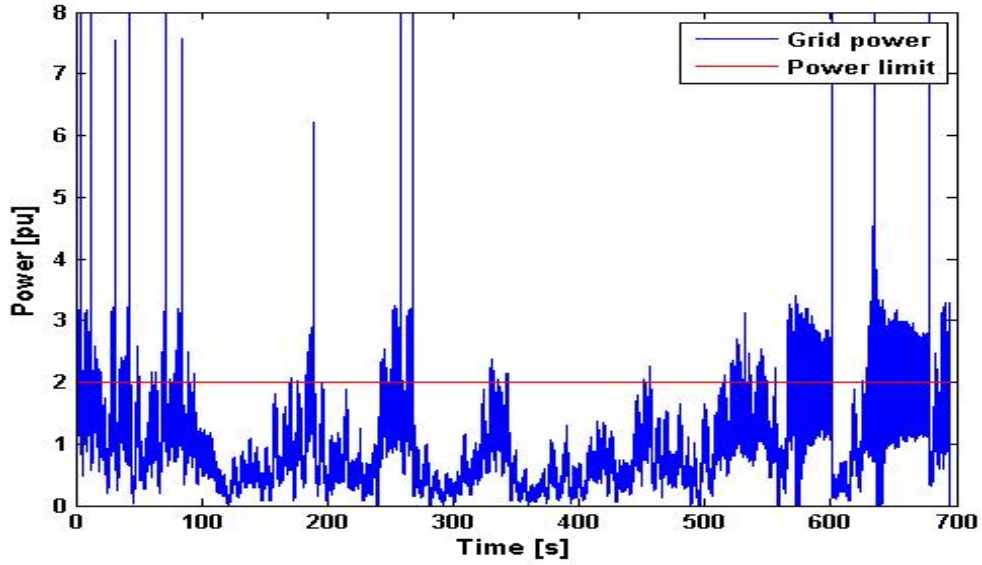
Figure 5.10: Power outputted to the grid

spikes are present and it should be noted that the power spikes occur simultaneously with the DC-link voltage spikes.
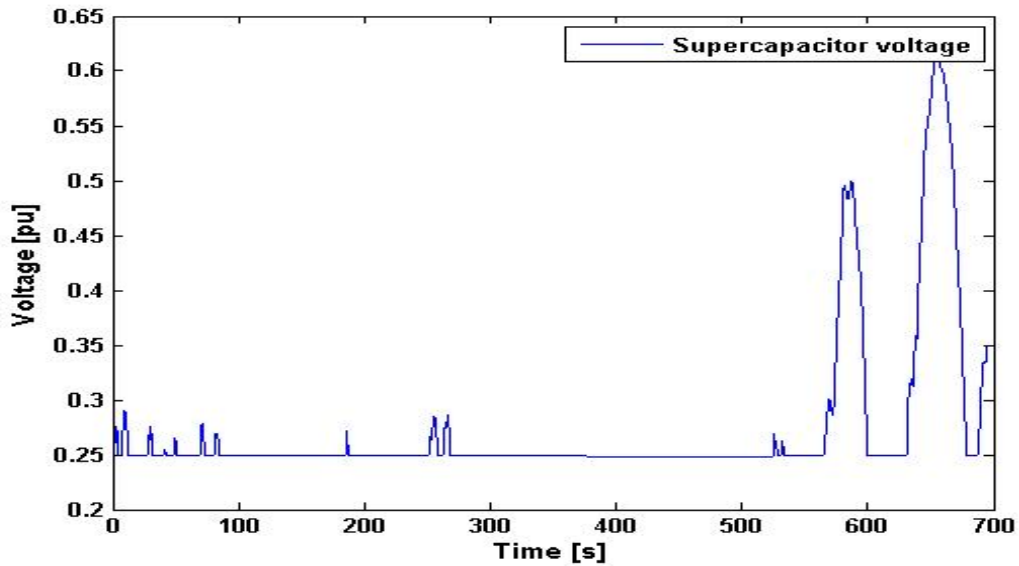
Figure 5.11: Supercapacitor voltage

The supercapacitor voltage level is depicted in figure 5.11. The supercapacitor voltage shows occasional voltage increases directly followed by an almost identical voltage decrease. The maximum supercapacitor voltage occurs at around $660s$ and attains $0.6pu$. Otherwise the voltage remains stable at $0.25pu$. Between $300s$ and $500s$, a minor voltage decrease can be detected.

42
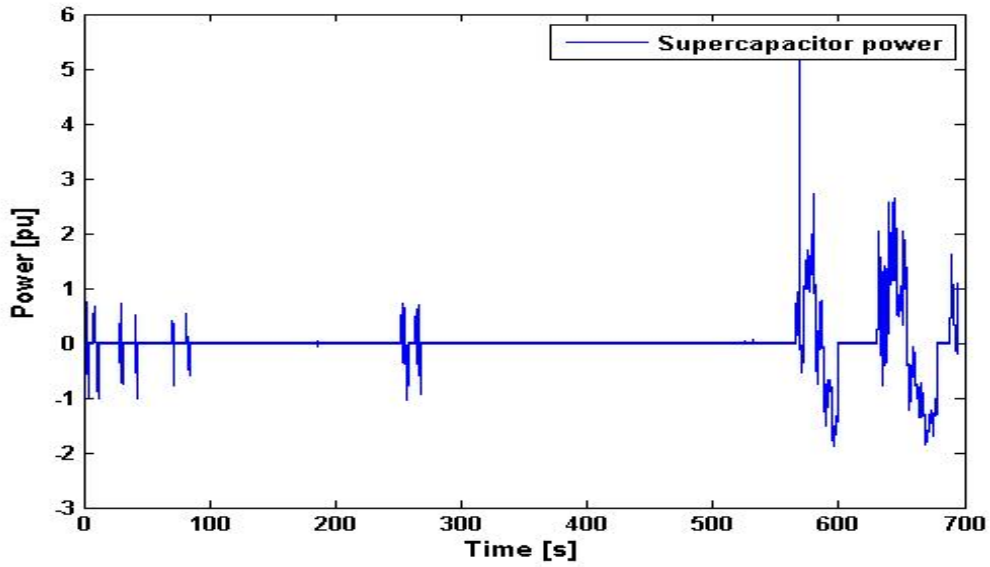
Figure 5.12: Supercapacitor power

The supercapacitor power output is depicted in figure 5.12. In this thesis, the power is defined as positive when flowing into the supercapacitor bank, and negative when flowing out. The figure shows a power output that is 0 for most of the simulation. Positive power intervals are always succeeded by negative power intervals. By comparing with figure 5.11, the positive power intervals reflects the supercapacitor voltage increase and similarly the negative power represents the supercapacitor voltage decrease.
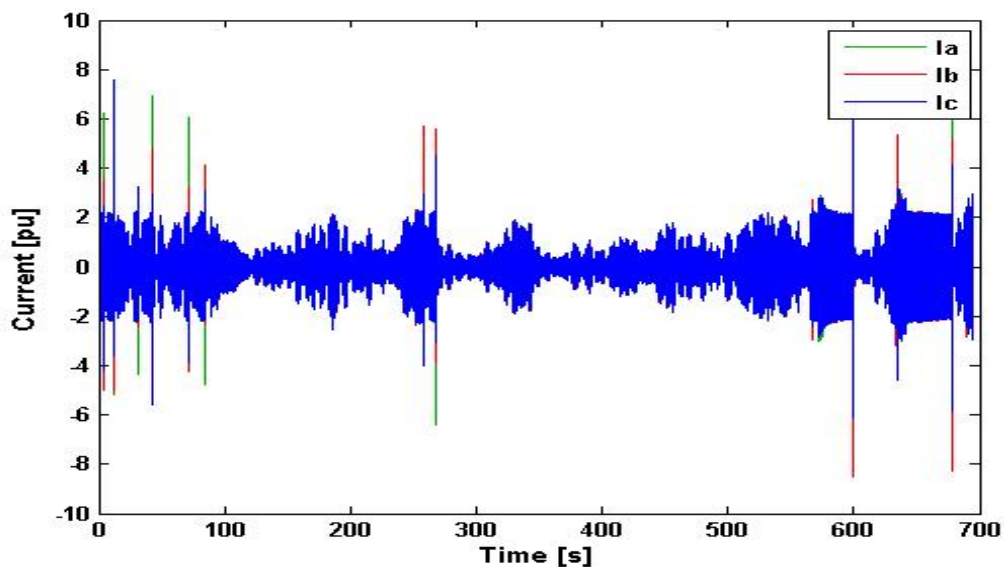
Figure 5.13: Grid side currents

The grid side currents are documented in figure 5.13 and also contains current spikes.

43
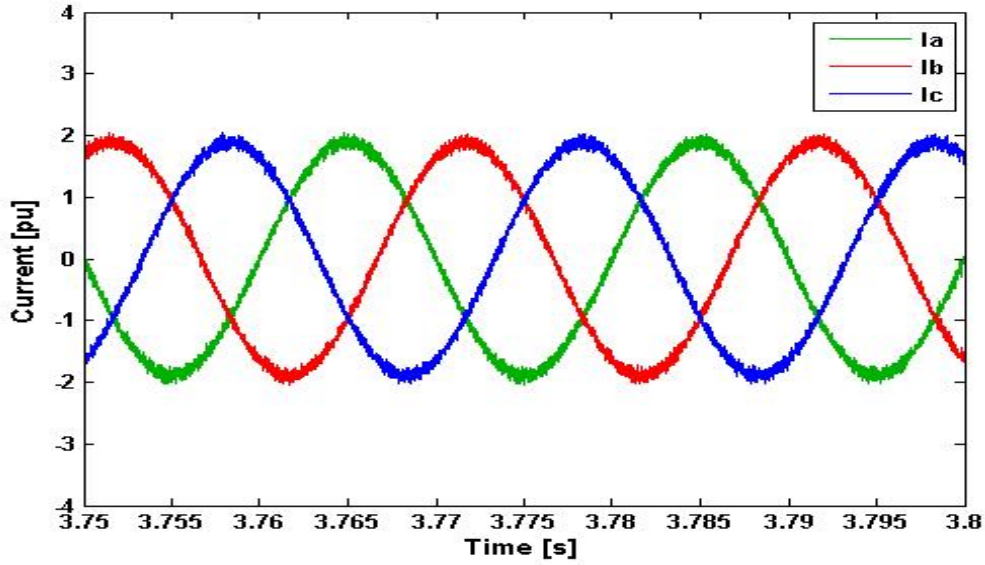
Figure 5.14: Close-up of grid side currents

To get a better impression of the grid side currents waveforms, a close-up picture is provided in figure 5.14. The currents are nearly sinusoidal with some harmonic content with an amplitude just below $2pu$. As a reference, the grid side voltages are given in figure 5.15 for the same time frame. The frequency of the grid side currents can be calculated:

$$f = \frac{1}{3,775s - 3,755s} = 50Hz \tag{5.13}$$

In addition it can be seen from figure 5.15 that the voltages and currents are in phase. Hence, there is no reactive power exchange at this point.
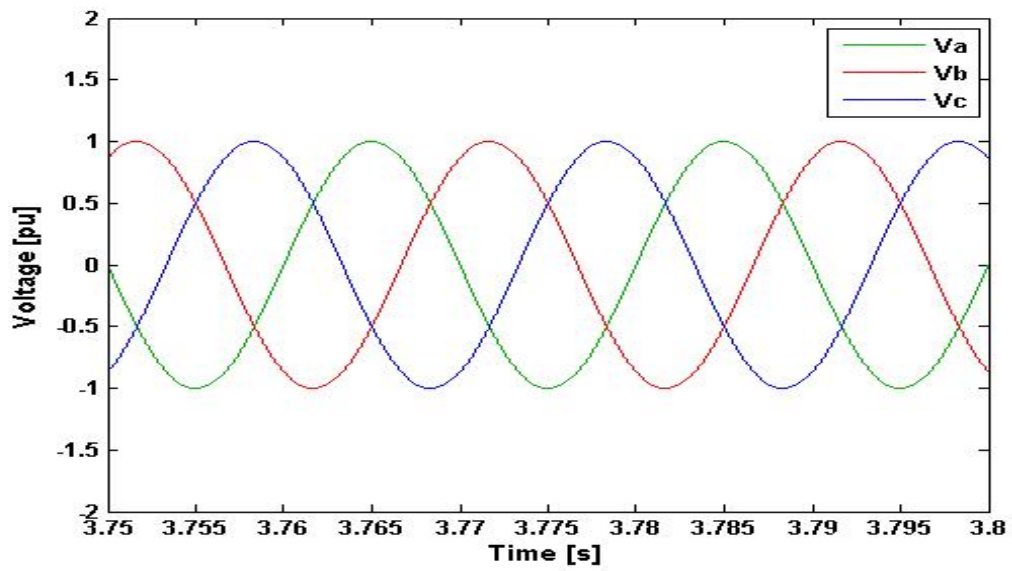
Figure 5.15: Close-up of the grid side voltages

Chapter 6

Discussion

The controllers' performance were examined in section 5.2. All controllers had phase margins above the cited criterion of 45° with infinite gain margins. Further the maximum response time was recorded to be $0.06s$. Hence, all criteria established in section 3.4 were fulfilled and the tuning of the controllers must be deemed successful and should provide a good basis for further simulations.

By inspecting the plots in chapter 5, large spikes are found throughout the system. They have in common that they are instantaneous and deviate a lot from their expected value. In addition they seem to occur simultaneously throughout the system and the cause is therefore suspected to be common. By investigating figure 5.10, the power spikes are taking place when the power suddenly drops. In other words, when the ESS is completely discharged. At this time the current reference is discontinuous and suddenly changes from a given value to 0. It might be expected that this discontinuity in the current is the source for the spikes. However, when inspecting the plots in appendix B.2, which shows the simulation results for a constant grid power ($k = 1$), the same spikes can be observed. For that case, the current is continuous and thus, the discontinuity cannot be the reason for the spikes but would have to be due to the zero-crossing of the DC-DC current. Therefore, a possible solution would be to analyse the DC-DC converter in discontinuous conduction mode for the zero-crossings. Nevertheless, the spikes are considered to be of low importance as they contain very little energy and will therefore be disregarded.

The DC-link is kept stable around the control voltage which indicates that the grid side converter control system operates satisfyingly. The voltage ripples increases when large amount of power is injected onto the DC-link. A remedy for this, would be to increase the DC-capacitor. Nevertheless, the voltage fluctuations are deemed minor and short and seem acceptable for the operation of the system.

46

The power outputted to the grid in figure 5.10 is measured at the DC side of the converter. Although the power is set not to exceed $2pu$, the power ripples reaches above $3pu$. The power is composed by a quite stable voltage and a highly distorted current which reflects the power oscillations above and below $2pu$. However, if figure 5.13 is examined, the grid side current peaks seem to be cut more sharply just above $2pu$, which represents the power limit at the AC-side. The AC currents have been smoothed out by the grid side filter and contain a lot less harmonics than on the DC-side. The effect is clearer when comparing with figure B.14, which shows the grid side currents without any energy storage. This would indicate that the power has been successfully limited to the set peak-to-average ratio. It could be expected that even better results would be achieved if the harmonic distortion of the currents in the system were further reduced.

The supercapacitor voltage increases when the DC-DC converter operates in boost charging mode and is characterized by a positive power profile in figure 5.12. Consequently, as soon as the wave power drops below the power limit, the ESS discharges to keep the power output constant at the power limit and the voltage decreases. The slight voltage decrease that can be observed in figure5.11 between $300s$ and $500s$ is consistent with the control system. Although the voltage should ideally be constant at this point, a minimal voltage decrease was allowed to prevent the voltage from rising. Hence, the operation of the ESS is confirmed by figure 5.12 and 5.11.

Chapter 7

Conclusion

7.1   Contributions of the Work

The goal for this thesis was to develop a model of a grid side converter with an energy storage system for a wave energy converter. The final model is intended to serve as a useful tool when performing analyses regarding grid connecting of WECs, or as a part of a detailed wave-to-wire model of a WEC.

The control scheme of the grid side converter was designed with vector control and was designed to maintain a constant DC-link voltage and to ensure no reactive power exchange at the converter output. The simulations proved that system response was fast and with no steady state error. This resulted in a stiff DC-link and grid side currents were injected in phase with the voltage at the rated frequency.

An energy storage system was considered for power smoothing purposes and supercapacitors were designated as the energy storage device. From practical experience, supercapacitor storage systems are unsuited for smoothing out the power completely because of elevated costs. A different approach was therefore envisaged, where the energy storage absorbs the power variations larger than a given peak-to-average ratio. Indeed, with a peak-to-average ratio of 2, the required supercapacitor capacitance could be reduced by a factor of 4.8. The storage was interfaced to the DC-link through a bi-directional DC-DC converter and current control was applied to provide the desired power dispatch from the supercapacitor.

Some concern was raised for transient spikes observed in the simulations, due to the zero-crossing of the energy storage current. Otherwise, the model demonstrated satisfying operation and consistency for long simulation times.

7.2 Further Work

- The next step would be to perform an economical optimization study where the savings from providing a smoother power would have to outweigh the costs from integrating an energy storage system.

- A significant improvement would be to reduce the simulation steps of the model without losing significant amount of accuracy and maintaining stability. As of now, the model has a simulation step time of $1e-5s$ whereas the total simulation time is around $700s$. This creates very large simulation data files which can be several hundreds of MB and makes it quite troublesome and tedious to work with and manipulate.

- When the inductor current drops to zero in the DC-DC converter, the control law changes and the circuit should be analysed in discontinuous conduction mode which has been disregarded in this thesis. It is possible that the transient spikes that are recurrent throughout the model might be solved with this approach.

- An outer reactive power controller could be included to the grid side converter control system to provide the reference current for the $q-axis$. The approach is similar to the outer voltage controller and was therefore not treated in the thesis.

- To gain a better understanding of the interaction with the grid, it is advised to extend the model to include the grid connection until the point of common coupling.

- The current ratings of the supercapacitors or the IGBTs have not been considered. This is especially relevant for the DC-DC converter where the current through a single switch can be very high since a two switch topology is considered. Depending on the rating of the energy storage device, a bridge topology could be considered. Still, the principles outlined in this thesis are also transferable to a bridge topology.

- Harmonics have not been a priority other than applying a single inductance filter at the grid side in order to approximate sinusoidal conditions. To further reduce the harmonics content, it is suggested to introduce a LCL-filter (two inductors in series and a shunt capacitor) as a grid filter. In addition, the size of the inductor could be reduced according to [31].

Bibliography

[1] K. Gunn, C. Stock-Williams, "Quantifying the global wave power resource", Renewable Energy, 2012

[2] European Comission, "The EU climate and energy package - The 20-20-20 targets", $http : //ec.europa.eu/clima/policies/package/index\_en.htm$

[3] MaRINET - Marine Renewables Infrastructure Network for Emerging Energy Technologies - $www.wavetrain2.eu$

[4] WAVETRAIN 2 - Initial Training Network for Wave Energy Research Professionals - $www.wavetrain2.eu$

[5] MARINA Platform - Marine Renewable Integrated Application Platform - $www.marina - platform.info$

[6] TROPOS - Modular Multi-use Deep Water Offshore Platform Harnessing and Servicing Mediterranean, Subtropical and Tropical Marine and Maritime Resources - $www.plocan.eu$

[7] Biscay Marine Energy Platform, $http : //www.eve.es/energia\_marina/index\_ing.htm$

[8] D. O'Sullivan, G. Dalton, "Challenges in the Grid Connection of Wave Energy Devices", Hydraulics and Maritime Research Centre, University College Cork, Ireland, 2003

[9] H. Polinder, M. Scuotto, "Wave Energy Converters and their Impact on Power Systems"

[10] J. B. Ulvin, M. Molinas, J. Sjolte "Analysis of the Power Extraction Capability of the Wave Energy Converter BOLT", Technoport, RERC, 2012

[11] C. Sandvik, "Wave-to-wire modelling of the Wave Energy Converter BOLT", Master's thesis, NTNU, 2012

[12] J. Sjolte, G. Tjensvoll, M. Molinas, "All-Electric Wave Energy Converter with Standalone 600VDC Power System and Ultracapacitor Bank", EVER12, Monaco, 2012

[13] Wave Hub, $http://www.wavehub.co.uk/$

[14] South West of England Regional Development Agency, "WEC Connection Specification, Wave Hub" Revision number 4, 2011

[15] Cuiqing Du, "The Controls of VSC-HVDC and its use for Large Industrial Power Systems", Thesis for the Degree of Licentiate of Engineering, Chalmers University of Technology, 2003

[16] Sverre Skalleberg Gjerde, "STATCOM and Energy Storage in Grid Integration of Wind Farms", Master's thesis, 2009,

[17] Robert Nilsen, "Electrical Motor Drives/Elektriske Motordrifter" (In Norwegian), Compendium, Department of Electrical Power Engineering, NTNU, 2005

[18] C. Bajracharya, "Control of VSC-HVDC Wind Power", Master's Thesis, NTNU, 2008

[19] T. M. Haileselassie, "Control of Multi-terminal VSC-HVDC Systems", Master's Thesis, NTNU, 2008

[20] J. G. Balchen, T. Andresen, B. A. Foss, "Control Engineering/Reguleringsteknikk (In Norwegian), NTNU, 2003

[21] Ned Mohan, "Electric Drives - An Interactive Approach", MNPERE, Minneapolis, 2003

[22] J. Sjolte, G. Tjensvoll, M. Molinas, "All-Electric Wave Energy Converter Connected in Array with Common DC-link for Improved Power Quality", NTNU, 2012

[23] J. Aubry, P. Bydlowski, B. Multon, H. Ben Ahmed, B. Borgarino, "Energy Storage System Sizing for Smoothing Power Generation of Direct Wave Energy Converters", Bilbao, ICOE 2010

[24] D. B. Murray, M. G. Egan, J. G. Hayes, D. L. O'Sullivan "Applications of Supercapacitor Energy Storage for a Wave Energy Converter System", University College Cork

[25] Chad Abbey, Geza Joos, "Supercapacitor Energy Storage for Wind Energy Applications", IEEE Transactions on Industry Applications, Vol. 43, No. 3, May/June 2007

[26] $http://www.cap-xx.com/resources/reviews/pwr-v-enrgy.htm$

[27] Madhavi Srinivasan, "Supercapacitors", MS4526 - Photovoltaics and Energy Storage, Nanyang Technological University, 2011

[28] D. B. Murray, J. G. Hayes, D. L. O'Sullivan, M. G. Egan, "Supercapacitor Testing for Power Smoothing in a Variable Speed Offshore Wave Energy Converter", IEEE Journal of Ocean Engineering, Vol. 37, No. 2, April 2012

[29] M. B. Camara, H. Gualous, F. Gustin, A. Berthon, "Design and New Control of DC/DC Converters to Share Energy Between Supercapacitors and Batteries in Hybrid Vehicles", IEEE Transactions on Vehicular Technology, Vol. 57, No. 5, September 2008

[30] G. Xu, L. Xu, D. J. Morrow, "Wind Turbines with Energy Storage for Power Smoothing and FRT Enhancement"

[31] V. Valdivia, J. Pleite, C. Gonzalez, R. A. Salas, "New approach to integrate an LCL filter and a transformer for grid connected converters following a simple design procedure"

[32] Mohan, Undeland, Robbins, "Power Electronics Converters, Applications and Design", John Wiley and Sons, 2003

[33] R. W. Erickson, "DC-DC Power Converters", Wiley Encyclopedia of Electrical and Electronics Engineering

[34] *www.wikipedia.org*

Appendix A

Simulink Subsystems

A.1 DC-DC Control System
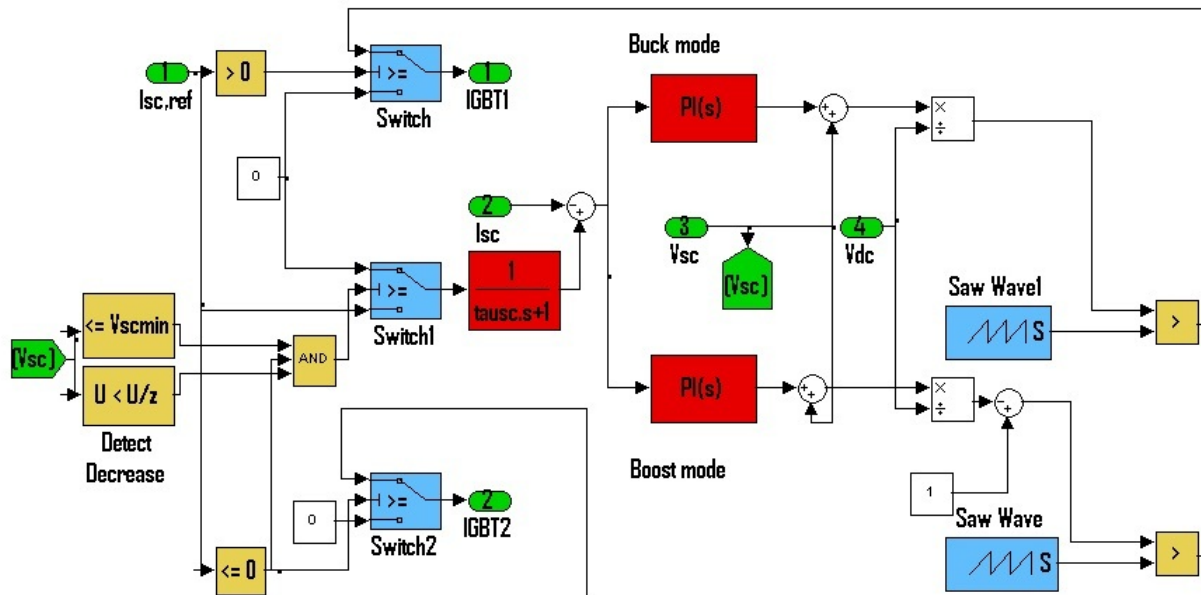
Figure A.1: Simulink control system of the DC-DC converter

A.2 Grid Side Control System

Figure A.2: Simulink control system of the grid side converter

(a) Current controller

(b) Voltage controller

Figure A.3: Caption of subfigures (a), (b)

Appendix B

Additional Simulation Results

B.1   Additional Simulation Results For Peak-to-Average Ratio $k = 2$
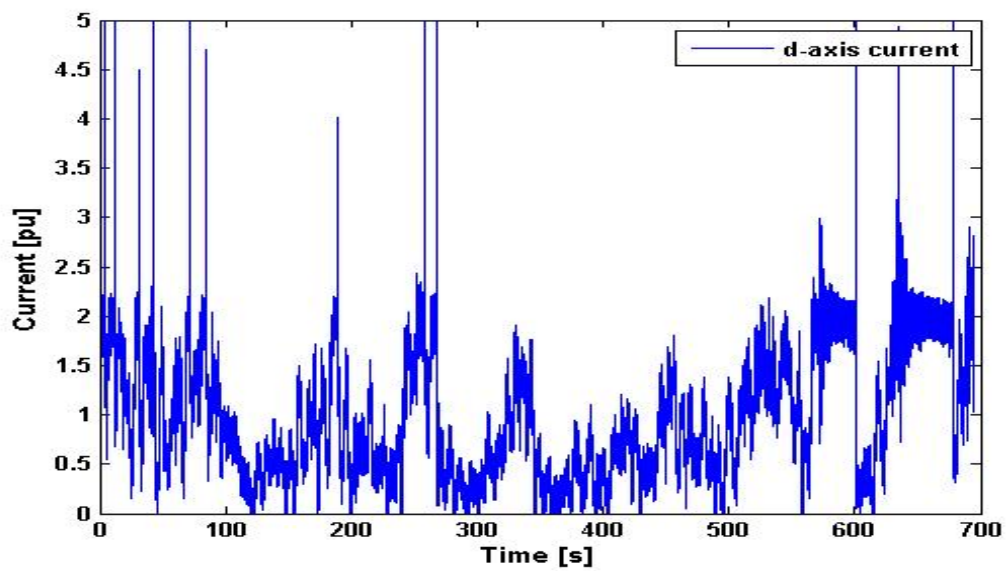
Figure B.1: d-axis current
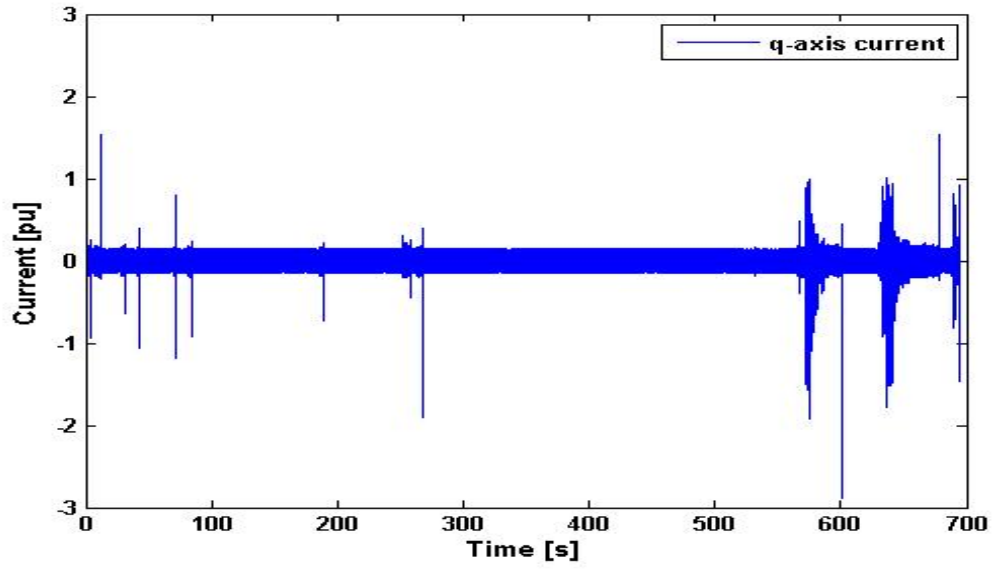
Figure B.2: q-axis current
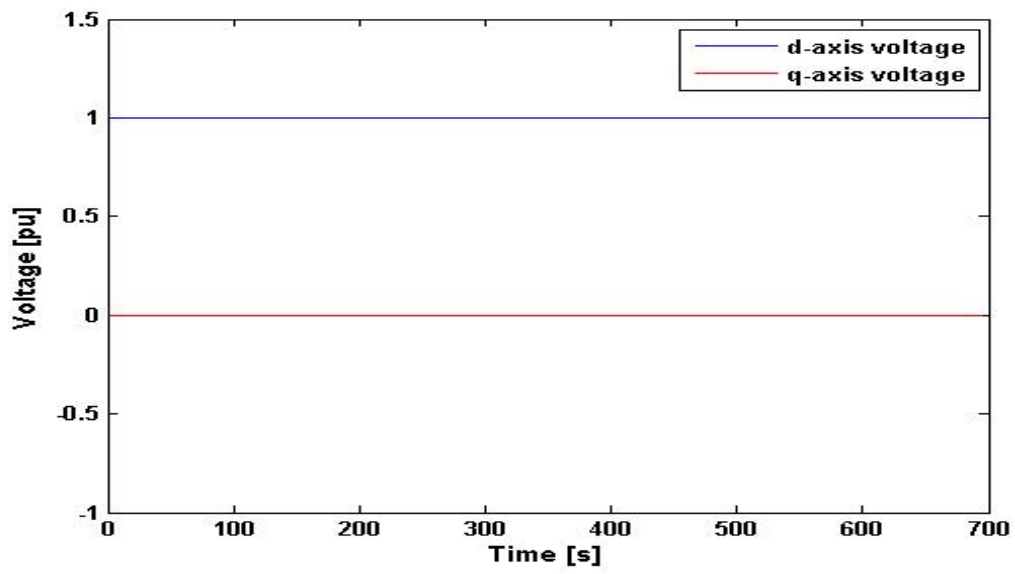
Figure B.3: d-axis voltage and q-axis voltage
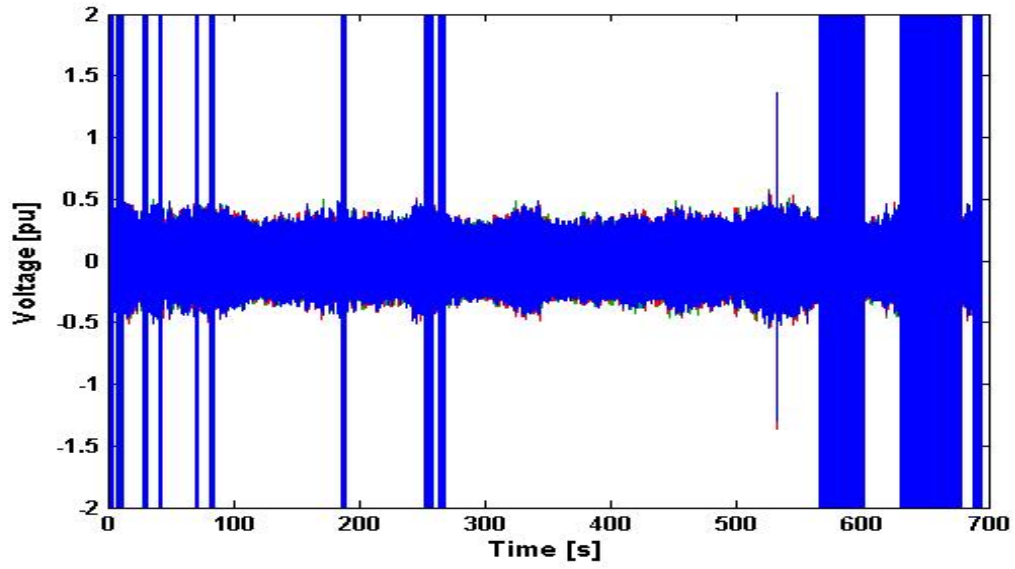
Figure B.4: Sinusoidal PWM signals
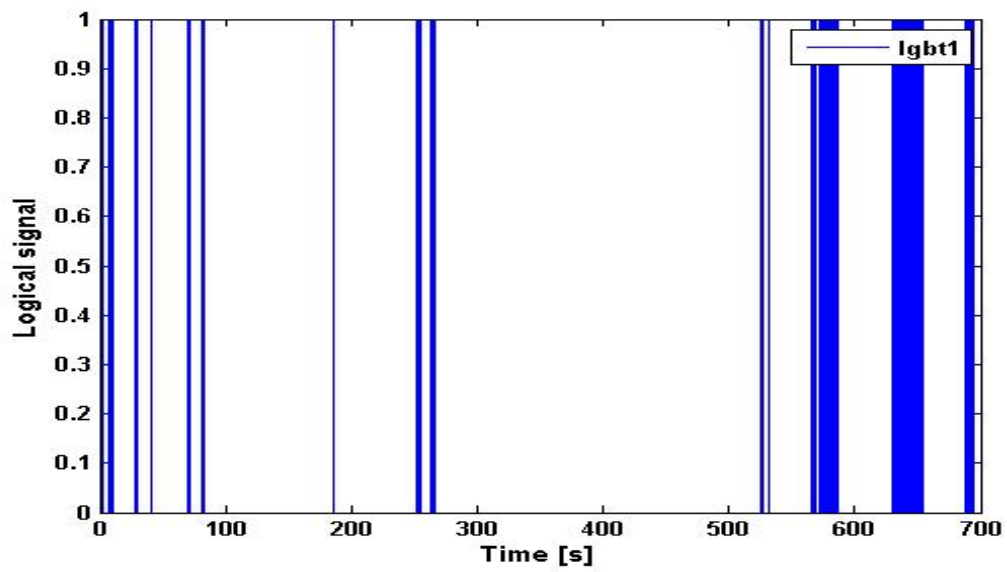
Figure B.5: Gating signal Igbt1
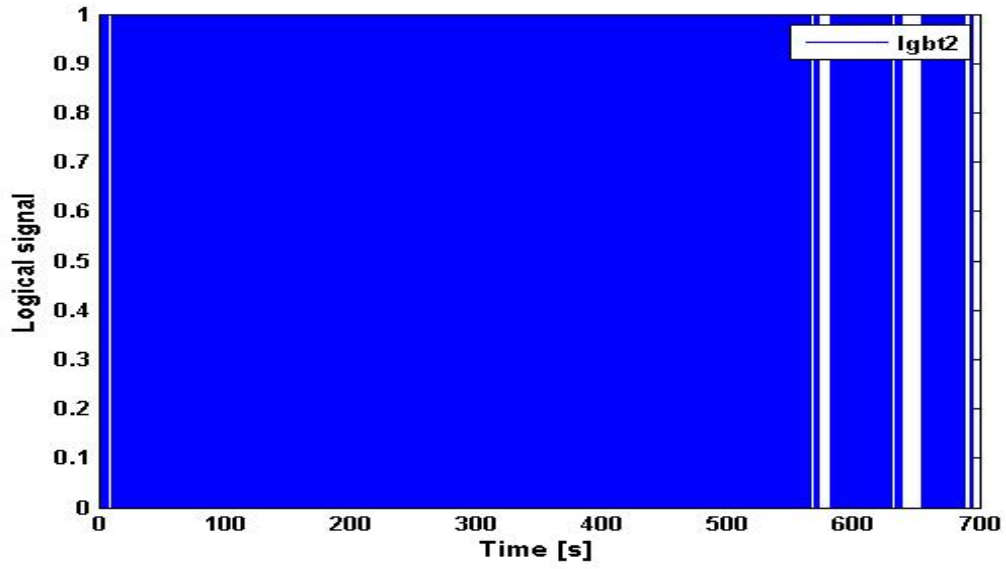
Figure B.6: Gating signal Igbt2

B.2   Simulation Results with Constant Grid Power
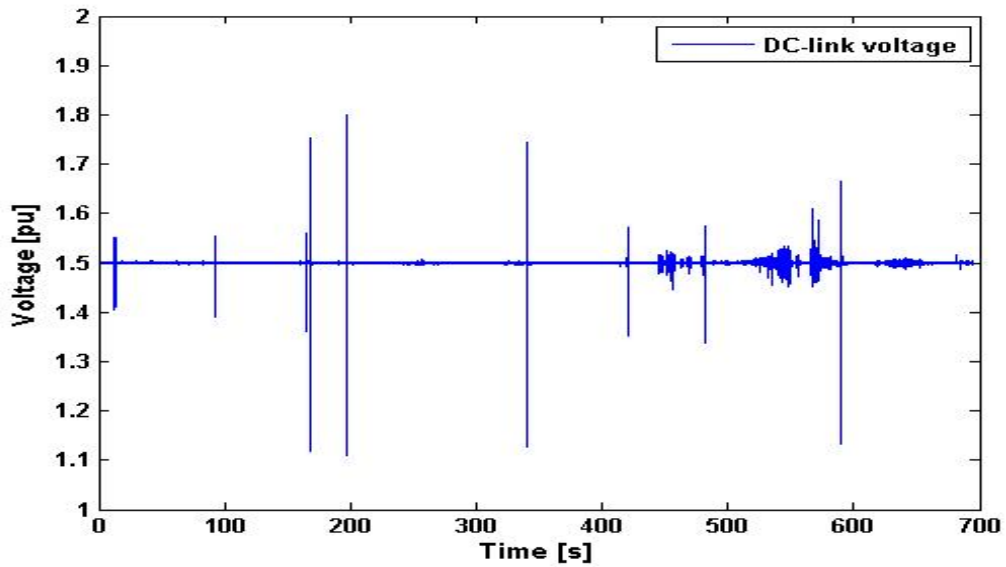
Figure B.7: DC-link voltage
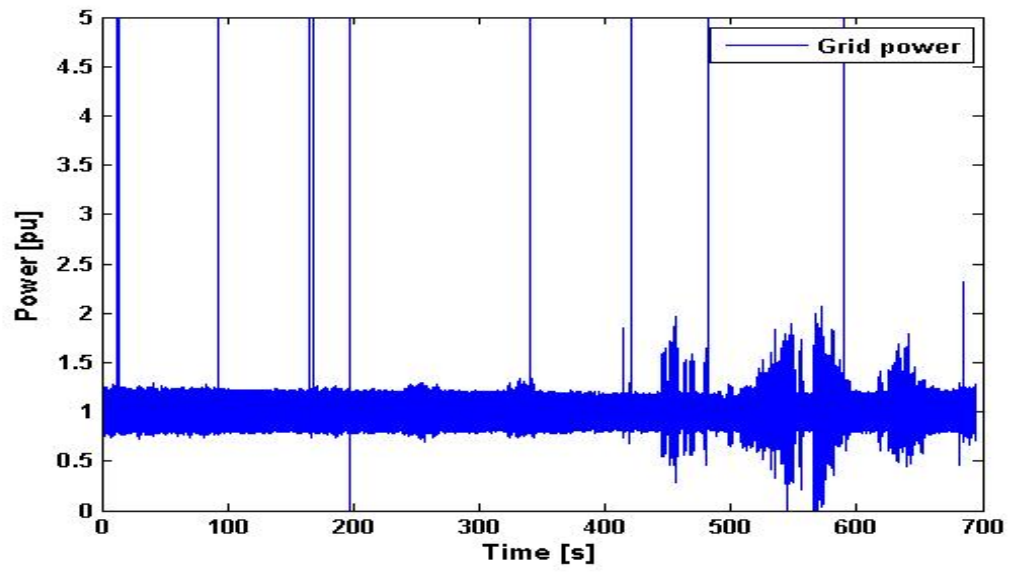
Figure B.8: Grid power
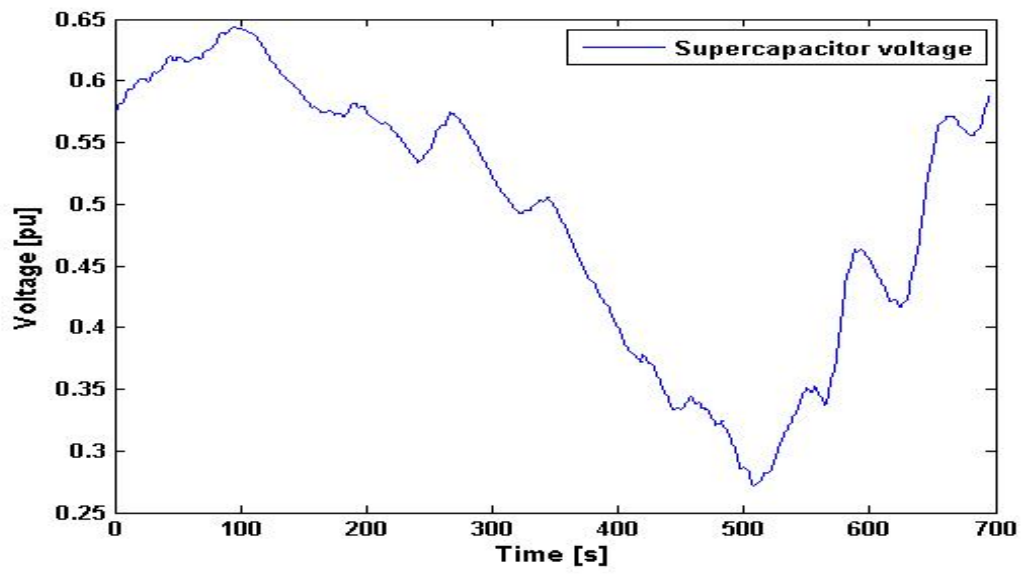
Figure B.9: Supercapacitor voltage
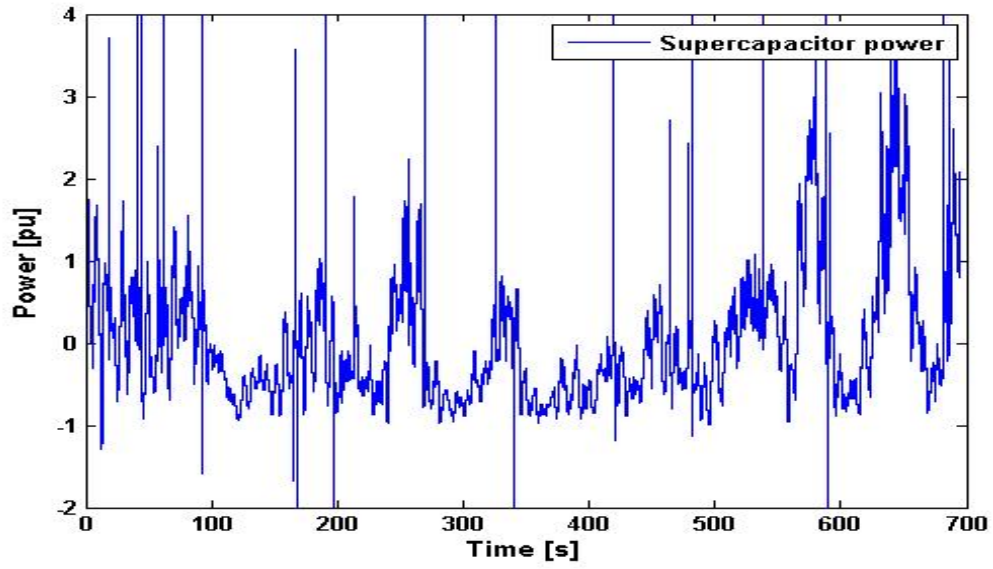
Figure B.10: Supercapacitor power
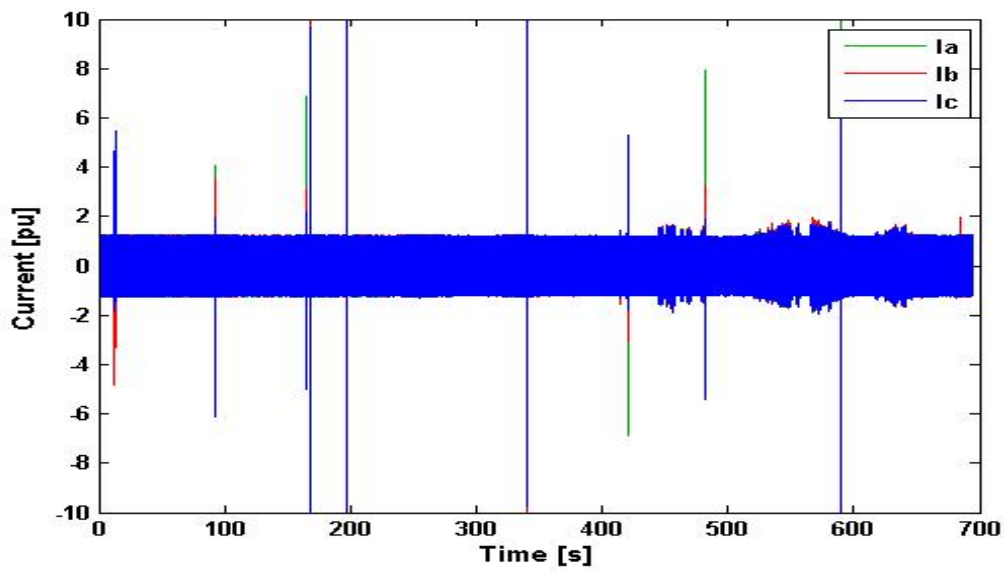
Figure B.11: Grid side currents

B.3   Simulation Results without Energy Storage
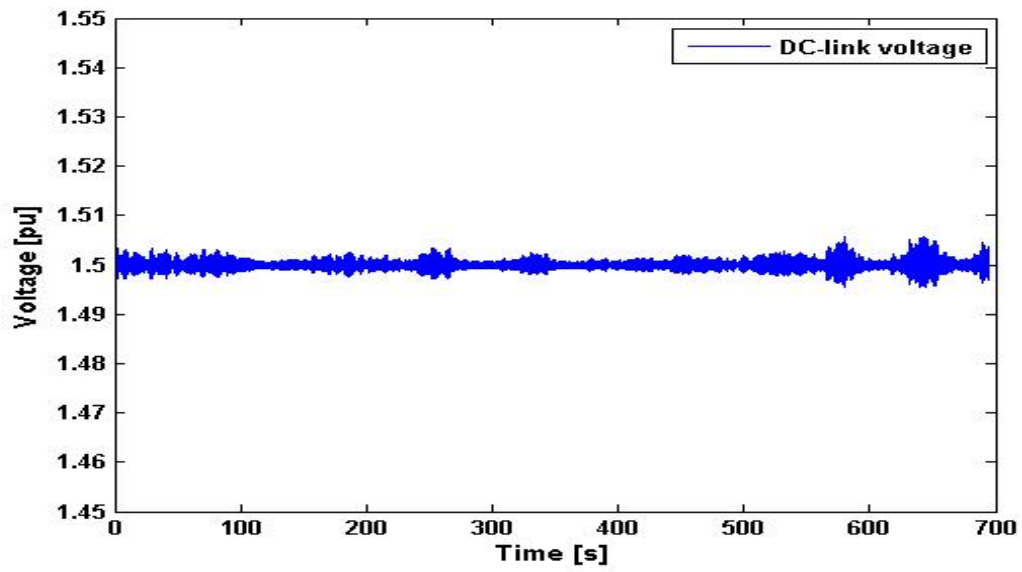
Figure B.12: DC-link voltage
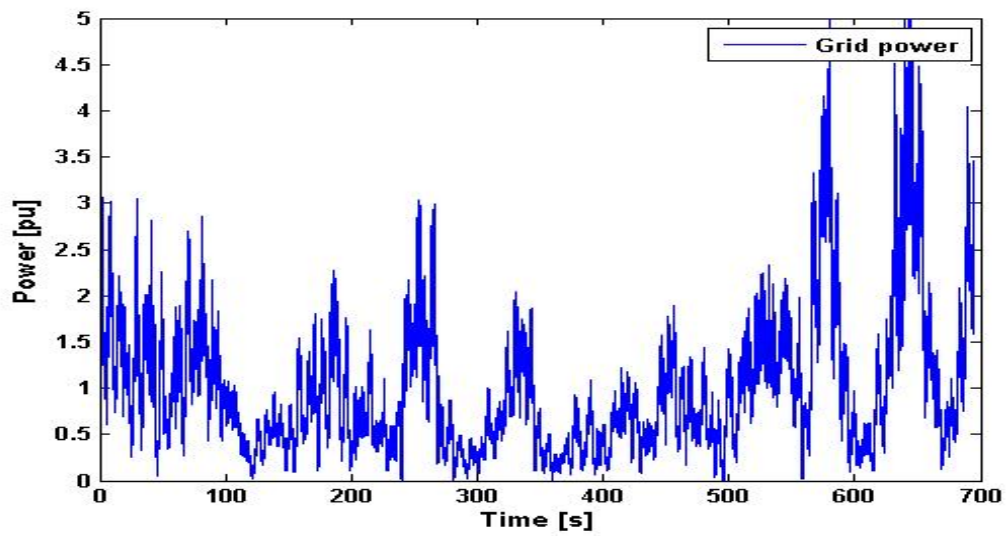
Figure B.13: Grid power
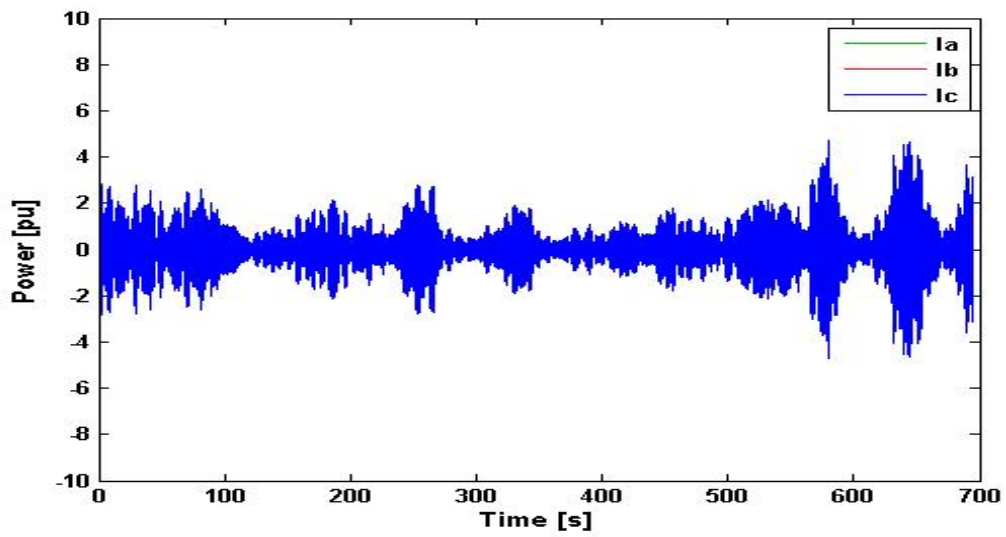
Figure B.14: Grid side currents

Appendix C

Power Electronics Fundamentals

C.1   AC-DC conversion

DC-AC inverters are used for transforming a DC power input to an AC power output.

C.1.1   Single-Phase Half Bridge DC-AC Inverter
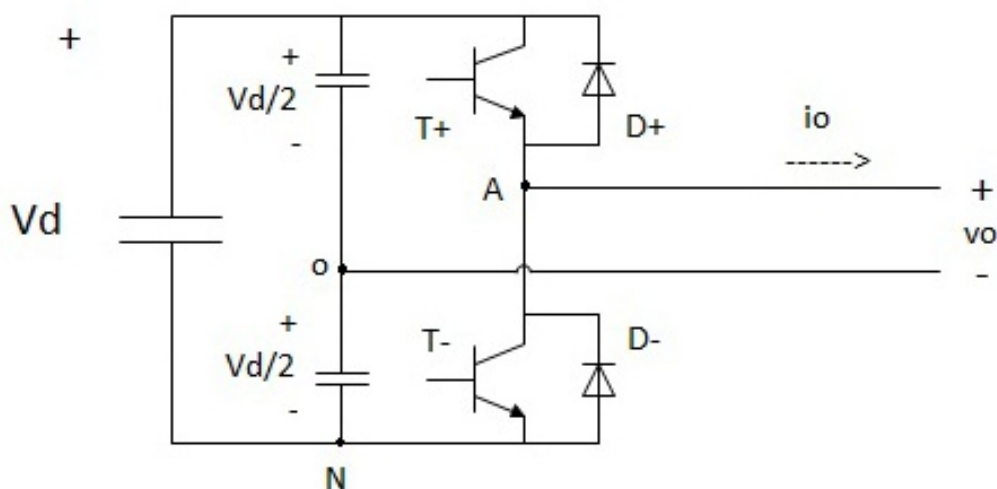
Figure C.1: Single Phase Half Bridge DC-AC Inverter

The simplest DC-AC inverter is the single-phase half bridge DC-AC inverter, depicted in figure C.1. It consists of two power semiconductor switches, T+ and T-, and two anti-parallel diodes, D+ and D-. When T+ is conducting, T- is turned off. Then, the voltage output is: $v_o = \frac{V_d}{2}$. Similarly, when T- is conducting, T+ is turned off and the voltage output is: $v_o = \frac{-V_d}{2}$.

By inversely turning on and off the two semiconductor switches, an output AC square wave voltage can be created. The voltage magnitude is controlled by setting the input DC voltage. The frequency is controlled by varying the switching frequency of the switches, i.e. the ON and OFF periods of the switches.

Ideally, the objective of an inverter is to create a sinusoidal voltage output and not a square wave. By using Fourier series, the square wave can be decomposed into multiple sine waves with frequency $f_1, 2f_1, 3f_1, ...$ f_1 represents the fundamental component which the inverter ideally should produce. The rest of the components are referred to as harmonics and are viewed as disturbances to an ideal system. The harmonics can be suppressed either by using other modulation techniques, or changing the inverter topology to include more voltage switching levels.

C.1.2 Three Phase Full Bridge DC-AC Inverter

The three phase full bridge DC-AC inverter is the dominating topology for three-phase applications with a line-to-line voltage less than $1000V$ [17]. It consists of three half bridge inverters connected in parallel, as depicted in figure C.2.
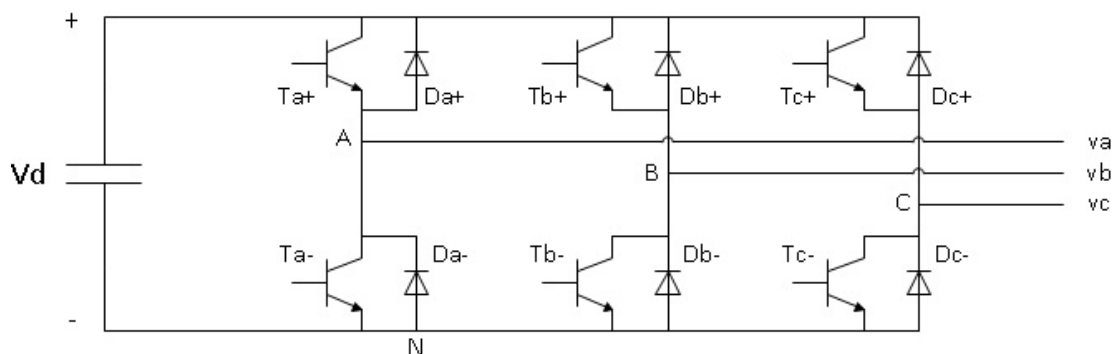
Figure C.2: Three Phase Full Bridge DC-AC Inverter

Previously, when power switches had quite large switching losses, the switching was controlled by using a technique called square wave modulation or six-step modulation. The six-step modulation is done by controlling the three sets of switches to conduct for half a period, 120 degrees shifted apart. This creates three voltage square waves in the three phases and a resulting three-level line-to-line voltage output. Six-step comes from the load phase voltage.

The RMS output line voltage is given by:

$$V_{L(rms)} = \sqrt{\frac{2}{3}} V_d \tag{C.1}$$

64

The nth harmonic amplitude is given as:

$$V_{Ln} = \frac{4V_d}{n\pi}cos(\frac{n\pi}{6}) \tag{C.2}$$

Hence the RMS fundamental voltage is:

$$V_{L1} = \frac{1}{\sqrt{2}}\frac{4V_d}{\pi}cos(\frac{\pi}{6}) = 0.7797V_d \tag{C.3}$$

The total harmonic distortion for such a modulation is given by:

$$THD = \frac{\sqrt{V_o^2 - V_1^2}}{V_1} = 31.08\% \tag{C.4}$$

Although the frequency of the output voltage could be altered quite easily by varying the switching period, another drawback to this modulation technique, in addition to the high contents of harmonics, was that the voltage output could only be controlled by varying the DC input voltage.

C.1.3 Sinusoidal Pulse Width Modulation (SPWM)

When the switching devices could handle more switching losses, Sinusoidal Pulse Width Modulation (SPWM) was introduced, where both the output frequency and the output voltage can be controlled as a result of the switching. The method is characterized by a very high switching frequency compared to the output voltage frequency. The switching frequency is determined by creating a high frequency triangle carrier wave. Further, three 120°-phase displaced reference sinus waves are compared to the common triangle carrier wave to create the switching pulses:

$$V_{control,A} = V_m cos(2\pi f_o t) \tag{C.5}$$

$$V_{control,B} = V_m cos(2\pi f_o t - 120°) \tag{C.6}$$

$$V_{control,C} = V_m cos(2\pi f_o t + 120°) \tag{C.7}$$

The technique is illustrated in figure C.3.

As long as $V_m < 1pu$ the RMS fundamental output voltage is given by [32]:

$$V_{L1} = \frac{\sqrt{3}}{2\sqrt{2}}V_d V_m \tag{C.8}$$
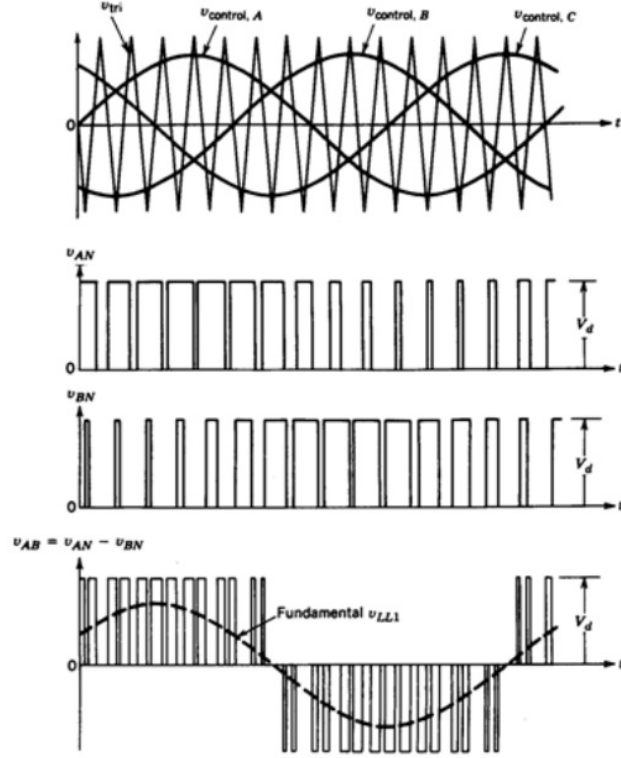
Figure C.3: Sinusoidal Pulse Width Modulation [32]

C.2 DC-DC conversion

The DC-DC converter can be used as a voltage regulator to convert an unregulated dc voltage to a regulated dc output voltage and to connect to different dc voltage levels. High efficiency is invariably required, since cooling of inefficient power converters is difficult and expensive. However in practice, efficiencies of 70 to 95 per cent are typically obtained [33]. Still, for simplicity, the converters in this thesis are assumed lossless. Usually the DC-DC converter contains at least two semiconductor devices. Filters are often added to the converter's output to improve performance. PWM allows control and regulation of the total output voltage.

A common term used when talking about DC-DC converters is the duty cycle, D, which is defined as the ratio between the ON-time of the switching device and the total switching period:

$$D = \frac{t_{on}}{T_s} \tag{C.9}$$

Further, DC-DC converters are inductance based switching devices where energy is stored and released throughout a switching cycle. The voltage across an inductor is given by:

$$V_L = L\frac{di_L}{dt} \tag{C.10}$$

The energy stored in an inductor is given as:

$$E = \frac{1}{2}Li_L^2 \tag{C.11}$$

When analysing the converter circuits, continuous conduction mode (CCM) is assumed. This means that the minimum inductor current never falls to zero. If the inductor current falls to zero, the inductor is completely discharged before the end of the switching period and the operating equations of the converters will change. This is called discontinuous conduction mode (DCM) and by choosing a large enough inductor, the discontinuous conduction mode can be avoided.

C.2.1 Boost converter

The boost converter is designed to step up a DC-voltage and its topology is shown in figure and has two states of operation depending on the state of the switching device.
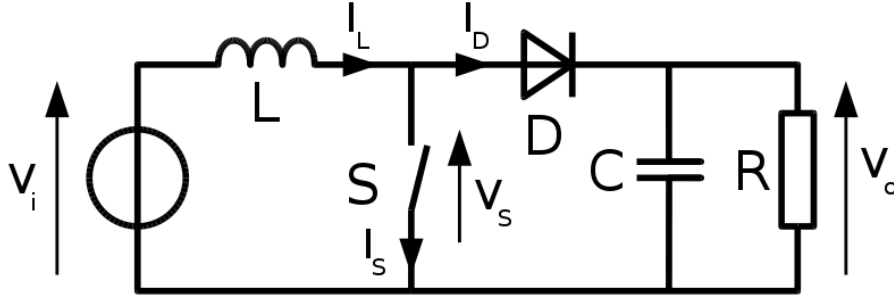
Figure C.4: DC-DC boost converter circuit [34]

Switch closed: When the switch is closed during the on-time of the switch, t_{on}, the voltage across the inductor is given by $V_L = V_i$. By using equation (C.10), the inductor current increases with the derivative given by:

$$\frac{di_L}{dt} = \frac{V_i}{L} \tag{C.12}$$

The total current increase during t_{on}:

$$\Delta i_L = \frac{V_i}{L}t_{on} = \frac{V_i}{L}DT_s \tag{C.13}$$

During this same interval, the diode is inversely biased, and the capacitor supplies current to the load.

Switch open: Upon opening the switch during the time t_{off}, the voltage across the inductor is $V_i - V_o$. The derivative of the inductor current is:

$$\frac{di_L}{dt} = \frac{V_i - V_o}{L} \tag{C.14}$$

The total current increase during t_{off}:

$$\Delta i_L = \frac{V_i - V_o}{L}t_{off} = \frac{V_i - V_o}{L}(1 - D)T_s \tag{C.15}$$

Since this is a step up converter $V_o > V_i$ the derivative of the current is negative during the off-time of the switch and the current decreases. This is natural since the inductor being charged during the on-time, must release the same amount of energy during the off-time. This creates the boosting effect in the circuit. The increase in inductor current during the switch closure time must equal the decrease during open switch time. We get:

$$\frac{V_i}{L}DT_s = \frac{V_i - V_o}{L}(1 - D)T_s \tag{C.16}$$

By rearranging, the relation between the voltage input and output can be obtained:

$$V_o = \frac{V_i}{1 - D} \tag{C.17}$$

C.2.2   Buck converter

The buck converter is designed to step down a DC-voltage and its topology is shown in figure and has two states of operation depending on the state of the switch.
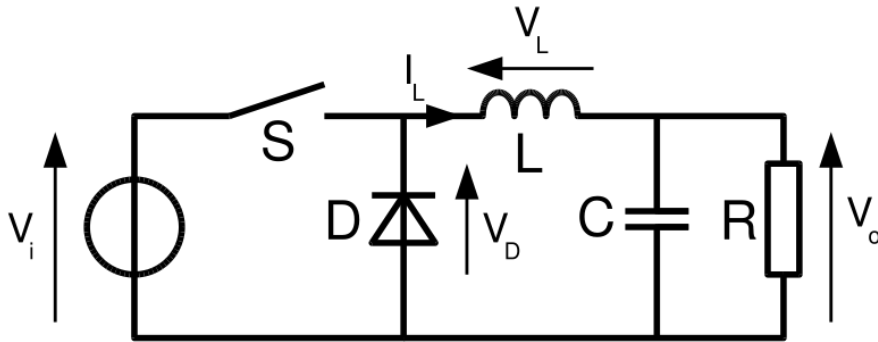
Figure C.5: DC-DC buck converter circuit [34]

Switch closed: With the switch closed, the input voltage is directly connected to the load through the inductor. In this case the voltage across the inductor is $V_L = V_i - V_o$, the inductor current increases linearly and energy is stored in the inductor. The change in current can be calculated from C.10 to be:

$$\Delta i_L = \frac{V_i - V_o}{L} t_{on} \tag{C.18}$$

Switch open: When the switch is open, the input voltage is disconnected from the circuit and the voltage across the inductor is $V_L = -V_o$. The inductor opposes a change in current and forces a decreasing current through the circuit through the diode which now is forward biased. Again, the change in the inductor current can be derived:

$$\Delta i_L = \frac{-V_o}{L} t_{off} \tag{C.19}$$

Similarly as for the boost converter, we can write:

$$\frac{V_i - V_o}{L} t_{on} - \frac{V_o}{L} t_{off} = 0 \tag{C.20}$$

Finally, by rearranging, we get:

$$D = \frac{V_o}{V_i} \tag{C.21}$$

Appendix D

Clark and Park transformation

A Clark transformation followed by a Park transformation is what is commonly known as a dq0-transformation, or direct-quadrature-zero transformation is a mathematical transformation to simplify the analysis of three-phase circuits. For a balanced three-phase circuit, the *dq*-transform reduces a three-phase sinusoidal waves into two constant DC signals. (zero-axis component is 0)

The transformation is often used to facilitate the modelling and control of three phase electrical machines and three phase inverters. The Clark Transformation is a projection of the three phase quantities (abc) onto two stationary axes ($\alpha\beta$). The transformation is given as below:

$$\begin{bmatrix} X_\alpha \\ X_\beta \end{bmatrix} = k \begin{bmatrix} 1 & \frac{-1}{2} & \frac{-1}{2} \\ 0 & \frac{\sqrt{3}}{2} & -\frac{\sqrt{3}}{2} \end{bmatrix} \begin{bmatrix} X_a \\ X_b \\ X_c \end{bmatrix} \tag{D.1}$$

This gives:

$$X_\alpha = k(X_a + \frac{-1}{2}X_b + \frac{-1}{2}X_c) \tag{D.2}$$

$$X_\beta = k(\frac{\sqrt{3}}{2}X_b + \frac{-\sqrt{3}}{2}X_c) \tag{D.3}$$

Where X represents arbitrary three-phase quantities (voltages, currents,...), and k is a constant.

The Park transformation is defined as the transformation from the $\alpha\beta$ stationary frame to the *dq* rotating frame:

$$\begin{bmatrix} X_d \\ X_q \end{bmatrix} = \begin{bmatrix} cos(\theta) & sin(\theta) \\ -sin(\theta) & cos(\theta) \end{bmatrix} \begin{bmatrix} X_\alpha \\ X_\beta \end{bmatrix} \tag{D.4}$$

Which gives:

$$X_d = X_\alpha cos(\theta) + X_\beta sin(\theta) \tag{D.5}$$

$$X_q = -X_\alpha sin(\theta) + X_\beta cos(\theta) \tag{D.6}$$

The complete transformation from *abc*-quantities to *dq*-quantities is given by:

$$\begin{bmatrix} X_d \\ X_q \end{bmatrix} = k \begin{bmatrix} cos(\omega t) & cos(\omega t - \frac{2}{3}\pi) & cos(\omega t + \frac{2}{3}\pi) \\ -sin(\omega t) & -sin(\omega t - \frac{2}{3}\pi) & -sin(\omega t + \frac{2}{3}\pi) \end{bmatrix} \begin{bmatrix} X_a \\ X_b \\ X_c \end{bmatrix} \tag{D.7}$$

Hence:

$$X_d = k(X_a cos(\omega t) + X_b cos(\omega t - \frac{2}{3}\pi) + X_c cos(\omega t + \frac{2}{3}\pi)) \tag{D.8}$$

$$X_q = k(-X_a sin(\omega t) - X_b sin(\omega t - \frac{2}{3}\pi) - X_c sin(\omega t + \frac{2}{3}\pi)) \tag{D.9}$$

If we consider balanced three-phase voltages:

$$V_a = V cos(\omega t) \tag{D.10}$$

$$V_b = V cos(\omega t - \frac{2}{3}\pi) \tag{D.11}$$

$$V_c = V cos(\omega t + \frac{2}{3}\pi) \tag{D.12}$$

By setting k to 2/3 we get:

$$V_d = V \tag{D.13}$$

$$V_q = 0 \tag{D.14}$$

This is called the voltage invariant transform and the magnitude of d-axis voltage is kept constant equal to V. By setting $k = \sqrt{\frac{2}{3}}$ the power-invariant transform is obtained and means that the dq-power is the same as the abc-power. The voltage-invariant transform will be used in this thesis.

71

Appendix E

Per Unit System

The three phase base quantities are defined as followed:

$$V_b = \sqrt{\frac{2}{3}} V_{LL,rms} \tag{E.1}$$

Where V_b is the nominal peak phase voltage at the PCC and $V_{LL,rms}$ is the line-to-line RMS voltage at the PCC.

$$S_b = 3 \frac{V_b}{\sqrt{2}} \frac{I_b}{\sqrt{2}} \tag{E.2}$$

Where S_b is the nominal three-phase apparent power at the PCC and I_b is the nominal peak phase current at the PCC.

Hence:

$$I_b = \frac{2S_b}{3V_b} \tag{E.3}$$

The base impedance is given as:

$$Z_b = \frac{V_b}{I_b} \tag{E.4}$$

From the base impedance, the base inductance can be found:

$$L_b = \frac{Z_b}{\omega_b} \tag{E.5}$$

Where L_b is the per phase base inductance and ω_b is the base frequency. Further the base capacitance is given as:

$$C_b = \frac{1}{\omega_b Z_b} \tag{E.6}$$

Where $C_{pu} = \frac{1}{\omega_b Z_b C}$.

To calculate the base quantities at the DC-link, we assume no losses in the system

and make use of the power balance:

$$S_b = \frac{3}{2} V_b I_b = S_{DC} = V_{DC,b} I_{DC,b} \tag{E.7}$$

Where $V_{DC,b}$ and $I_{DC,b}$ are the base quantities at the DC-link. The base for the DC-voltage is chosen to be:

$$V_{DC,b} = 2V_b \tag{E.8}$$

Hence, the base for the DC-current is determined:

$$I_{DC,b} = \frac{3}{4} I_b \tag{E.9}$$

And the base for the DC-link impedance:

$$Z_{DC,b} = \frac{V_{DC,b}}{I_{DC,b}} = \frac{8}{3} \frac{V_b}{I_b} = \frac{8}{3} Z_b \tag{E.10}$$

Hence, the base for the DC-capacitance is:

$$C_{DC,b} = \frac{1}{\omega_b Z_{DC,b}} \tag{E.11}$$

And the DC-inductance:

$$L_{DC,b} = \frac{Z_{DC,b}}{\omega_b} \tag{E.12}$$

Appendix F

Technoport RERC 2012 Conference Proceedings

ELSEVIER

Technoport RERC Research 2012

Analysis of the Power Extraction Capability for the Wave Energy Converter *BOLT*®

Johannes Bedos Ulvin (johannul@stud.ntnu.no), Marta Molinas (marta.molinas@ntnu.no), Jonas Sjolte (jonas.sjolte@ntnu.no)

Department of Electrical Power Engineering,
Norwegian University of Science and Technology,
O.S. Bragstad plass 2E, Trondheim, Norway

Abstract

The goal of this paper is to investigate the power extraction capability for the *Wave Energy Converter* (WEC) concept *BOLT*®. Specifically, the impact of different *control strategies* on the power extraction and their high sensitivity to the incoming waves will be presented. The *BOLT*® concept is based on a flat point absorber designed with a small mass and a *Power Take-Off* (PTO) solely controlling the amplitude of the WEC's motion, *passive loading*. It is reported that the small weight of the device makes passive loading suitable for most sea states. As the device is still on the pilot stage, there is room for exploring the potential improvement of the power extraction for different sea states by determining the optimal control strategy for sinusoidal waves of different amplitudes and frequencies. In addition, when considering realistic designs of PTOs, the constraint on the peak power should be taken into account. The power handled by the electro-mechanical system is limited by the ratings of the electrical components and the mechanical force limits. Imposing a constraint on the peak power will greatly affect the control strategies' impact and thus the average extracted power.

Keywords: Wave Energy Converter, control strategies, Power Take Off, passive loading.

1. Introduction

Despite having the potential of satisfying a significant fraction of the world's energy needs [1], wave energy has been overshadowed by more mature and profitable renewable technologies like wind and solar.

There are many prototypes with very different concepts being investigated around the world and it is very hard to predict which of the technologies holds the most promise [2]. The *BOLT*® Wave Energy Converter [3], depicted in figure 1, is developed by Fred Olsen Renewables [4]. *BOLT*® is a circular, flat, semi-submerged point absorber and is located near Risør, Norway. Currently, Fred Olsen Renewables are working on a second version which is to be installed at the Wave Hub [5], near Hayle in the United Kingdom.
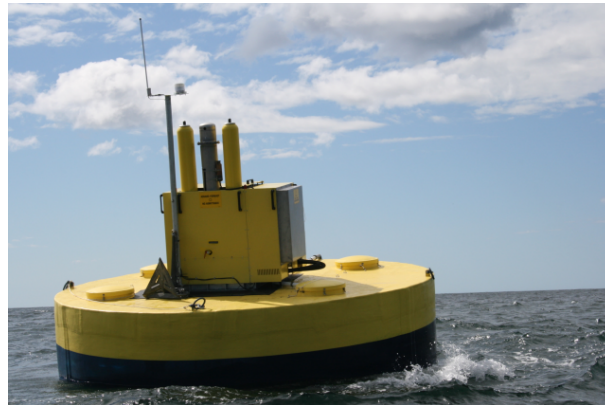
Fig. 1: Fred Olsen's Wave Energy Converter BOLT®, located outside Risør, Norway

To maximize the extractable power, the Power Take Off (PTO) of the device needs to be tuned according to the incoming sea waves. For sinusoidal waves, the theoretical maximum is obtained by controlling the phase and the amplitude of the WEC's motion to be in resonance with the incident wave. However, such control, usually referred to as optimal control, requires costly oversizings of the system's mechanical structure and electrical ratings.

While designing $BOLT^{®}$ and as the result of a techno-economical optimization, Fred Olsen decided to apply a simpler control strategy which is more likely to respect the electro-mechanical limitations, only resorting to control the amplitude of the WEC's motion. This is done by only controlling the damping of the device, commonly called passive loading. To make the WEC more suitable for this control strategy, $BOLT^{®}$ has a low mass to ensure a saturation on force and power already in low sea states.

The purpose of this paper is to investigate the improvement of the power extraction by including a phase control for these low sea states. With a limitation on the maximum extractable power, passive loading can be beneficial during high amplitude waves whereas optimal control has the ability to extract more power during calmer seas [6], [7].

For this investigation, the WEC and PTO system is modelled as an electrical equivalent. An estimation of the wave excitation force is used as voltage source and the point absorber is modelled as an RLC circuit. The PTO consists of a power extracting element (resistance) and a reactive element (inductance). By performing an electrical analysis of the circuit, the control problem is optimally solved by using an iterative numerical method in MATLAB.

Finally the electrical circuit is simulated in Simulink using the proposed control method.

2. Device Presentation

The device under investigation in this study is the $BOLT^{®}$ Wave Energy Converter developed by Fred Olsen and is a prototype that has been tested and used in operation outside Risør in Norway since June 2009. The idea was to make a simple, light and cost-effective device.

The point absorber is semi-submerged and shaped as a cylinder tightly moored to the sea bottom. The dimensions of the point absorber can be found in table 1.

The Power Take-Off system is a hybrid PTO, which means that it's a combination of a mechanical/electrical and a hydraulic PTO. The hydraulic system works as some kind of energy storage but will not be further mentioned in this study.

The PTO system uses the mooring rope as production rope. The rope is tied around a winch, which transforms the linear motion from the motion of the point absorber into a rotational motion. The angular velocity is increased through a gear system consisting of belts. The gear system is in place so that an induction machine can be connected.
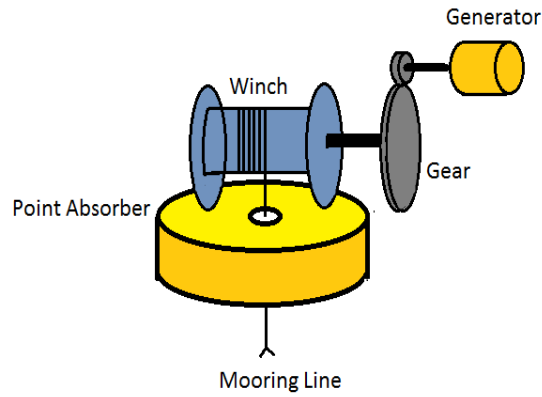
Fig. 2: Principal sketch of the WEC

Table 1. Point absorber dimensions

Diameter	5,15m
Height	1,5m
Mass	5000kg

$BOLT^®$ has not been connected to the grid. However the goal for the next generation $BOLT^®$ device, $BOLT2^®$, is to build a commercial system in operation at the wave test facility Wave Hub in the UK. It is planned to use a permanent magnet synchronous machine (PMSM) and a suitable back-to-back converter. With this topology the gear system can be made redundant. The reduction in rotational speed can be compensated by a high number of poles in the PMSM. The frequency converter ensures that the frequency at the point of common coupling with the grid is constant.

3. Modelling of a point absorber in heave

3.1. Hydrodynamic diffraction model

The hydrodynamic diffraction model is a well known representation of a point absorber in heave. Some basic assumptions are required to make use of this model. The movement of the device is restricted to one degree of freedom (heave) and the waves are propagating in an infinite water depth with small motion. The following equation is then valid:

$$(M + a(\omega))\frac{d^2x(t)}{dt^2} + B(\omega)\frac{dx(t)}{dt} + Kx(t) = F_E(t) - F_L(t) \tag{1}$$

$F_E(t)$, the excitation force, is the force applied by the wave on the device. The point absorber is characterized by its mass, M, its frequency dependent damping, $B(\omega)$ and its stiffness, K. In addition, the coefficient $a(\omega)$ represents the added mass from the body of water that takes part in the buoy motion. $F_L(t)$, the Power Take Off force, is the force applied from the device to the shaft of a generator through a gear system. The

solution to this second-order linear ordinary differential equation gives the position of the WEC with respect to time, $x(t)$.

3.1.1. Parameter identification

In order to perform the analysis of the power extraction capability of $BOLT^{®}$, the parameters of (1) need to be determined. $BOLT^{®}$ is cylindrical with a radius $r = 5, 15m$ and a mass $M = 5000kg$. From the radius and the geometry of the device, the stiffness can be derived:

$$K = \pi r^2 \rho g = \pi(\frac{5.15m}{2})^2 \cdot 1027 \frac{kg}{m^3} \cdot 9.81 \frac{m}{s^2} \simeq 209 \frac{kN}{m} \tag{2}$$

In addition, Fred Olsen provided frequency-dependent vectors of 27 points for the added mass, $a(\omega)$, the damping, $B(\omega)$ and the excitation force coefficient, $\widehat{H}_{F\zeta}(\omega)$.

3.1.2. Estimation of the excitation force

The excitation force is dependent of the incoming wave, the geometry and the design of the WEC. An approximation of the excitation force [8] is given by the excitation force coefficient and the incident wave elevation, ζ:

$$\widehat{F_E} = \widehat{H}_{F\zeta}(\omega)\zeta \tag{3}$$

The incident wave elevation will be referred to as the amplitude of an incoming sinusoidal wave, A. The excitation will be modelled as a sinusoidal excitation force. The rms-value will be used for the calculations in this paper by the following formula:

$$F_E(\omega) = \frac{\widehat{H}_{F\zeta}(\omega)A}{\sqrt{2}} \tag{4}$$

3.2. Electrical Analogue

The hydrodynamic diffraction model given by (1), is essentially a spring-mass system. It is known that an electrical RLC-circuit can be written on the exact same form as the spring-mass system:

$$L\frac{d^2Q(t)}{dt^2} + R\frac{dQ(t)}{dt} + \frac{1}{C}Q(t) = E(t) - V_L(t) \tag{5}$$

In an electrical circuit, the current $I(t)$ is of more importance than the charge $Q(t)$. Thus, using $I(t) = \frac{dQ(t)}{dt}$ and $\frac{dI(t)}{dt} = \frac{d^2Q(t)}{dt^2}$, and inserting into (5):

$$L\frac{d^2I(t)}{dt^2} + R\frac{dI(t)}{dt} + \frac{1}{C}I(t) = \frac{d}{dt}(E(t) - V_L(t)) \tag{6}$$

The solution $I(t)$ is composed of a transient and a steady-state solution. Theoretically, the transient solution dies out because of the damping as $t \to \infty$, but in practice it will become negligible after a relatively short time. Since we are assuming a sinusoidal input (excitation force) the steady-state response of the current will be sinusoidal with the same frequency as the input including a phase shift. When steady-state is assumed, an analysis in the frequency domain can be performed.

The electrical circuit described by (6) is depicted in figure 3 and a summary of the mechanical quantities and their respective electrical quantities are summarized in table 2. It is desirable to develop the electrical equivalent to be able to analyse the power extraction with knowledge from electric circuits theory.

4. Control

4.1. Control Strategies

The aim is to maximize the power supply to the PTO. By manipulating the PTO damping and the PTO added mass, the power extracted by the PTO can be controlled.
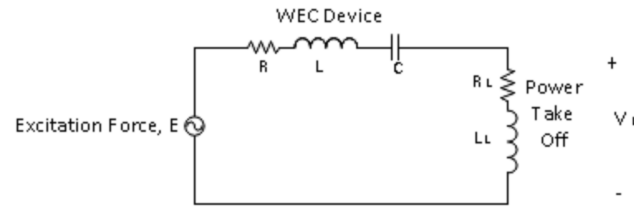
Fig. 3: Electrical equivalent circuit of the hydrodynamical system

Table 2. Relations between the hydrodynamical and electrical model

Mechanical system	Electrical system
Excitation force, F_E	Voltage source, E
Position, x	Charge, Q
Speed, v	Current, I
Total mass, $M + a(\omega)$	Inductance, L
Damping, $B(\omega)$	Resistance, R
Stiffness, K	Inverse capacitance, C^{-1}
PTO force, F_L	Load voltage, V_L
PTO damping, B_L	Load resistance, R_L
PTO added mass, M_L	Load reactance, L_L

4.1.1. Optimal Control

The reactive component of the PTO is set as to exactly compensate the reactive components of the physical device. The device will then be in resonance with the incoming wave and the excitation force will be in phase with the speed of the WEC. When the total reactive term is equal to zero, the PTO damping should be tuned to the same value as the device damping to achieve maximum power transfer. Hence, the tuning of the control parameters are given as follows:

$$R_L = R \tag{7}$$

$$X_L = -(wL - \frac{1}{wC}) \tag{8}$$

For this type of control, a bi-directional flow of power is required. Since this is an all-electric PTO, the generator will have to switch between motor and generator operation. Also, the power electronic converter will require bi-directional switches.

4.1.2. Passive Loading

A simpler way of controlling the power extraction is by only having a resistive control of the PTO. The optimal power transfer is then given by:

$$R_L = \sqrt{R^2 + (wL - \frac{1}{wC})^2} \tag{9}$$

In this case, the power flows in one direction since the PTO power factor is unity; i.e. the PTO force is in phase with the WEC speed. This is the type of control that is currently applied to BOLT.

4.1.3. Control Constraints

Without any limitations to the system, optimal control would always maximize the average power output. However, wave energy is troubled by extremely high instantaneous peaks of power compared to the average extractable power. High peaks in power requires a huge and costly over-dimensioning of the electro-mechanical system and reduces the power quality supplied to the grid.

For sinusoidal conditions the peak-to-average ratio, k, can be described by the following equation [9]:

$$k = 1 + \frac{1}{cos(\phi_L)} \tag{10}$$

Where the PTO power factor, $cos(\phi_L)$, is given by:

$$cos(\phi_L) = cos(arctan(\frac{X_L}{R_L})) \tag{11}$$

For passive loading, $X_L = 0$ and the power factor will be equal to 1 (unity). k will then always be equal to 2, regardless of the magnitude of R_L. Passive loading gives the lowest possible value for k.

Evidently, the increase of the reactive load element, while keeping R_L constant, increases the displacement angle $cos(\phi_L)$ and $\frac{1}{\phi_L}$ can quickly become a large number and hence the peak-to-average ratio $k > 2$.

Optimal control requires the largest reactive element to compensate for the reactive elements of the device. The average power extraction can be increased by increasing the reactive power compensation, at the expense of a increasing peak-to-average ratio k.

4.2. Development of a Constrained Optimization Problem

As mentioned, for an unconstrained problem optimal control will always give the optimal solution. Nevertheless, previous arguments have shown that a trade-off needs to be met between two conflicting aims: maximizing the average power while minimizing investment costs.

For $BOLT^{\circledR}$ the problem will be solved with a constraint on the peak power. After being advised by Fred Olsen, the rating of the electrical equipment of $BOLT^{\circledR}$ has been set to $P_{max} = 130kW$

When constraining the problem, the most beneficial control strategy and the optimal tuning of the PTO, will change according to the incident wave. It is vital to understand that for each incoming wave of different amplitude or frequency, the electrical circuit will be different and the optimal solution of the circuit will change.

Another important realization is that the optimal solution, might lie in between optimal control and passive loading. For waves where the peak power constraint never is reached, optimal control should be applied. With higher energy waves, the constraint might be reached and hence the peak-to-average power ratio has to be reduced by decreasing the reactive loading. An **intermediate** solution is obtained. Very high energy waves could require to reduce k until passive loading is achieved. To cope with even higher energy waves, and no longer being able to adjust k, the peak power can still be kept at the allowed limit by increasing the resistive element of the PTO, at the expense of a reduced average power.

The borderlines between the three control strategies are calculated and a map of the advisable control strategies is illustrated in figure 4. The relevant frequency range has been based on a scatter diagram for the Wave Hub site [10] given in table 3.

Figure 4 suggests that for wave amplitudes below 1.4 m, more power can always be extracted by $BOLT^{\circledR}$ if some kind of reactive control is included in the control of the PTO. By consulting the scatter diagram for the Wave Hub, $BOLT^{\circledR}$ should be operated with some kind of reactive control for at least 4398 hours yearly according to the map.

For the unconstrained case of optimal control, the tuning of the elements are easily calculated, however in the passive loading and the intermediate control area, a mathematical optimization problem needs to be solved. The goal is to maximize the average power extraction by the PTO. A general expression for the average power extracted by the PTO is given by multiplying the square of the current magnitude in the circuit by the resistive PTO element as follows:
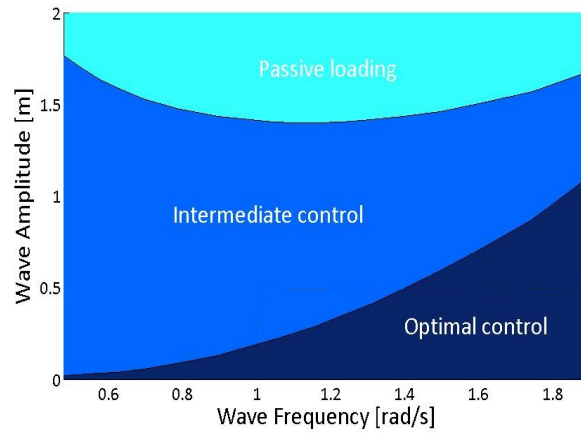
Fig. 4: Map of the optimal control strategies

Table 3. Scatter diagram at Wave Hub, hours per wave state

Significant wave height [m]	Wave period Tz [sec]								
	3,5	4,5	5,5	6,5	7,5	8,5	9,5	10,5	11,5
0,25	26	79	44	18	0	0	0	0	0
0,75	499	832	491	140	18	0	0	0	0
1,25	184	1051	604	307	70	26	9	0	0
1,75	0	587	701	333	149	53	26	0	9
2,25	0	96	534	254	123	44	9	0	0
2,75	0	0	237	228	105	26	9	9	0
3,25	0	0	26	175	123	44	9	0	0
3,75	0	0	0	79	96	35	18	0	0
4,25	0	0	0	9	44	26	9	9	0
4,75	0	0	0	0	26	18	9	0	0
5,25	0	0	0	0	18	26	18	0	0
5,75	0	0	0	0	0	18	9	0	0
6,25	0	0	0	0	0	9	0	0	0

$$\overline{P} = \frac{E^2 R_L}{(R + R_L)^2 + (wL - \frac{1}{wC} \pm R_L tan(\phi_L))^2} \tag{12}$$

To remove an unknown X_L, has been replaced by $\pm R_L tan(\phi_L)$; where the $\pm$ sign depends on the resulting reactance of the WEC device. Since the capacitive element of the WEC is dominant, the sign should be positive.

The optimization problem can be expressed:

$$max \ \overline{P} \tag{13}$$

$$while \ \widehat{P} = \overline{P}(1 + \frac{1}{cos(\phi_L)}) < 130kW \tag{14}$$

This problem can be solved analytically with Lagrange multipliers. However, they give very complex equations; hence, a simpler iterative numerical approach is chosen [6]. By implementation in MATLAB,
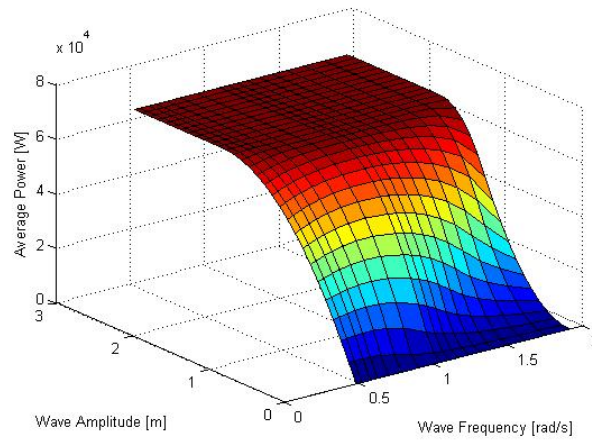
Fig. 5: Surface plot of the average power extraction with the proposed control method for different wave amplitudes and frequencies

the problem could be solved for a similar selection of wave amplitudes and wave frequencies as for figure 4. The average power extraction is plotted in figure 5.

The plot shows the average power according to the incident wave which is characterized by its frequency and amplitude. The average power increases with the amplitude of the wave until it enters the passive loading area where the average power is constant irrespective of wave frequency or amplitude. The extra energy from higher energy waves is oppressed by a higher PTO damping.

To make a comparison of the power extraction with the purely passive control method applied by $BOLT^{®}$ and the proposed control method, a 2D-plot of the average power extraction for both methods is given in figure 6. A single frequency is chosen on the basis of the scatter diagram for the Wave Hub. By calculating the average of the most frequent wave frequencies during a year at the Wave Hub location, an average frequency of 1.13 $\frac{rad}{s}$ is obtained. Hence, from the data points provided by Fred Olsen a frequency
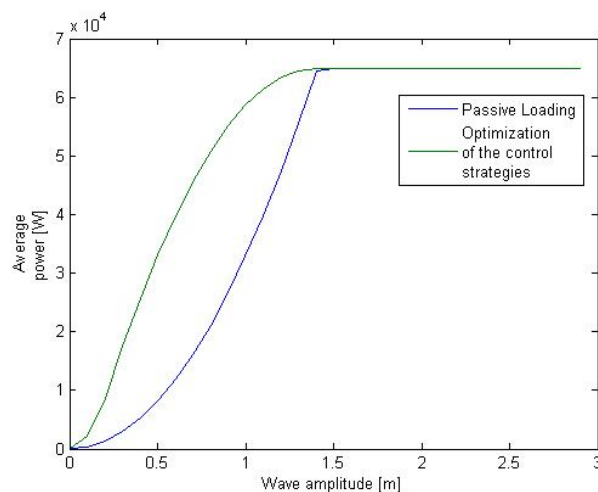

Fig. 6: Comparison of the performance of the two control methods

of 1.1021 is chosen.

Figure 6 clearly confirms that more power is extracted for low amplitude waves with the optimized control method.

4.3. Energy Calculations

With the use of the number of hours a wave state occurs during a year given by table 3, the expected yearly energy output from the WEC can be calculated. Since the wave periods given in table 3 do not exactly correspond to the 27 wave periods provided by Fred Olsen, the closest ones are chosen. The device PTO is optimally tuned according to the wave states and the average extracted power is calculated. By multiplying with the number of hours a given wave state occur per year, the total extracted energy can be determined.

Table 4. Expected yearly energy output with an optimization of the control strategies, MWH per wave state

Significant wave height [m]	Wave period [sec]								
	3,5	4,5	5,5	6,5	7,5	8,5	9,5	10,5	11,5
0,25	0,08	0,45	0,44	0,24	0	0	0	0	0
0,75	13,35	35,34	23,22	6,76	0,87	0	0	0	0
1,25	10,85	66,59	38,69	19,69	4,44	1,65	0,56	0	0
1,75	0	38,16	45,57	21,65	9,69	3,45	1,69	0	0,59
2,25	0	6,24	34,17	16,51	8,00	2,86	0,59	0	0
2,75	0	0	15,41	14,82	6,83	1,69	0,59	0,59	0
3,25	0	0	1,69	11,38	8,00	2,86	0,59	0	0
3,75	0	0	0	5,14	6,24	2,28	1,17	0	0
4,25	0	0	0	0,59	2,86	1,69	0,59	0,59	0
4,75	0	0	0	0	1,69	1,17	0,59	0	0
5,25	0	0	0	0	1,17	1,69	1,17	0	0
5,75	0	0	0	0	0	1,17	0,59	0	0
6,25	0	0	0	0	0	0,59	0	0	0

Table 5. Expected yearly energy output with passive loading, MWH per wave state

Significant wave height [m]	Wave period [sec]								
	3,5	4,5	5,5	6,5	7,5	8,5	9,5	10,5	11,5
0,25	0,04	0,16	0,09	0,04	0	0	0	0	0
0,75	7,42	14,78	9,15	2,59	0,30	0	0	0	0
1,25	7,60	51,85	31,25	15,79	3,25	1,21	0,40	0	0
1,75	0	38,16	45,57	21,65	9,69	3,45	1,69	0	0,59
2,25	0	6,24	34,17	16,51	8,00	2,86	0,59	0	0
2,75	0	0	15,41	14,82	6,83	1,69	0,59	0,59	0
3,25	0	0	1,69	11,38	8,00	2,86	0,59	0	0
3,75	0	0	0	5,14	6,24	2,28	1,17	0	0
4,25	0	0	0	0,59	2,86	1,69	0,59	0,59	0
4,75	0	0	0	0	1,69	1,17	0,59	0	0
5,25	0	0	0	0	1,17	1,69	1,17	0	0
5,75	0	0	0	0	0	1,17	0,59	0	0
6,25	0	0	0	0	0	0,59	0	0	0

The amount of energy extracted over a year with only passive loading as control strategy is also calculated. The results are given in table 4 and 5.

With the proposed optimization method, the total amount of energy that can be produced during a year is $507, 63 \frac{MWh}{year}$. By only using passive loading as control strategy the expected amount of energy is calculated to be $430, 35 \frac{MWh}{year}$. This represents an energy increase of $77, 28 \frac{MWh}{year}$ or $17, 96\%$. Assuming that the cost of the electricity produced is similar to Wavestar [12], which has been announced to be around $1 \frac{€}{kWh}$ [2], the increase in income by applying the optimized control method would be $77280 \frac{€}{year}$. This is without considering any extra investment costs from implementing more advanced control.

4.4. Mechanical Considerations

A weakness in the map from figure 4 was pointed out by Fred Olsen. Before entering the electrical domain, i.e. before the generator windings, the power is composed by two components, speed/angular speed and force/torque. The speed is often below the allowed limit for all WEC components [11]. Therefore the PTO force is the main design property and a constraint on force should be included, which translates as a limit on the voltage over the PTO in the electrical equivalent. The resulting map is depicted in figure 7.

With the force constraint included, both the intermediate control area and the optimal control area are significantly reduced. These reductions favours the application of a purely passive control strategy. However, the scatter diagram shows that even with this reduction, the WEC should still operate with intermediate or optimal control for at least 666 hours yearly. 666 hours is found by adding the hours from the scatter diagram for a wave height of 0.25 m and adding the hours for a wave height of 0.75m and a period of 3.5 seconds, which clearly are in a reactive control area. The question is if the extra amount of power extracted for these low energy waves is enough to justify the extra investment from more advanced control.

5. Simulations

Time simulations were made in MATLAB/Simulink. In order to show the response from operating in the three different control areas, three different excitation forces were generated. On an interval of 200s each, excitation forces were generated with wave amplitudes of 0.1m, 0.6m, 1.4m. To simplify the simulations, a constant frequency was chosen. The incoming wave frequency was set to 1.1 $\frac{rad}{s}$, as previously. This gives constant values for the RLC-branch describing the device. With the selected frequency L = 42376 *H*, R = 14159 Ω and C = $\frac{1}{209000}$ = 4.7847e-6 *F*. It can be worth noting that the device inductance L is dominated by the value of the added mass as the device itself only weighs 5 tons.
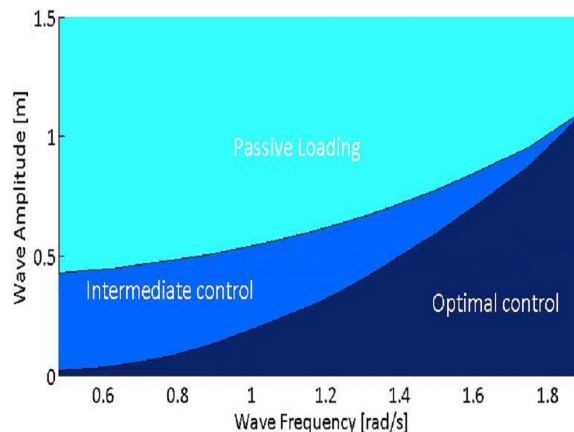

Fig. 7: Map of the optimal control strategies with constraints on force and power

Table 6. Simulation results

	Optmization of Control Strategies			Passive Loading	
Wave Amplitude	Peak Power	Average Power		Peak Power	Average Power
0.1*m*	20560*W*	1850*W*		662*W*	331*W*
0.6*m*	130000*W*	38620*W*		23844*W*	11922*W*
1.4*m*	130000*W*	65000*W*		129820*W*	64910*W*

When A = 0.1m, according to optimal control, the control parameters should be set to $R_L = 14160\Omega$ and $L_L = 128510H$. This gives a peak power of 20560*W* and an average power of 1850*W*. For A = 0.6m the control strategy is tuned to an intermediate control, $R_L = 66040\Omega$ and $L_L = 128510H$. As previously explained, the peak power limit is then reached and the average extracted power is 38620*W*. At A = 1.4m the control is just about to enter the purely passive domain. The control settings are given by $R_L = 144470\Omega$
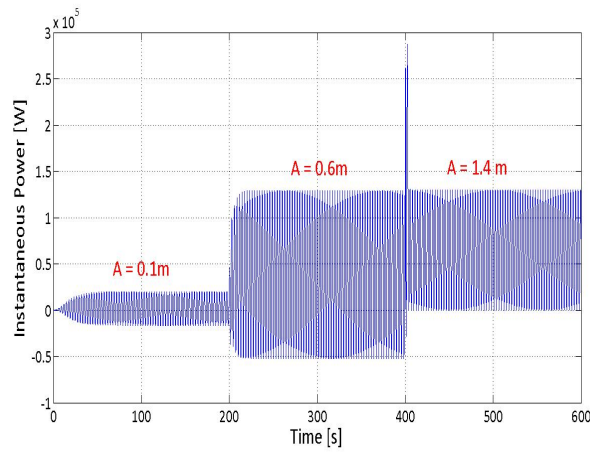

Fig. 8: Instantaneous power for step changes in wave amplitudes with optimal control strategies
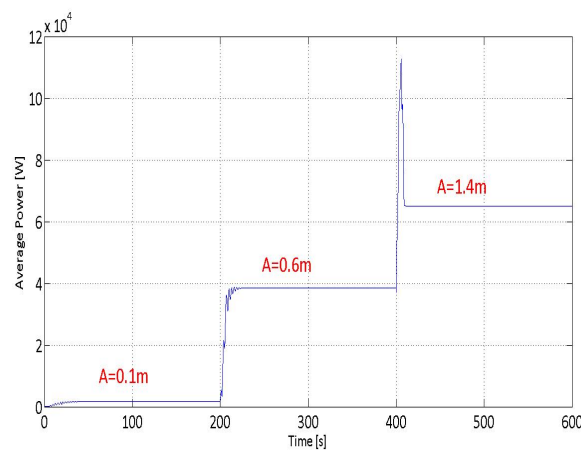

Fig. 9: Average power for step changes in wave amplitudes with optimal control strategies

and $L_L = 200H$. Obviously, the peak and average power is then $130000W$ and $65000W$. These results can be confirmed and viewed in figure 8 and 9 and are summarized in table 6. Figure 8, which shows the instantaneous, power clearly shows that with reactive control, the power flow has to be bi-directional. The unexpected transient peaks are due to switching in the Simulink circuit.

To get an impression of the improved power extraction capability when including reactive control in the control strategy, the same simulations are done for a purely passive control strategy. For simplicity, the frequency is still kept constant throughout the simulation. The tuning of the resistive element is then also constant throughout the analysis: $R_L = 143630\Omega$. The results are given in the table 6 and plots in figure 10 and 11.

From this analysis, at A = 0.1m, the average power can be improved by a factor of 5.6. For A = 0.6m the average power can be improved by a factor of 3.24.

Another observation is that the instantaneous power passes zero twice for every wave when applying a reactive control, and that it touches zero for every wave when applying a purely passive loading. Therefore an important feature of wave energy projects is a flexible energy storage to deal with the fluctuating power output and improve the power quality at the grid connection point.
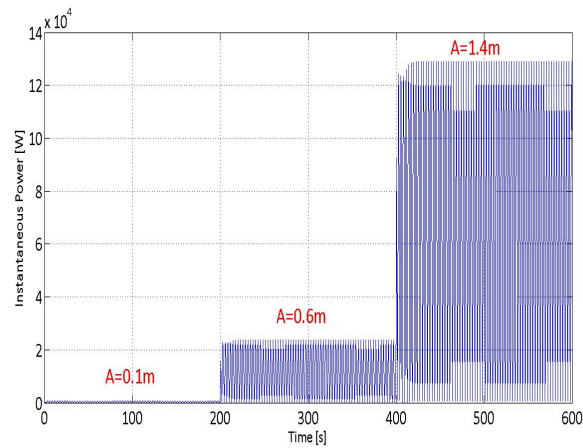

Fig. 10: Instantaneous power for step changes in wave amplitudes with purely passive loading
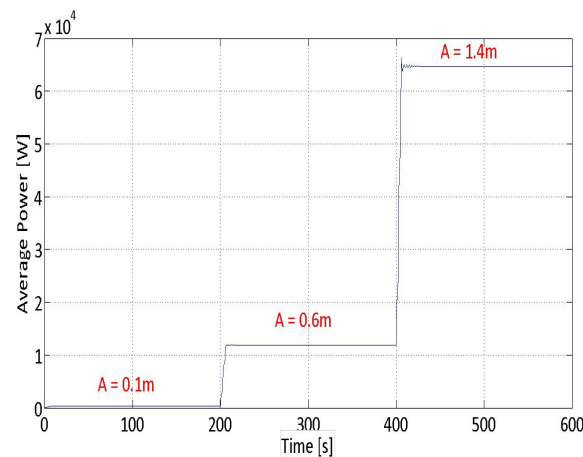

Fig. 11: Instantaneous power for step changes in wave amplitudes with purely passive loading

6. Discussion on WEC design

This study has shown how it is possible to optimize the power extraction of the $BOLT^{\circledR}$ WEC with an effective tuning of the control parameters. However, the design of $BOLT^{\circledR}$ is not optimized with respect to power production and the potential for improving the power extraction would be higher if $BOLT^{\circledR}$ had a different design. WEC designers should therefore include control considerations already from the first stages of the product development and design.

6.1. Effect of a low mass on WEC design:

$BOLT^{\circledR}$ was designed with a low mass. The effect of this can be viewed by inspecting the electrical equivalent in figure 3. The WEC device has two reactive terms describing it, the inductance L and the capacitance C. Since L is small because of the low mass of the WEC, the capacitance C would be more dominant than for WECs with larger masses: $BOLT^{\circledR}$ is a stiff system. The stiffer the system, a larger reactive element is needed in the PTO to compensate.

From this reasoning, a light stiff system would be less susceptible to reactive control than a heavier and less stiff system. Building systems that can easily achieve resonance should therefore be a priority for WEC designers.

6.2. Effect of the force constraint on WEC design:

By introducing the force constraint into the problem the power extraction is effectively reduced. By building a more robust PTO, the force constraint would loosen or even become redundant. The power extraction capability would then move from the map in figure 7 to figure 4.

Greater attention should therefore be paid to increasing the robustness of the PTO. Possible solutions would be to use the strongest production rope available, using two ropes and/or two winches to divide the tension, losing the gear system,...

7. Conclusion and further work

This paper explains how an effective tuning of the control parameters can maximize the average power extraction for the Wave Energy Converter $BOLT^{\circledR}$, under sinusoidal conditions. The method utilized took into account a constraint in the peak power to avoid breaching the electrical limits of the system. It is shown how a more elaborate tuning of the all-electric PTO will increase the average power extraction for low amplitude waves. Section 4.3 concludes with a possible energy increase of $77,28 \frac{MWh}{year}$ or $17,96\%$ when applying the proposed control method.

However, if an additional constraint on force is included, the benefit from applying the proposed control strategy is significantly reduced. This double constrained maximization problem was not optimally solved and further work should be done to quantify the possible energy improvement.

The next step should be the development of a hydrodynamical model in time domain based on irregular waves which are more closely related to real sea waves. It is known that real sea waves give higher power peaks than for the ideal case studied in this report (even for passive loading $k > 2$) [13]. It is therefore important to build a more accurate model of the sea to view the effect it has on the advisable control strategies.

Finally, a complete wave-to-wire model of the system should be made. This means that a complete model of the electrical system, from the generator to the grid connection point, will have to be implemented. The modelling and control of the power electronics converter will be an essential task. The hydrodynamical time domain model and the accordingly selected tuning of the PTO elements would serve as input to the control of the rectifier circuit to ensure that the desired PTO force is obtained.

References

[1] T.W.Thorpe, "An overview of wave energy technologies: Status, performance and costs", in Wave Power: Moving Towards Commercial Viability., London, U.K.: IMechE Seminar, 1999.

[2] A. Babarit, J.Hals, M.Muliawan, A.Kuriawan, T. Moan, and J. Krokstad, "Numerical benchmarking study of a selection of wave energy converters", Wave Energy Workshop, NUIM Maynooth, Ireland, 2011.

[3] I.Bjerke, E.Hjetland, G.Tjensvoll, and J.Sjolte, "Experiences from field testing with the bolt wave energy converter", European Wave and Tidal Conference (EWTEC11), Tech. Rep., 2011.

[4] http://www.fredolsen-renewables.com/

[5] http://www.wavehub.co.uk/

[6] E.Tedeschi and M. Molinas, "Control Strategy of Wave Energy Converters Optimized Under Power Electronics Rating Constraints", ICOE, Bilbao, Spain, 2010.

[7] Johannes Falnes, "Ocean Waves and Oscillating Systems: Linear Interaction Including Wave-Energy Extraction", 1st ed. Cambridge, U.K., Cambridge University Press, 2002.

[8] J.Hals, "Moddeling and phase control of wave-energy converters", Doctoral Thesis, Norwegian University of Science and Technology, 2010.

[9] E.Tedeschi and M.Molinas, "Impact of Control Strategies on the Rating of Electric Power Take Off for Wave Energy Conversion", ISIE2010, Bari, Italy, 2010.

[10] "The wave power climate at the wave hub site", journal: Applied Wave Research Review of Wave Power Climate, November 2006.

[11] J.Sjolte, I.Bjerke, A.Crozier,G.Tjensvoll, and M.Molinas, "All-Electric Wave Energy Power Take Off System with Improved Power Quality at the Grid Connection Point", Tech.Rep., 2011.

[12] www.wavestar.com

[13] E.Tedeschi, M.Carraro, M.Molinas, P.Mattavelli, "Effect of Control Strategies on Power Take-Off Efficiency on the Power Capture from Sea Waves", Tech.Rep., 2011.